

AUTONOMOUS NAVIGATION OF AN ELECTRIC ALL-TERRAIN VEHICLE  
ALONG WAYPOINT-DEFINED TRAILS

by

Jacob Thomas Daniel

A thesis submitted to the faculty of  
The University of North Carolina at Charlotte  
in partial fulfillment of the requirements  
for the degree of Master of Science in  
Applied Energy and Electromechanical Engineering

Charlotte

2022

Approved by:

---

Dr. Aidan Browne

---

Dr. Michael Smith

---

Dr. Wesley Williams



## ABSTRACT

JACOB THOMAS DANIEL. Autonomous Navigation of an Electric All-Terrain Vehicle Along Waypoint-Defined Trails. (Under the direction of DR. AIDAN F. BROWNE)

Previous research attempted to autonomously control an internal combustion all-terrain vehicle platform but was unsuccessful due to the inability to reliably control speed. To address this, an electric motor conversion is performed on the platform to enhance its stability and controllability. A robust trail detection methodology is applied to this electric all-terrain vehicle (eATV) prototype to autonomously traverse a 3- to 5-meter-wide wooded trail, an environment that introduces unique challenges for autonomous vehicle control. The vehicle can follow a predetermined route defined by periodic waypoints placed by a human along a trail. A suite of real-time image processing algorithms is developed to respond to input from an Intel RealSense depth camera mounted on the platform. Various simultaneous solutions for path following are prioritized using a confidence scoring approach. Image processing and control techniques are also introduced for obstacle detection and avoidance schemes. The prototype vehicle has successfully navigated waypoint routes along walking trails for over 500-meters while detecting obstacles and pedestrians in real-time. To accommodate global positioning system denial that occurs occasionally in wooded environments, algorithms based on image processing are implemented for navigation toward the subsequent waypoint. An adaptive throttle-braking algorithm is also introduced to maintain a targeted velocity throughout the traversed environment. This research investigates and fulfills a budget-conscious methodology for autonomous off-road vehicle navigation along trails.

## ACKNOWLEDGMENTS

I would like to acknowledge the extensive contribution and engagement of Dr. Aidan Browne in the completion of this research. His mentorship and drive for student development were invaluable to this thesis and the various other research we have pursued. Dr. Browne's volunteered time and effort has influenced my engineering mindset in directions I would not have considered prior to my graduate career.

I would also like to thank Dr. Michael Smith and Dr. Wesley Williams for their added expertise and willingness to aid in this endeavor. Their guidance was advantageous in several aspects of the research, providing practical avenues to expand my specific knowledge and develop a passion for autonomous research.

## DEDICATION

This thesis is dedicated to three great men responsible for igniting my curiosity and passion for engineering. It is safe to say I would not be where I am today without their willingness to teach their trades, to narrate technical and undoubtedly humorous stories, and to lead by example. In honor of F.D. “Earnest” Collier, and in loving memory of Luther “Grifton” Daniel and Thomas “Jerry” Ellis. Thank you for the unwavering support and memorable life lessons throughout the years.

I also dedicate this thesis to my parents, Joseph and Lorie, and my sister, Leah. Your guidance and influence for me to always try my best has pushed me to heights unimaginable to me just a couple of years earlier. I am especially grateful for the encouragement, love, and compassion you have instilled into the man I am today.

## TABLE OF CONTENTS

LIST OF TABLES .....	x
LIST OF FIGURES .....	xi
LIST OF ABBREVIATIONS.....	xvii
CHAPTER 1: INTRODUCTION.....	1
1.1 Background.....	1
1.2 Problem Statement.....	1
1.3 Objectives .....	2
CHAPTER 2: LITERATURE REVIEW .....	3
2.1 Powertrain.....	3
2.1.1 Internal Combustion Engine .....	3
2.1.2 Electric Drive.....	4
2.2 Path Detection.....	5
2.2.1 Color Vision Processing .....	5
2.2.2 LiDAR.....	8
2.2.3 Depth.....	10
2.3 Localization.....	11
2.3.1 Global Positioning System.....	11
2.3.2 Global Navigation Satellite System.....	11
2.3.3 Simultaneous Localization and Mapping.....	12

2.4 Navigation.....	12
2.4.1 Waypoint Navigation.....	12
2.4.2 Vehicle Navigation .....	13
2.5 Off-Road Autonomy.....	15
2.5.1 Autonomous Vehicle Control .....	15
2.5.2 Environmental Factors .....	17
CHAPTER 3: DESIGN OVERVIEW .....	18
3.1 Base Vehicle .....	18
3.2 Vehicle Contributions .....	20
3.3 EV Conversion.....	23
3.3.1 EV Conversion Kit.....	23
3.3.2 Conversion Design.....	25
3.3.3 EV Power Modeling .....	28
3.4 System Architecture.....	33
3.4.1 Computing.....	33
3.4.2 Sensing.....	38
3.4.3 Actuation.....	39
3.5 Cost of Conversion .....	43
CHAPTER 4: METHODOLOGY .....	45
4.1 Vision Processor .....	45

4.1.1 Color Vision.....	46
4.1.2 Depth Vision .....	46
4.1.3 Obstacle Detection.....	47
4.2 Mobility System.....	49
4.2.1 Depth Vision Mobility .....	49
4.2.2 Color Vision Mobility.....	51
4.2.3 Operational Mobility.....	52
4.3 GPS Localization .....	53
4.4 Testing.....	53
4.4.1 Comparative Testing.....	54
4.4.2 Color Vision Testing.....	55
4.4.3 Depth Vision Testing .....	56
4.4.4 Operational Testing.....	56
CHAPTER 5: RESULTS AND DISCUSSION.....	57
5.1 Comparative Testing.....	57
5.1.1 ICE Warm Start.....	57
5.1.2 ICE Cold Start.....	72
5.1.3 Electrified.....	85
5.1.4 Overview .....	100
5.2 Computer Vision Testing.....	102

5.2.1 Tunnel Vision.....	102
5.2.2 Intersections .....	105
5.2.3 Path Detection.....	107
5.2.4 Obstacle Detection.....	108
5.3 GPS Testing .....	110
5.4 Autonomy Testing .....	113
5.4.1 Speed Control.....	113
5.4.2 Vehicle Steering.....	114
5.4.3 Image Prioritization .....	115
5.4.4 Obstacle Maneuvering.....	116
5.5 Integration Testing.....	116
CHAPTER 6: CONCLUSIONS .....	119
6.1 Overview.....	119
6.2 Future Work .....	120
REFERENCES .....	122
APPENDIX A: LabVIEW Code.....	125
APPENDIX B: Computer Vision Scripts .....	130
APPENDIX C: Supplemental Information.....	132

## LIST OF TABLES

TABLE 1: Categorized Cost of Prototype and eATV .....	44
TABLE 2: HTT Conditions at 82°F Ambient .....	73
TABLE 3: MTT Conditions at 82°F Ambient.....	75
TABLE 4: LTT Conditions at 82°F Ambient.....	77
TABLE 5: Uphill HTT Conditions at 83°F Ambient .....	79
TABLE 6: Uphill MTT Conditions at 83°F Ambient .....	81
TABLE 7: Uphill MTT Conditions at 83°F Ambient .....	83

## LIST OF FIGURES

FIGURE 1: Vex Robotics Example DC Motor Curve.....	5
FIGURE 2: Example Histogram Back Projection Tracks: Detected Track Start points (1), Left and Right Tracks (2), Connected Mask (3), Final Results (4) .....	6
FIGURE 3: Example Template Matching: Input (1), Template (2), Template Matching Matrix (3), Result (4) .....	7
FIGURE 4: Example Roadside Detector: Scanline Scheme (1), Single Scanline (2), Detected Roadside (3), Final Result (4).....	8
FIGURE 5: Example 2D LiDAR Use Case for Lower-Level Obstacle Detection.....	9
FIGURE 6: Example Demonstration of Stereo Vision Methodology .....	10
FIGURE 7: Predetermined Waypoint Route Along UNC Charlotte Fitness Trail.....	13
FIGURE 8: Autonomous Waypoint Navigation in GPS-Denied Scenario .....	14
FIGURE 9: Multi-Layer Hierarchical Control for Reliable Autonomous Control.....	16
FIGURE 10: Machine Learning Steering Model for ATV .....	17
FIGURE 11: Initial State of Base Vehicle: ATLAS for 2017 AFRL Design Challenge .	19
FIGURE 12: Before (top) and After (bottom) Steering Gearbox Refresh.....	20
FIGURE 13: Implemented Design of Free-Structure Encoder.....	22
FIGURE 14: Retrofit Connection for Torque Motor and Linear Actuator Mechanism...	23
FIGURE 15: Vevor 48 V 2000 W Electric Conversion Kit .....	24
FIGURE 16: EV Conversion Drivetrain Assembly.....	26
FIGURE 17: Post-Install Modification to EV Drivetrain Assembly .....	27
FIGURE 18: Rear Dimetric (left) and Front Isometric (right) Views of the Revised Assembly.....	28

FIGURE 19: MATLAB Motor & Drive Block Parameters.....	29
FIGURE 20: MATLAB Longitudinal Vehicle Block Parameters.....	30
FIGURE 21: MATLAB Simscape Simulation of eATV .....	31
FIGURE 22: Proportional and Integral Control for Vehicle Speed Simulation .....	31
FIGURE 23: MATLAB Simulation: Current Draw at 2.5 m/s Target Velocity .....	32
FIGURE 24: MATLAB Simulation: Current Draw at 6 m/s Target Velocity .....	33
FIGURE 25: NI myRIO Port Display and Configuration .....	34
FIGURE 26: Implemented myRIO Expansion Port A .....	35
FIGURE 27: Implemented myRIO Expansion Port B.....	36
FIGURE 28: Hardware Configuration for Remote Vehicle Control.....	37
FIGURE 29: Hardware Configuration for Autonomous Vehicle Control.....	38
FIGURE 30: Vevor Motor Controller Wiring Diagram .....	42
FIGURE 31: Binary Path Detection: Upper Left (UL): Color Image, Upper Right (UR): Saturation Plane. Lower Left (LL): Binary Threshold, Lower Right (LR): Advanced Morphology.....	46
FIGURE 32: UL: Depth Image, UR: Color Extraction, LL: Binary Analysis, LR: Circle Detection.....	47
FIGURE 33: UL: Depth Image, UR: Masked Color Extraction, LL: Binary Analysis, LR: Circle Detection .....	48
FIGURE 34: UL: Depth Image, UR: Color Extraction, LL: Binary Analysis, LR: Shape Matching.....	49
FIGURE 35: Weight Assignment of Targeted Path Depth Imaging .....	50
FIGURE 36: Colorized Lookup Table.....	51

FIGURE 37: Centroid-based Trajectory for Path Detection Methods.....	52
FIGURE 38: Predetermined Waypoint Route .....	53
FIGURE 39: Orientation for Flat Ground Velocity Tests .....	55
FIGURE 40: Flat Ground HTT: Warm Start .....	58
FIGURE 41: Averaged HTT & Variation: Warm Start.....	59
FIGURE 42: Flat ground MTT: Warm Start .....	60
FIGURE 43: Averaged MTT & Variation: Warm Start .....	61
FIGURE 44: Flat Ground LTT: Warm Start.....	62
FIGURE 45: Averaged LTT & Variation: Warm Start .....	63
FIGURE 46: Summarized Throttle Response: Warm Start.....	64
FIGURE 47: Uphill HTT: Warm Start .....	65
FIGURE 48: Averaged Uphill HTT & Variation: Warm Start.....	66
FIGURE 49: Uphill MTT: Warm Start.....	67
FIGURE 50: Averaged Uphill MTT & Variation: Warm Start.....	68
FIGURE 51: Uphill LTT: Warm Start.....	69
FIGURE 52: Averaged Uphill LTT & Variation: Warm Start.....	70
FIGURE 53: No Throttle Downhill Test: Warm Start.....	71
FIGURE 54: No Throttle Downhill Variation: Warm Start .....	72
FIGURE 55: Flat Ground HTT: Cold Start .....	73
FIGURE 56: Averaged HTT & Variation: Cold Start .....	74
FIGURE 57: Flat Ground MTT: Cold Start.....	75
FIGURE 58: Averaged MTT & Variation: Cold Start .....	76
FIGURE 59: Flat Ground LTT: Cold Start.....	77

FIGURE 60: Averaged LTT & Variation: Cold Start .....	78
FIGURE 61: Summarized Throttle Response: Cold Start .....	79
FIGURE 62: Uphill HTT: Cold Start.....	80
FIGURE 63: Averaged Uphill HTT & Variation: Cold Start.....	81
FIGURE 64: Uphill MTT: Cold Start.....	82
FIGURE 65: Averaged Uphill MTT & Variation: Cold Start .....	83
FIGURE 66: Uphill LTT: Cold Start .....	84
FIGURE 67: Averaged Uphill LTT & Variation.....	85
FIGURE 68: Flat Ground HTT: EV .....	86
FIGURE 69: Averaged HTT & Variation: EV .....	87
FIGURE 70: Flat Ground MTT: EV.....	88
FIGURE 71: Averaged MTT & Variation: EV .....	89
FIGURE 72: Flat Ground LTT: EV .....	90
FIGURE 73: Averaged LTT & Variation: EV .....	91
FIGURE 74: Summarized Throttle Response: EV .....	92
FIGURE 75: Uphill HTT: EV.....	93
FIGURE 76: Averaged Uphill HTT & Variation: EV .....	94
FIGURE 77: Uphill MTT: EV .....	95
FIGURE 78: Averaged Uphill MTT & Variation: EV .....	96
FIGURE 79: Uphill LTT: EV .....	97
FIGURE 80: Averaged Uphill LTT & Variation: EV .....	98
FIGURE 81: Summarized Uphill Throttle Response: EV .....	99
FIGURE 82: No Throttle Downhill Test: EV.....	100

FIGURE 83: ICE Warm Start, ICE Cold Start, and EV Acceleration Curves .....	101
FIGURE 84: UNC Charlotte Fitness Trail: Summer (left) and Autumn (right).....	103
FIGURE 85: UL: Depth Image, UR: Binary Extraction, LL: Advanced Morphology, LR: Circle Detection .....	104
FIGURE 86: UL: Base Image, UR: Depth, LL: Orig. Method, LR: Rev. Method .....	105
FIGURE 87: Intersection Detection Approach.....	106
FIGURE 88: Intersection: Color Image (left) and Depth Image (right) .....	107
FIGURE 89: UL: Color Image, UR: Binary Extraction, LL: Binary Erosion, LR: Advanced Morphology .....	108
FIGURE 90: Onboard GPS Module Validation .....	111
FIGURE 91: Adaptive Throttle and Braking Performance from 500+ meter Test .....	114
FIGURE 92: Steering Performance from Autonomous 50+ meter Test .....	115
FIGURE 93: Initial Remote Control eATV Test on UNC Charlotte Fitness Trail .....	117
FIGURE 94: Vision Processing Image Script Prioritization .....	125
FIGURE 95: Applying Weighing to Geometry of Interest.....	126
FIGURE 96: Waypoint Detection at Intersections .....	127
FIGURE 97: Steering Algorithm for Color-Vision Imaging.....	127
FIGURE 98: Steering Algorithm for Depth-Vision Imaging .....	127
FIGURE 99: Steering Algorithm for Obstacle Avoidance .....	128
FIGURE 100: Adaptive Throttle-Braking Algorithm.....	129
FIGURE 101: Gravel Detection Script.....	130
FIGURE 102: Asphalt Detection Script .....	130
FIGURE 103: Obstacle Detection Script.....	130

FIGURE 104: Depth Analysis Script.....	130
FIGURE 105: Pedestrian Detection Script .....	131
FIGURE 106: Offset DC Motor Steering Assembly .....	132
FIGURE 107: Installed EV Conversion Kit and Supporting Components.....	133
FIGURE 108: Encoder Structure .....	134
FIGURE 109: Installed Encoder Structure .....	135

## LIST OF ABBREVIATIONS

2D	Two Dimensional
3D	Three Dimensional
A	Amps
Ah	Amp-hour
API	Application Programming Interface
ATV	All-Terrain Vehicle
cc	cubic centimeters
CAD	Computer-Aided Design
CAN	Controller Area Network
DC	Direct Current
DC-AC	Direct Current to Alternating Current
DIO	Digital Input/Output
eATV	electric All-Terrain Vehicle
EKF	Extended Kalman Filter
EUD	End User Device
FOV	Field of View
GNSS	Global Navigation Satellite System
GPS	Global Positioning System
IMAQ	Image Acquisition
IMU	Inertial Measurement Unit
ID	Inner Diameter
in	Inches

KF	Kalman Filter
kg	Kilogram
LADAR	LAser Detection And Ranging
LiDAR	Light Detection And Ranging
m	Meter
ML	Machine Learning
MPH	Miles Per Hour
MSP	Mini System Port
MXP	myRIO Expansion Port
NI	National Instruments
NC	Normally Closed
OD	Outer Diameter
PWM	Pulse Width Modulation
RGB	Red/Green/Blue
RGB-D	Red/Green/Blue Depth
ROI	Region of Interest
RPM	Revolutions Per Minute
SDK	Software Development Kit
SLAM	Simultaneous Localization and Mapping
UGV	Unmanned Ground Vehicle
V	Volts
VI	Virtual Instrument
W	Watt

## CHAPTER 1: INTRODUCTION

### 1.1 Background

For this research, off-road autonomy can be defined as a vehicle autonomously traversing any demarcated trail topography. These environments include walking, ATV, and nature trails with asphalt, gravel, and dirt terrains. Most current autonomous ground vehicles navigate well-defined and marked roadways. An accessible unmanned vehicle capable of traversing a variety of complex terrains as compared to commercially available flat-ground autonomous vehicles would provide a substantial boost for research in many topic areas. Several use cases for a vehicle with such capabilities would benefit industries such as construction, military, search and rescue, fire risk evaluation, exploration, supply transportation, and farming. Limitations arise when evaluating the cost of one commercially available vehicle that likely requires modification to achieve off-road autonomy. Navigation is another concern for off-road vehicles as the environments are often taxing on GPS connectivity due to potentially remote locations and dense tree foliage.

### 1.2 Problem Statement

It is necessary to advance budget-conscious methodologies for off-road autonomous ground vehicle navigation. Small ATVs are a well-developed solution for off-road trail environments but are not easily speed-controlled in autonomous applications. A methodology is needed to control an existing ATV platform for autonomously navigating trail environment topographies with intermittent GPS access.

### 1.3 Objectives

This research aims to develop a methodology for an existing ATV to navigate along a waypoint-defined route autonomously. The tasks required the conversion of a petrol-based ATV to an EV platform for simplified, reliable control. Computer vision was implemented with an RGB-D camera for enhanced image processing to improve path detection. The vehicle should receive a waypoint-guided route of coordinates to define the desired path accounting for areas of GPS denial. Lastly, the vehicle must implement detection of and maneuvering schemes around debris, obstacles, and pedestrians.

## CHAPTER 2: LITERATURE REVIEW

A literature review was conducted to survey existing autonomous control of vehicle powertrains, trail detection, localization, and navigation.

### 2.1 Powertrain

Ground vehicle powertrains are typically limited to petrol-based ICEs and electric motors. The powertrain delivers a rotational force to at least one drive axle comprising two or more wheels or a tracked assembly. Distinguishing the attributes of the ICE and electric powertrains allowed a justified selection for the prototype vehicle. It is important to note that ICEs are inherently difficult to control in autonomous control schemes.

#### 2.1.1 Internal Combustion Engine

In efforts to develop a multi-terrain capable, budget-conscious autonomous vehicle, limited commercially available starting platforms can traverse the challenging terrain and a distance over 500 m. This often drives researchers to use ICE-powered vehicles, specifically designed for off-road conditions, such as ATVs. ATVs are capable machines designed for riders to navigate trails and varying terrains, though they can be troublesome when integrating with an autonomous system. Prior research has been conducted to develop methodologies for CAN bus throttle control of an ATV platform [1]. The CAN-bus-controlled throttle body was actuated via a servo motor attached to a drive flange in place of the original cable-driven accelerator with better success. The variability of ICEs, however, as the engines become heat soaked or in variable loading scenarios, is not conducive for high-fidelity autonomous control. Additionally, minimizing costs to an air-cooled and carbureted platform exploits these limitations

further, as it is known that heat directly changes the characteristics of which a carburetor flows a mixture of air and fuel to the ICE [2]. Expecting any form of linear throttle control for a budget-conscious autonomous ICE-powered vehicle is improbable without the aid of a deep-learning engine.

### 2.1.2 Electric Drive

Electric powertrains are predominantly outfitted in commercially available autonomous vehicles commonly found in transportation, manufacturing, and cleaning service applications. Aside from the increased charge time compared to an ICE fuel fill-up, there are few drawbacks to using electric motor drivetrains in autonomous vehicles. The linear speed control, motor and battery efficiency, and low-speed torque all aid in implementing a more predictable control scheme [3]. Typical DC motor curves express an optimal operation speed where output torque, power, and efficiency are nearest the maximum. A Vex Robotics DC motor example, as shown in Figure 1, models the expected behavior of a DC motor. To achieve the optimal operating range of any DC motor, a specific gear reduction is often applied to maintain high efficiency for the specific operational requirements [4].

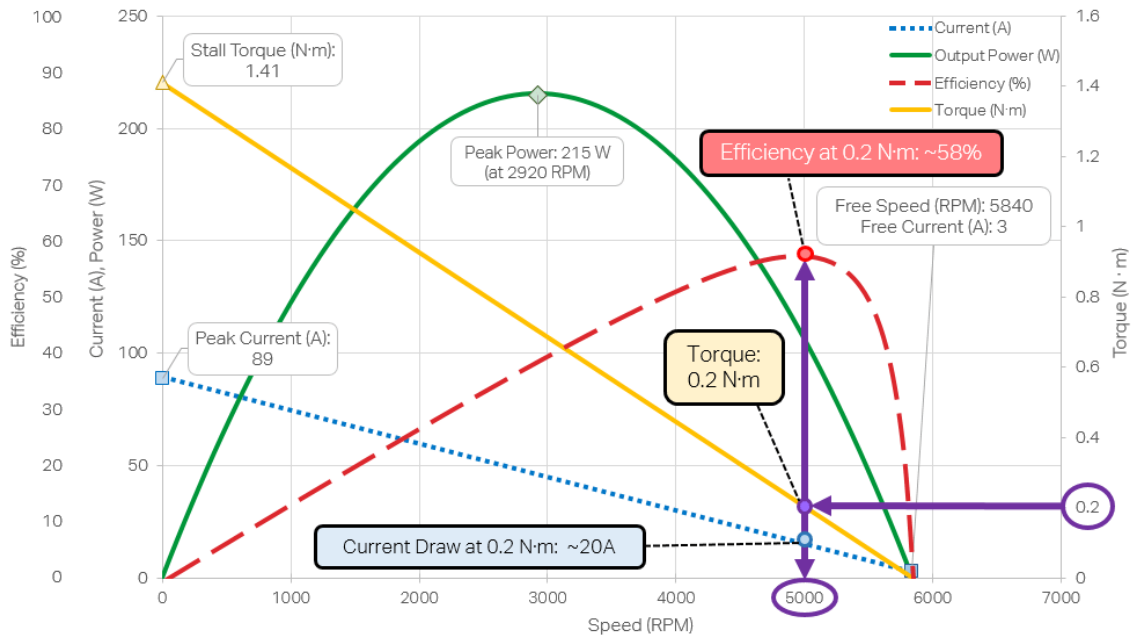


Figure 1: Vex Robotics Example DC Motor Curve

## 2.2 Path Detection

To successfully navigate through walking trail topographies, a means of computer vision is required for autonomous vehicles. Methodologies to detect pre-existing trails vary from contrasting appearance of the color imaging to pattern matching and 2D and 3D LiDAR. Color vision processing uses a captured image of an environment as visible to the human eye. LiDAR methods generate an array of distance values from a measurement device at varying angles. After comparing two disparity images, depth processing assigns a distance value to each pixel in an intensity graph.

### 2.2.1 Color Vision Processing

One method of interpreting a color image to define a trail includes increasing the image saturation and targeting a specific color range given the path material. The 2018 research tested asphalt, saturated dirt, dirt, and tracked paths in the [5]. This research

steps through the implementation of color saturation segmentation, template matching, and scanline feature detection.

Figure 2 features a tracked path with two different color tones indicating the path direction. Oversaturating the image and searching a histogram of color ranges can produce a binary image indicating the trail and can be further processed to determine the desired direction-of-travel result.

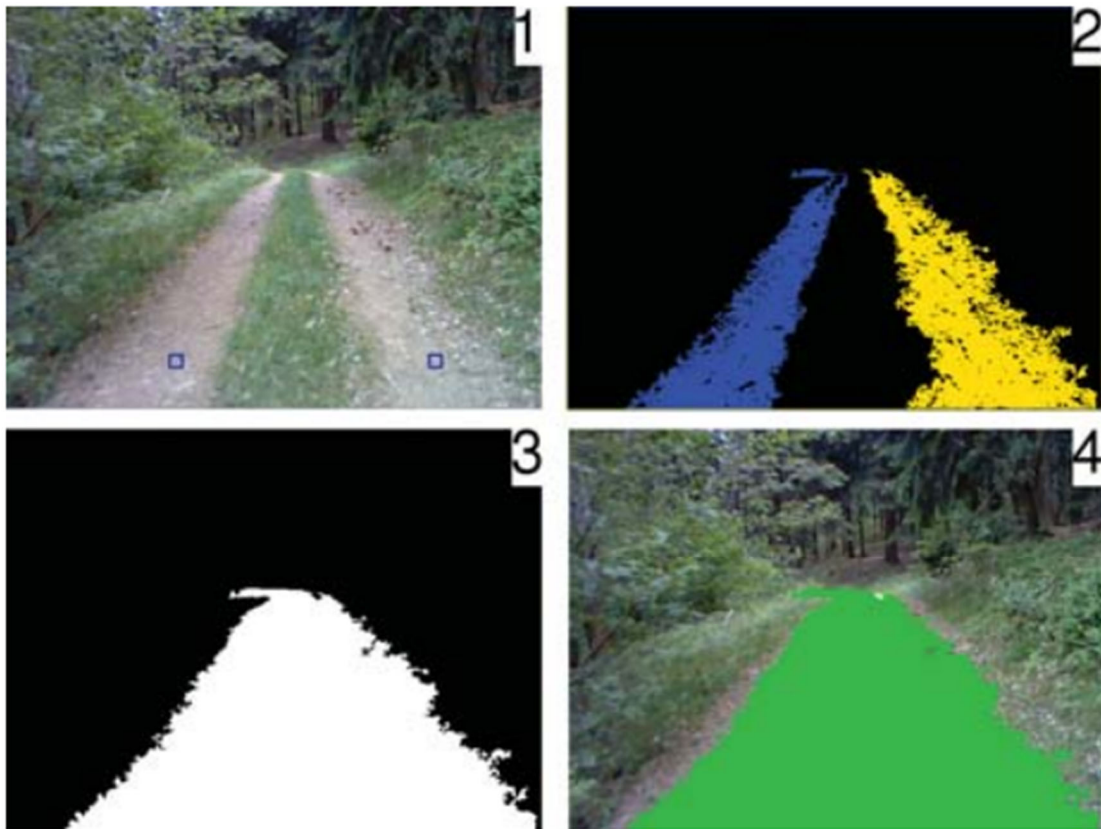


Figure 2: Example Histogram Back Projection Tracks: Detected Track Start points (1), Left and Right Tracks (2), Connected Mask (3), Final Results (4)

Figure 3 illustrates the use of pattern matching in the case of matching a frame including a patch of gravel with other portions of the image. A confidence score of the

pattern can be processed across the image and indicated at the likely path location. As a result, a general path direction and shape can be procured.

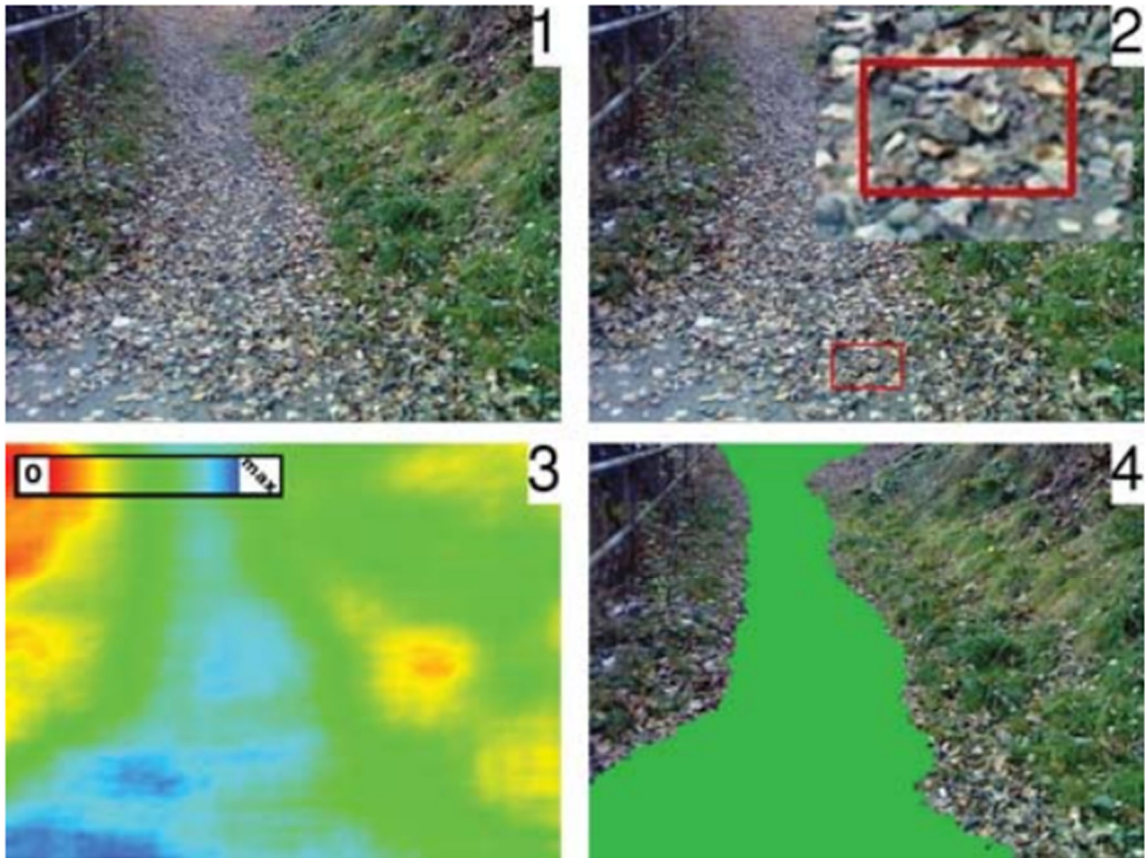


Figure 3: Example Template Matching: Input (1), Template (2), Template Matching Matrix (3), Result (4)

Figure 4 demonstrates a scanline function searching for determined features around a specified point in the image. In this case, the scanline detects a roadside and places a point at the vector end. Scanning around the point 180 degrees forward can be used to find multiple roadside detections and plotted to develop a general path shape.

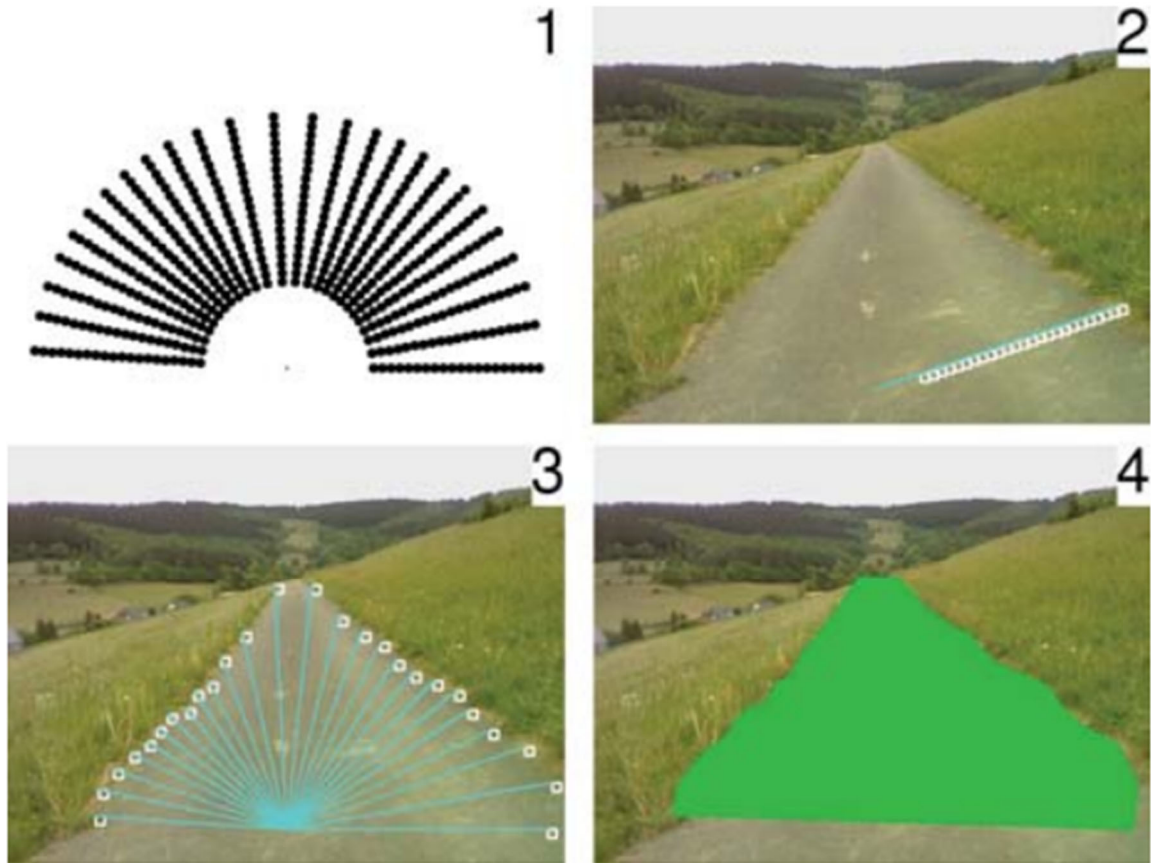


Figure 4: Example Roadside Detector: Scanline Scheme (1), Single Scanline (2), Detected Roadside (3), Final Result (4)

Other methods for rapid trail detection have been developed using the contrasting appearance approach and minimizing the computational demand by indicating two perspective lines along the trail direction. This method can be used where a definable edge detection is available.

### 2.2.2 LiDAR

2D LiDAR has been used in autonomous vehicles for obstacle detection and path detection where applicable. LiDAR is frequently used in mapping applications where

obstacles are vertically invariable (e.g., straight walls, cabinets, chairs.) [6]. When placed to view in the horizontal direction, a 2D LiDAR module can only detect distance at the same horizontal level as the sensor. For example, a robot tasked to drive through a hallway without touching any objects by only using LiDAR would fail if a limbo bar is stretched across the hallway either above or below the detection plane of the sensor. [7] implemented a methodology to improve 2D LiDAR in obstacle detection applications by lowering the angle of the device toward the ground. This increases the likelihood of detecting objects resting on the ground without regard for the object height; however, the detection range becomes limited as the device can only register the tangent distance, which can be visualized in Figure 5.

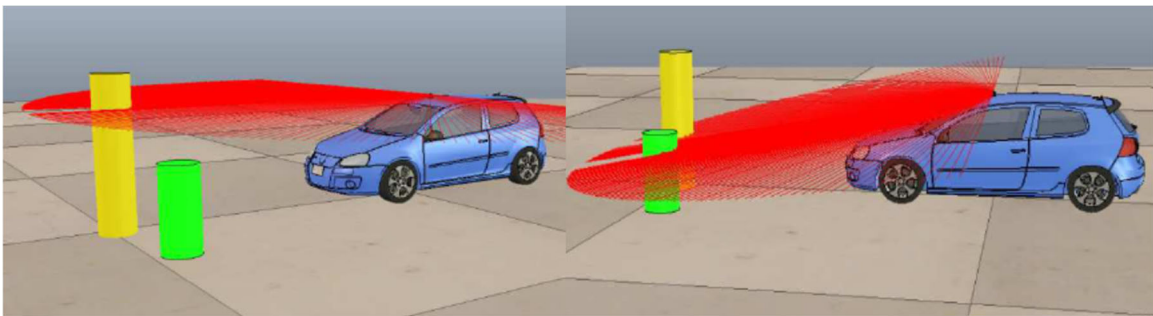


Figure 5: Example 2D LiDAR Use Case for Lower-Level Obstacle Detection

Schemes have been developed using a 2D LiDAR on an actuated third axis to develop a low-cost 3D LiDAR, essentially, but this method would only further limit the detection capabilities in the rugged trail environment [8]. In contrast, 3D LiDAR maps a visible frame of the surrounding area on all axes. The research [9] implemented 3D LiDAR for curb detection on an autonomous road vehicle. This method captured the curb dimensions and path proximities for avoidance and intersection mapping. The 3D LiDAR data was filtered into different layers of probable surfaces, including the road, curb,

sidewalk, and off-road areas. This environmental perception capability would be advantageous in off-road trail applications, though it would be considered out of the budget-conscious scope for this research.

### 2.2.3 Depth

Depth imaging provides another method for multidimensional vision by capturing two still images of differing perspectives and calculating the depth of a particle. This binocular disparity calculation is the same method performed by the human eye, as expressed in Figure 6 [10].

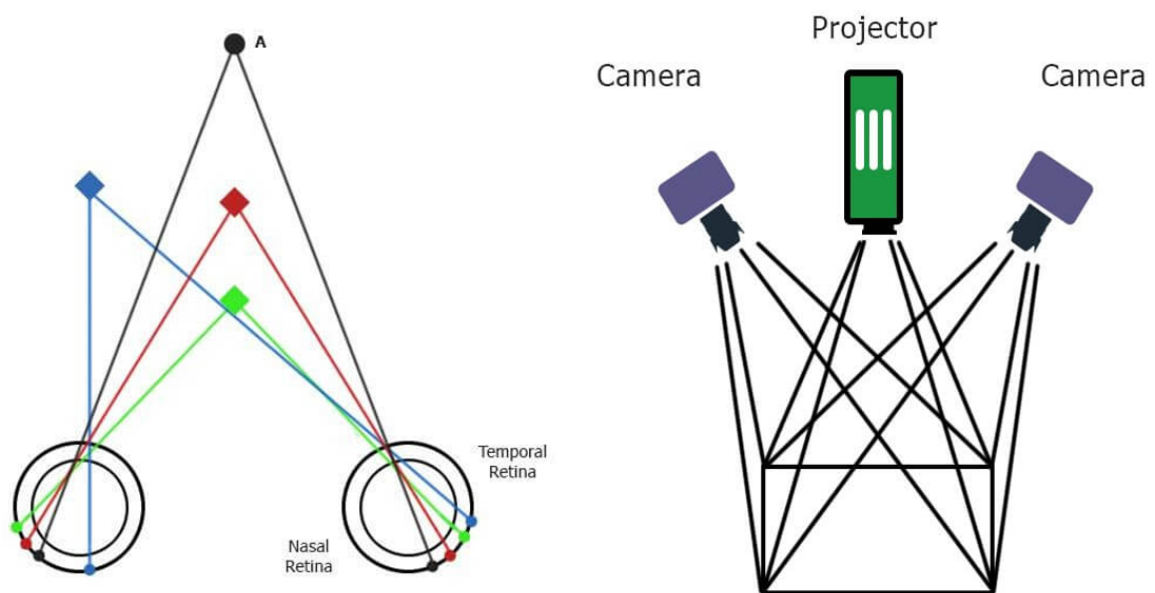


Figure 6: Example Demonstration of Stereo Vision Methodology

Figure 6 details a depth camera emitting laser points to increase the effectiveness of the binocular camera configuration. This depth imaging method could be implemented in place of a 3D LiDAR to perform distance calculations analogous to standard RGB color imaging [11].

## 2.3 Localization

For a vehicle to operate autonomously, it must locate itself locally or globally. GPS, GNSS, and SLAM are methods to acquire location and orientation information based on the vehicle's position relative to a known position of one or more defined objects. GPS calculates position based on the U.S. satellite-based radionavigation system. Using GNSS provides access to the international multi-constellation satellite system. SLAM implements a map-building algorithm to orient and track the position of a vehicle with respect to the surrounding environment.

### 2.3.1 Global Positioning System

GPS acquisition allows a user or robotic device to geolocate based on available orbital satellites. These devices are common, relatively inexpensive, and compatible with most programming languages and computing hardware. Because it uses triangulation methods, a GPS unit must connect with three or more satellites, each with its range of error due to the earth's curvature, to find where the three ranges collide. Ideally, a connection with four or more satellites would provide the most accurate GPS coordinate estimation [12]. A heading value can be determined from the compass internal to each GPS unit or by capturing the difference between GPS coordinates with respect to time. A GPS unit can more precisely measure its velocity than its actual position [13].

### 2.3.2 Global Navigation Satellite System

Similar to GPS, GNSS uses orbital satellites to acquire global coordinates. However, GNSS accesses greater numbers of satellites in orbit, thus increasing the accuracy, speed of acquisition, and satellite availability. GNSS modules are integrated

with KF and EKF to take advantage of the optimized estimation algorithms [14]. The estimation algorithms often coincide with SLAM operations for autonomous vehicle operations.

### 2.3.3 Simultaneous Localization and Mapping

SLAM is a locally based positioning system optimized for known areas of interest [15]. SLAM methods are used in autonomous vehicle applications such as the iRobot Roomba to acquire the features of an environment, build a model of the environment, and learn an optimal route to complete its tasks given the environment [16]. SLAM has been implemented on various other autonomous vehicles, often configured with LiDAR to aid in obstacle avoidance and environment mapping [17,18].

## 2.4 Navigation

To navigate through a defined environment, an autonomous vehicle must have a method for interpreting the environment and reacting accordingly. For instance, if the vehicle is in motion, it must steer to follow a path, increase throttle to climb a hill, and brake to avoid a collision. Methods for path following include waypoint navigation, where a human marks coordinates along a path with the intention for an unmanned vehicle to follow later. Adaptive throttle and obstacle avoidance are methods of vehicle navigation necessary for responding to the surroundings within an environment.

### 2.4.1 Waypoint Navigation

To the avid vehicle user, point-to-point driving directions are a seemingly necessary tool for traveling outside of the daily commute. Likewise, for an autonomous

vehicle, a sense of direction is necessary to traverse between two known points.

Waypoint navigation has been implemented in many robotic systems, including UAVs, UGVs, and USVs. Prior research [18,19] has expanded the applicability of breadcrumb navigation, a user-defined trail of points to later be returned by an autonomous vehicle.

This methodology is advantageous for applications where a region may be scouted before introducing an autonomous vehicle for search and rescue, surveillance, or fire risk evaluation. An example of a predetermined waypoint route is included in Figure 7.

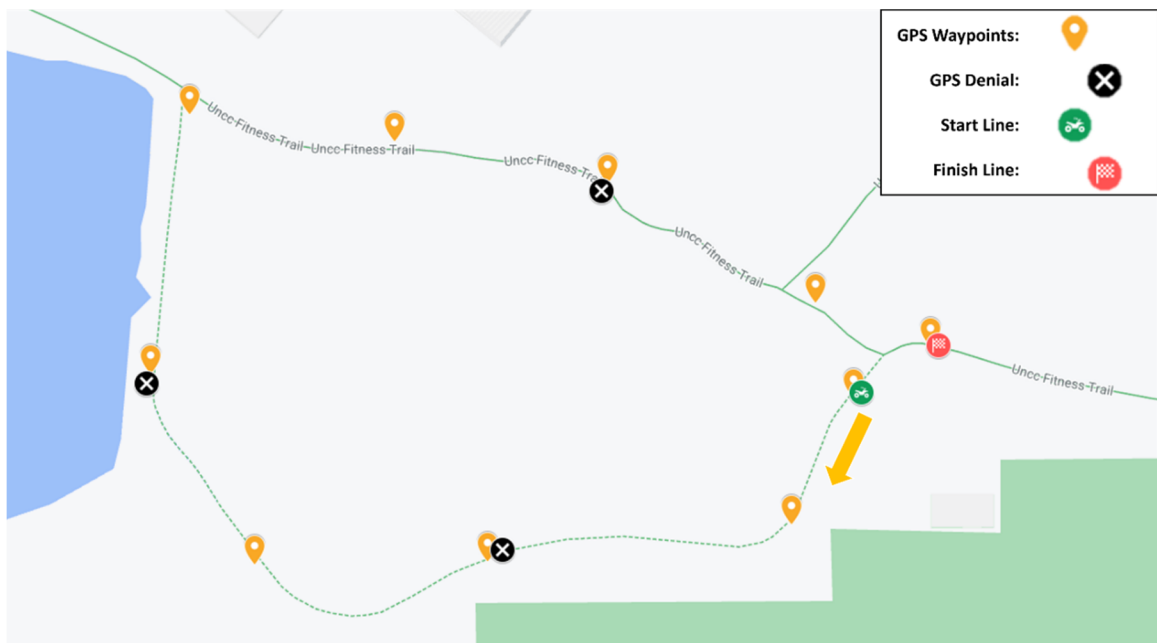


Figure 7: Predetermined Waypoint Route Along UNC Charlotte Fitness Trail

#### 2.4.2 Vehicle Navigation

An autonomous vehicle can maneuver point to point in a flat terrain environment via commanded waypoint navigation [19]. Calculating the vehicle heading and translating the GPS coordinates from global to local orientation introduced a direction for the vehicle to base a steering operation, as shown in Figure 8. Quite frequently, in off-road trail environments, GPS connectivity may be lost or denied due to the location or

foliage coverage. Operating in such conditions requires disregarding a denied waypoint and continuing through the terrain to the next available waypoint [20].

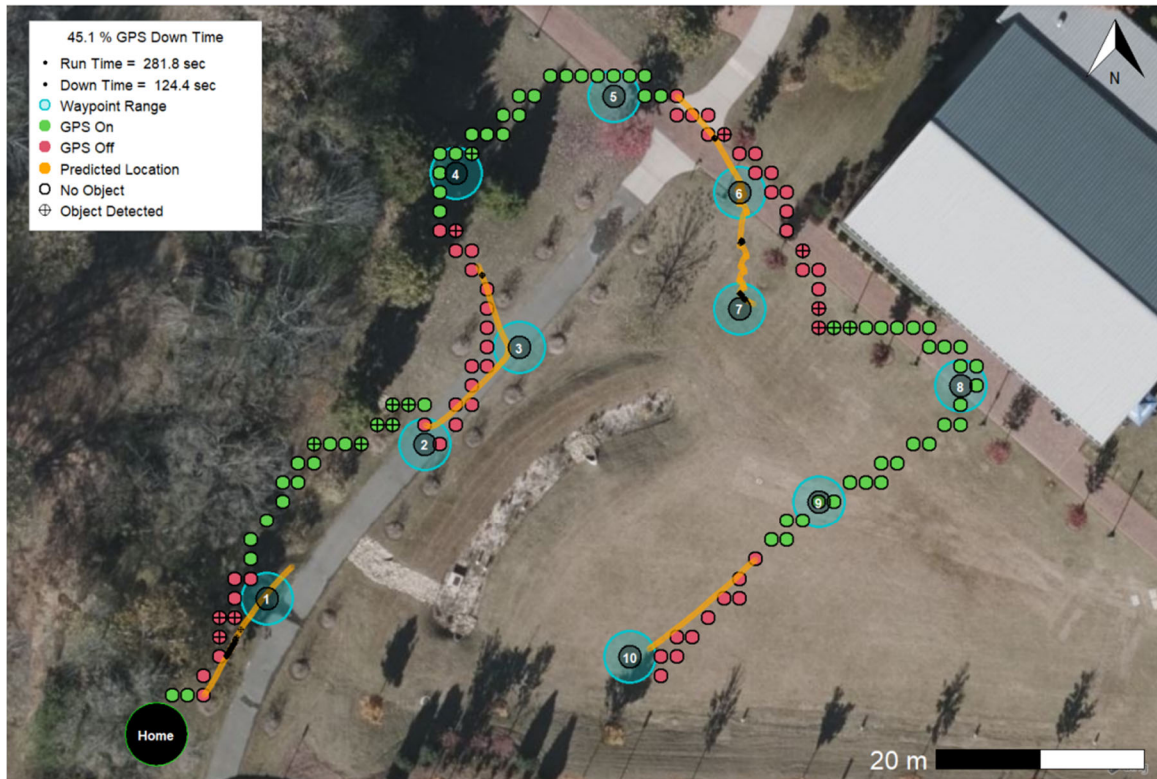


Figure 8: Autonomous Waypoint Navigation in GPS-Denied Scenario

Various steering schemes have been introduced in autonomous vehicles based on vision data. For example, pollution acquisition research [21] developed a swim-lane approach to traverse aquatic environments in a guided direction based on a vision model. As the USV operated its course, pollution was recognized and targeted for extraction. The methodology provided the USV to change course toward the targeted pollution and return to its course accordingly following the completion of the procedure.

## 2.5 Off-Road Autonomy

With the ever-advancing technologies enabling higher-fidelity autonomy, it is clear that autonomous vehicle research will continue to expand into non-traditional road types. Non-traditional road types can be defined as unmarked walking trails, game trails, dry riverbeds, and other similar environments. Precise vehicle control is necessary to traverse such environments. Factors such as terrain grade, wheel traction, and tire deflection may also be accommodated in off-road autonomy control schemes.

### 2.5.1 Autonomous Vehicle Control

System integration is crucial for reliable off-road autonomy. Programming architecture was evaluated in part by [22] with the implementation of a multi-layer hierarchical control to reduce the need for human supervision seen in Figure 9. This research details the difficulties in traversing point to point without an intermediate step or provided variables such as GPS waypoints. Reactive planning and control were implemented in the autonomous scheme in response to a LADAR vision system. The team also found discrepancies with computer vision during the introduction of wooden environments and tuning methods based on human perspective.

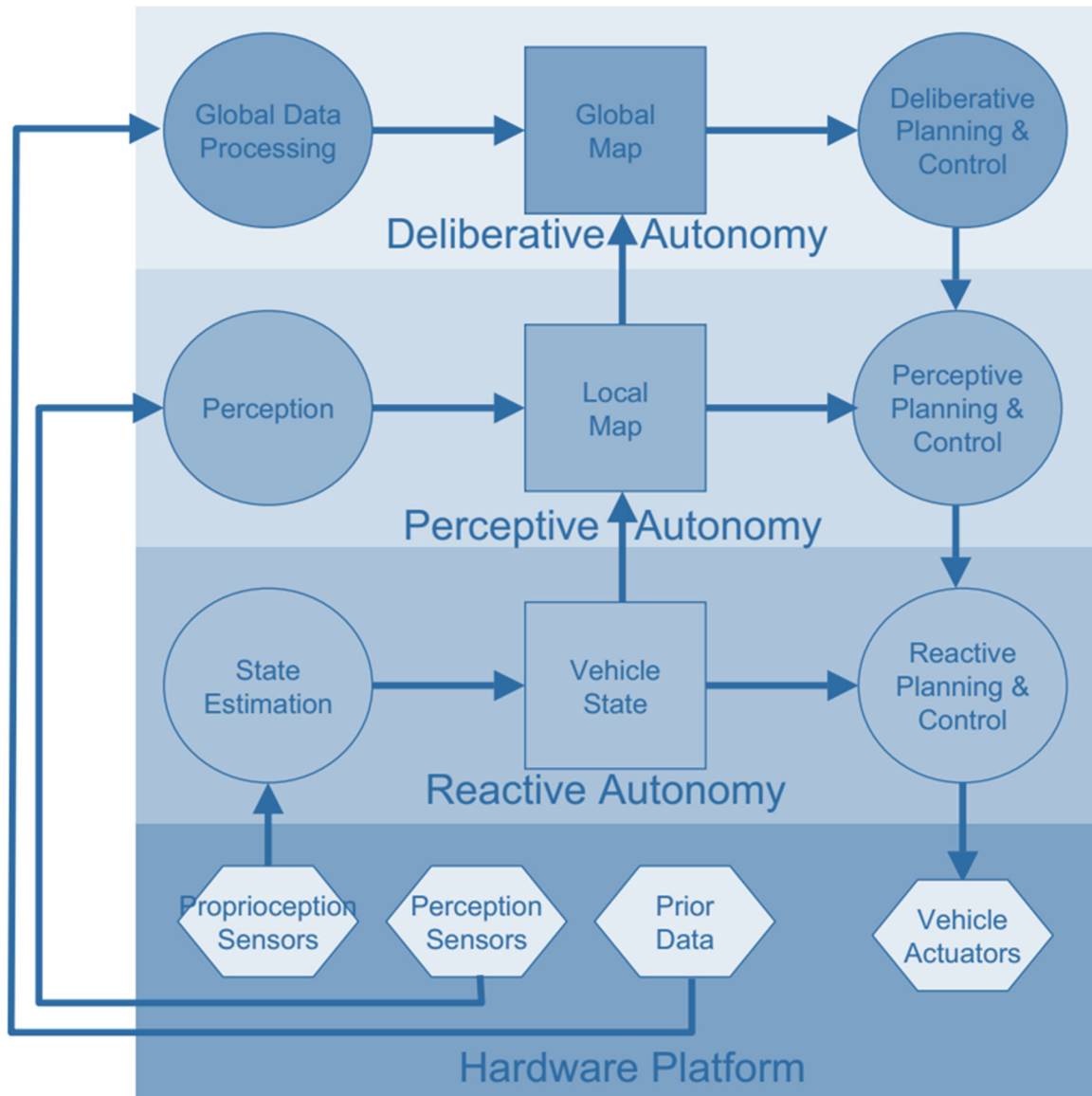


Figure 9: Multi-Layer Hierarchical Control for Reliable Autonomous Control

Steering schemes specific to trail terrain environments have been researched. ML models for predictive steering based on path detection were implemented to enhance the algorithmic trajectory calculations in Figure 10, [23]. Including input factors of current steering angle, vehicle speed, and trajectory, the regression model performed analyses to effectively learn and adapt to cases outside the initially implemented algorithm.

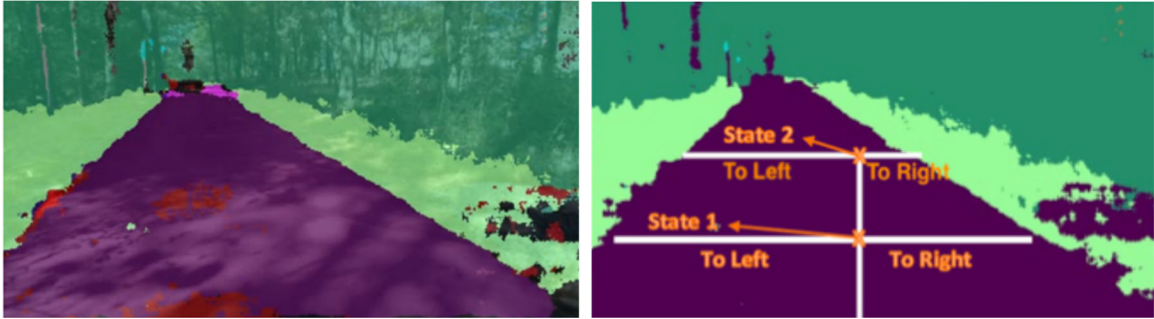


Figure 10: Machine Learning Steering Model for ATV

### 2.5.2 Environmental Factors

To traverse terrains with varying traction, it may be necessary to account for environmental factors such as wheel deflection, wheel slippage, tire tread penetration, and friction coefficients of local dirt, gravel, and asphalt textures. Studies of agricultural tires have found a maximum of 10% travel reduction in some instances of high soil deformation [24]. Hyperelasticity models have further been conducted to model the 3D finite analysis of tire interaction with various terrains [25]. Analytically, the factors presented in tire traction research are valid and impact navigation models in off-road autonomy applications [26]; however, the results are marginal in testing scenarios similar to the scope of this thesis and should therefore be negligible.

## CHAPTER 3: DESIGN OVERVIEW

Evaluation of the accessible and off-road capable vehicles at UNC Charlotte ultimately led to a previously customized senior design project tasked to build a rugged military prototype for the 2017 AFRL Design Challenge. This vehicle was designed for airlift seizures to aid troops by minimizing pack weight for special operations. The vehicle provided a great starting platform but would need a significant overhaul to perform reliable autonomous navigation.

### 3.1 Base Vehicle

The AFRL team chose the base platform to be a Scorpion HD Mini ATV. This vehicle featured a 120 cc 4-stroke carbureted engine with a centrifugal transmission including forward, neutral, and reverse gear selections. The team designed and built a modular chassis off the original vehicle frame to transport the mission gear and house the added electronic and mechanical components shown in Figure 11.

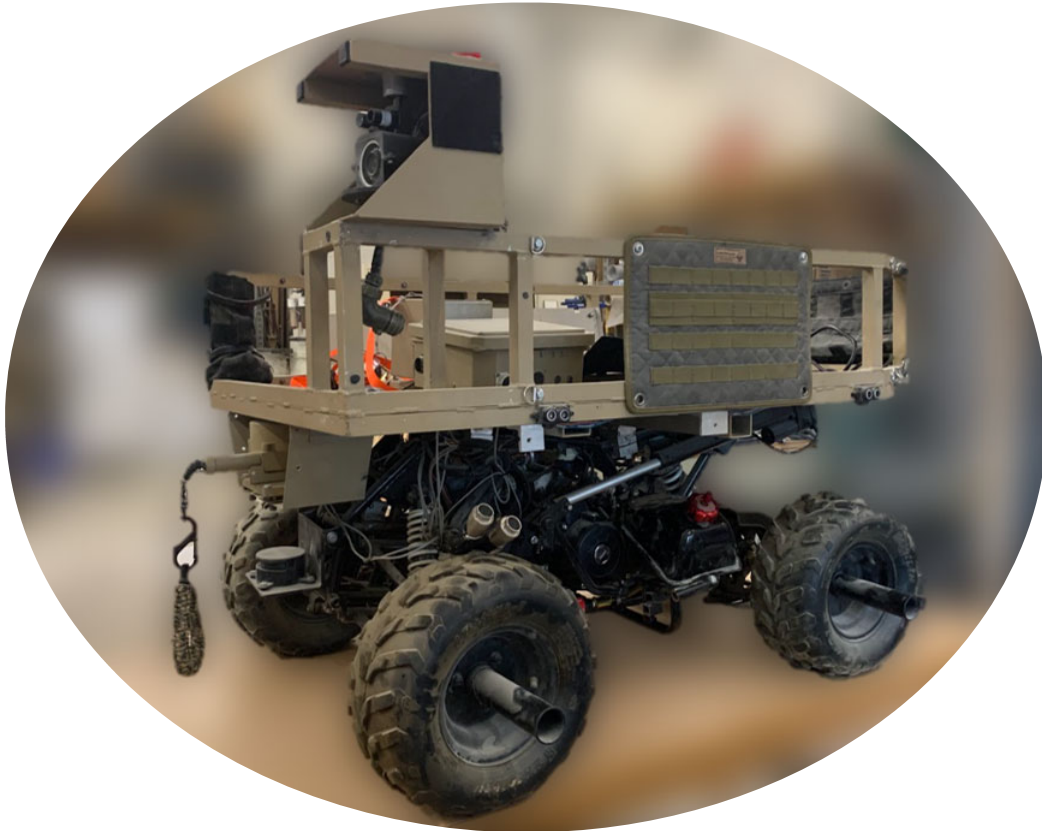


Figure 11: Initial State of Base Vehicle: ATLAS for 2017 AFRL Design Challenge

For the initially intended use, the team also implemented a servo actuated throttle cable, linearly actuated hydraulic braking system, linearly actuated gear selector mechanism, relocated gas tank, retrofitted fuel pump, and an offset 12 VDC Vex Bag motor actuated steering column. Additionally, two LiDAR systems, an IR camera, and a tether system were added to aid the semi-autonomous guidance system. In this form, the vehicle was named the All-Terrain Load-bearing Autonomous System, or ATLAS for short. The ATLAS was controlled via an NI myRIO microcontroller with the embedded LabVIEW graphical programming language.

### 3.2 Vehicle Contributions

The vehicle had not been used for the five years prior to this research. As expected, before beginning the baseline tests, several aspects of the ATLAS needed a refresh or replacement, such as the gas tank, fuel filter, air filter, and carburetor. The steering system was also damaged during the 2017 competition and required new gear sets in the Vex Versaplanetary gearbox, as shown in

Figure 12. The resulting steering ratio was converted to a 360:1 with a 10:1, 4:1, and 9:1 gear set inline.

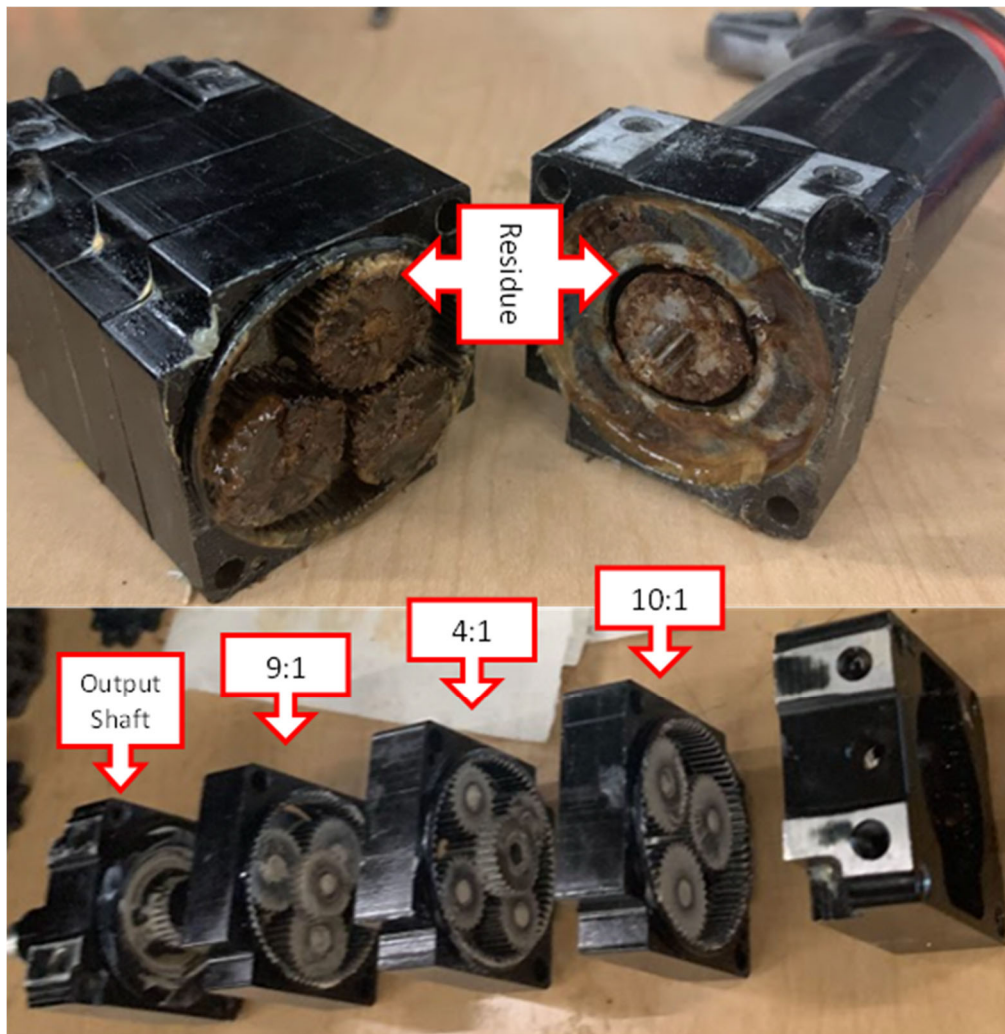


Figure 12: Before (top) and After (bottom) Steering Gearbox Refresh

During testing, it was determined that the onboard GPS unit was not accurate enough at short bursts of low speed to analyze the engine acceleration and velocity. The update speed for the GPS unit was not quick enough to provide a precise speed measurement as velocity is variable; however, it was very accurate at a constant velocity. To provide higher-fidelity speed calculations, a US Digital quadrature rotary encoder was added to the rear axle to interpret the counts per revolution. A simple VI was added in LabVIEW to calculate the actual wheel speed to verify against the GPS output. A structure was assembled from a recycled Vex Robotics classroom kit and a TETRIX MAX gear pack to minimize fabrication time. This structure supported the encoder freely outside the ATLAS chassis from an existing mounting location, as shown in Figure 13. The ID of an 80-tooth aluminum gear was bored to the OD of the rear axle and affixed between the two lock nuts with sufficient torque holding the rear axle centered within the rear trailing arm. This gear was oriented to mesh with a second 80-tooth aluminum gear to drive the concentrically installed encoder.

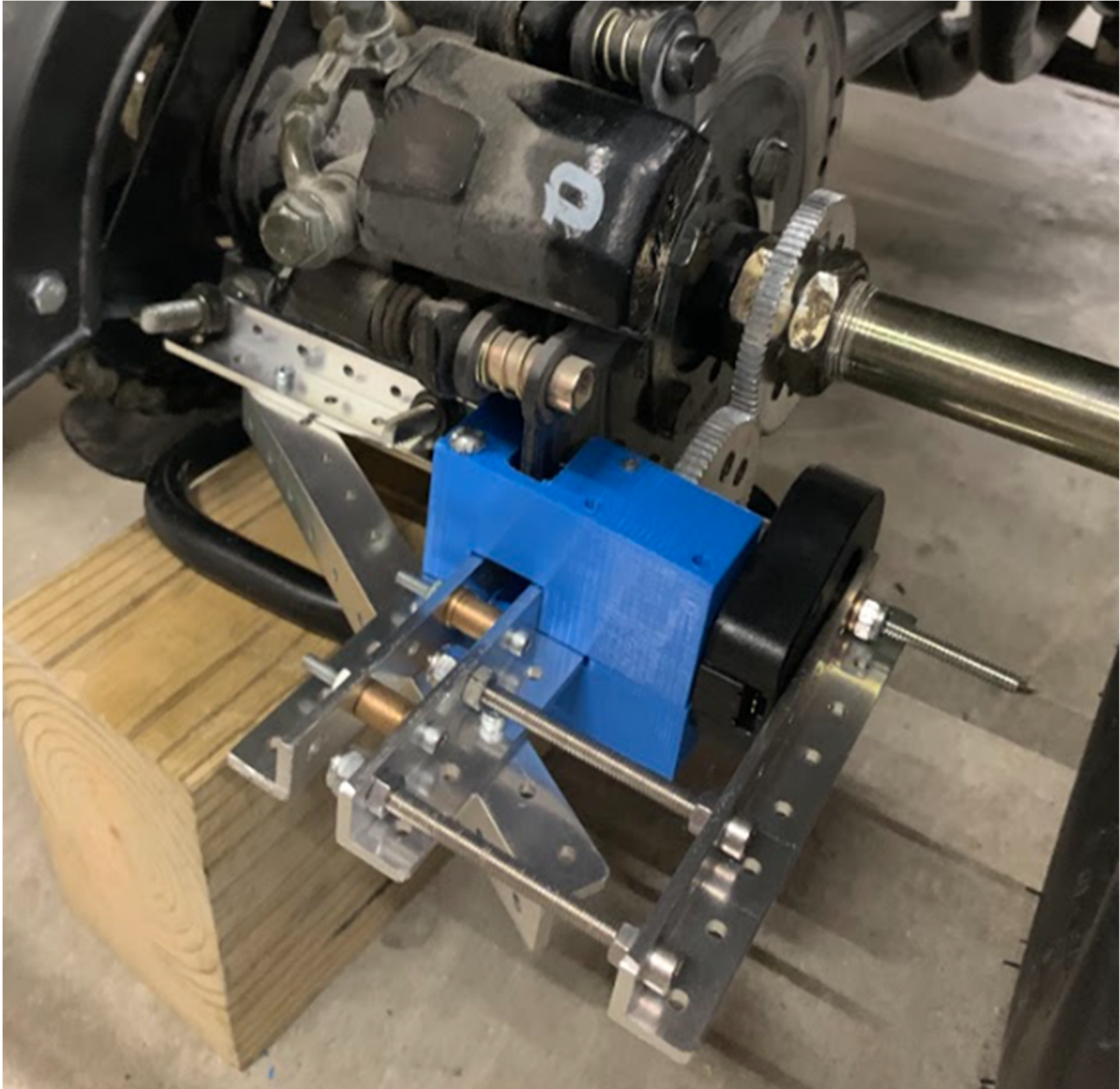


Figure 13: Implemented Design of Free-Structure Encoder

Another evolution of the initial base vehicle included a conversion of the braking system. The ATLAS originally had an Actuonix L16 linear actuator which was not designed to be constantly powered. The internal hardware was also not designed for a robust application, such as the required braking torque for the ATV. A rugged Uxcell 12 VDC torque motor was used in place, retaining the original threaded rod and circuitry within the actuator, as shown in Figure 14.

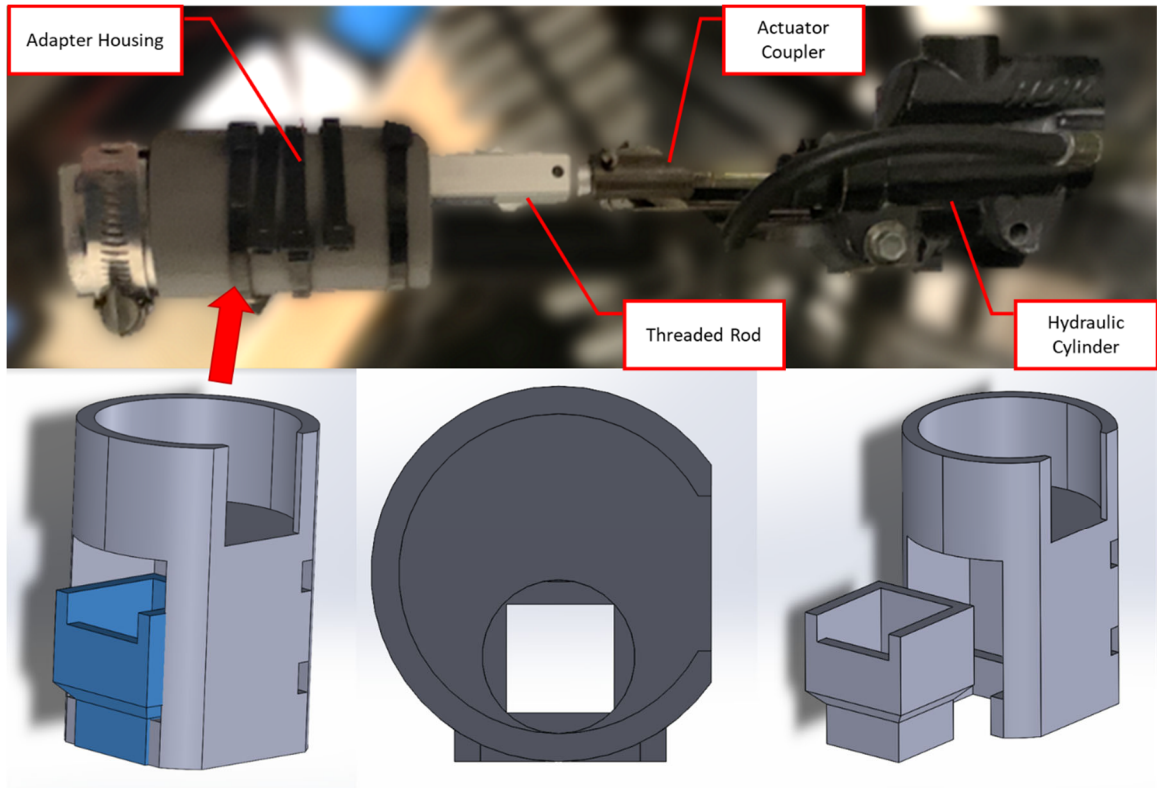


Figure 14: Retrofit Connection for Torque Motor and Linear Actuator Mechanism

### 3.3 EV Conversion

The ICE displayed several attributes that would not be conducive to autonomous control. The next step was to begin the design phase of the conversion, but first, the electric conversion of the ATLAS required a new name, the eATV.

#### 3.3.1 EV Conversion Kit

Upon researching commercially available motors, it became apparent that few plug-and-play options would be available in the budget-conscious price range. Especially in a time of an international shipping crisis, the options to procure an inexpensive electric motor capable of powering a 140 kg vehicle were somewhat limited. The selected Vevor conversion kit included a 48 VDC 2000 W motor and supporting motor controller

designed for sprocket-driven applications. This kit, shown in Figure 15, was initially designed for small scooters, go-karts, or ATVs where the user would manually control a twist throttle.

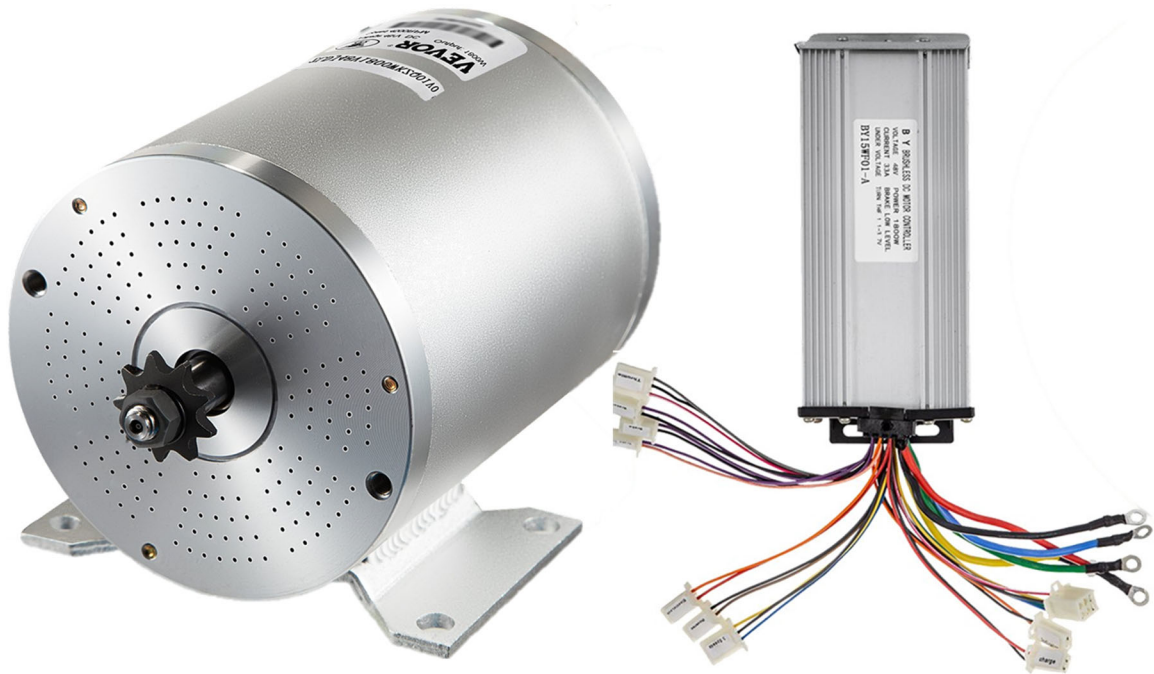


Figure 15: Vevor 48 V 2000 W Electric Conversion Kit

The EV conversion kit included additional manual switches for speed selection, keyed ignition, and brake lamp indicator. The keyed ignition and speed selection were intended to be retained, so relays were implemented to complete the circuit as commanded by the myRIO. The 48 V system for the motor and motor controller consisted of 4 SLA1116 12 V 18 Ah batteries configured in series. The resulting working voltage of 46-54 V was confirmed acceptable for the kit. The maximum rated current requirement for the motor was specified as 36 A. The theoretical maximum run time would be 30 minutes at maximum throttle using Equation 1.

$$\text{Run Time} = \frac{\text{Rated Capacity}}{\text{Maximum Current}} \quad [1]$$

### 3.3.2 Conversion Design

Beginning the conversion, the ICE and other engine-critical components were removed from the vehicle. The ICE, transmission, gas tank, starter, ignition coil, stator, carburetor, throttle servo and linkage, PCV valve, fuel pump, and fuel pressure regulator were no longer necessary and removed.

To enable the maximum performance of the new electric motor, the gear reduction needed to be reduced further than the original 12:45 ratio of the ICE configuration. Material was recycled from a previous course project to reduce the cost of the design implementation; the mechanism included two standoffs and two pillow bearings to support an axle. Likewise, a solid half-inch aluminum base plate was recycled from the project and designed to withstand the dynamic loading as mounted on an off-road vehicle.

Using two chain-and-sprocket assemblies, the gear reduction was reduced to 13.02:100 final drive ratio with the intermediate axle. The intermediate axle allowed the motor to drive a 10:40 ratio, thus translating the rotational orientation to a 25:48 ratio. Figure 16 details the overall conversion mechanism, which retains the rear axle configuration.

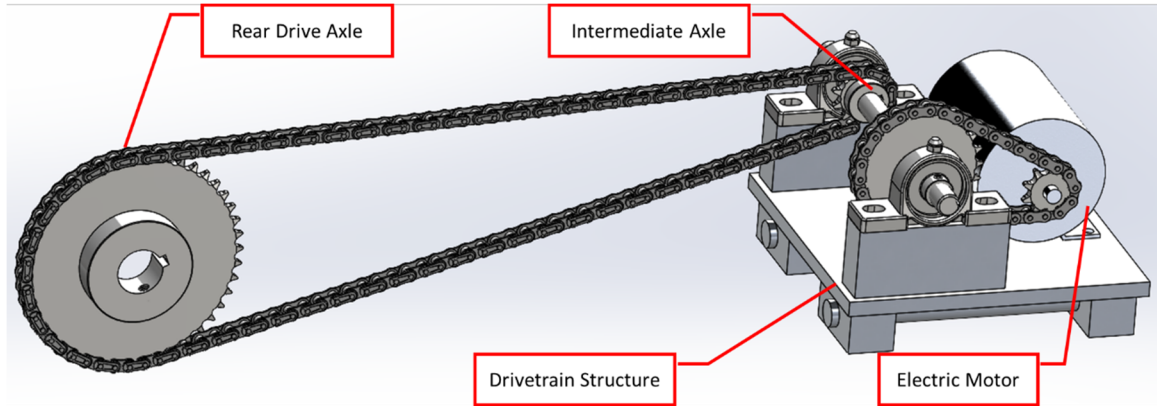


Figure 16: EV Conversion Drivetrain Assembly

After the initial design was assembled and implemented, it was found that the chain would not clear the vehicle's frame when under load. A simple fix required the drive chain and sprocket to be relocated on the opposing side of the pillow bearing and the rear sprocket to be spaced off the rear axle an equivalent amount, as shown in Figure 17. A Delrin spacer was fabricated to offset the rear sprocket.

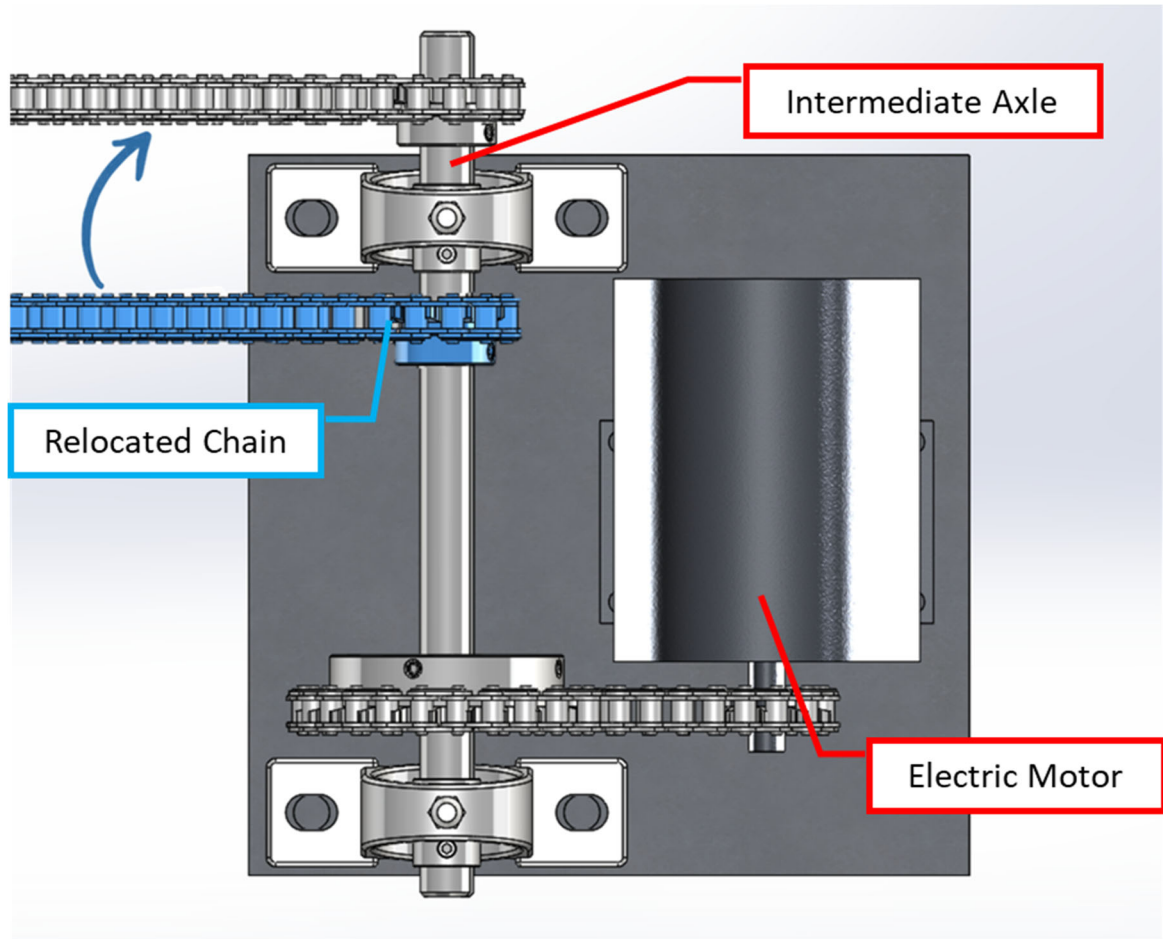


Figure 17: Post-Install Modification to EV Drivetrain Assembly

Figure 18 displays additional views of the intermediate reduction from the electric motor. The base plate is attached to the original vehicle frame tubing at the base of the ICE mounting location. The weight savings from the conversion totaled 2.75 kg in fully operational condition, batteries included. The conversion design could easily be optimized for the specific loading provided by the motor parameters, gear reduction, and vehicle weight to reduce material costs and weight overall.

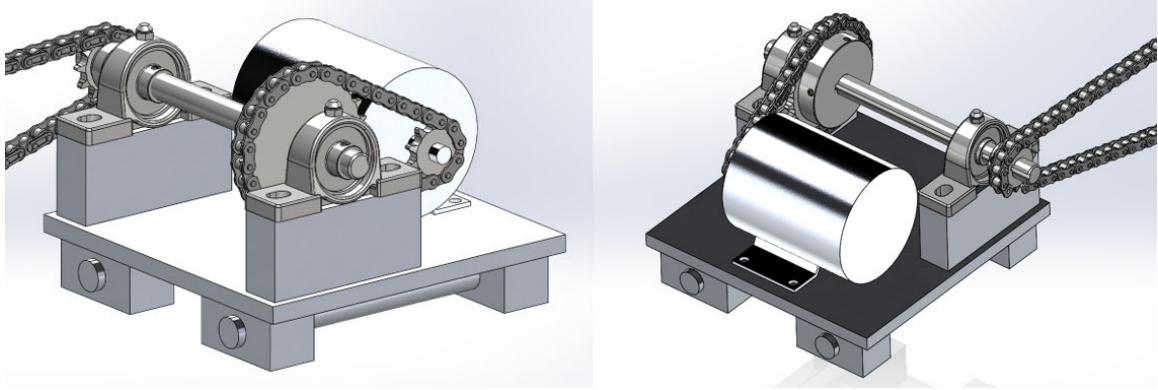


Figure 18: Rear Dimetric (left) and Front Isometric (right) Views of the Revised Assembly

### 3.3.3 EV Power Modeling

Following the initial power calculations, a digital twin of the eATV drivetrain was generated to calculate an expected acceleration and current draw. Using MATLAB, parameters of the vehicle, electric motor, and battery bank were incorporated.

First, the electrical and mechanical aspects of the electric motor were entered in the Motor & Drive block available in MATLAB Simscape. The maximum torque, maximum power, and rated motor speed were derived from the Vevor manual. The torque control time-constant was left as default from the Motor & Drive block, while the motor efficiency and efficiency torque were estimated based on calculations from similarly capable motors with available motor curves.

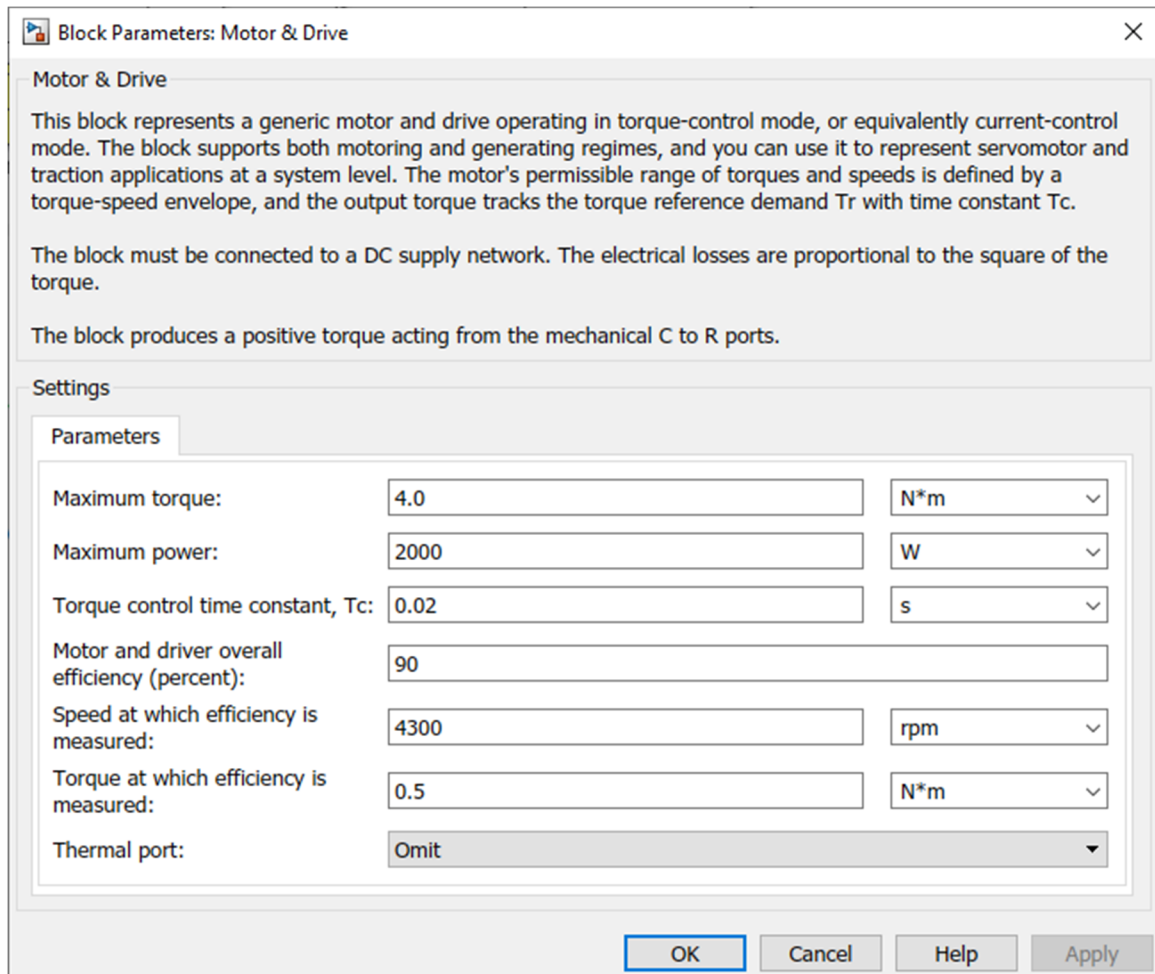


Figure 19: MATLAB Motor & Drive Block Parameters

The Motor & Drive block feeds directly into a model representing the dual chain system and retains the translation and gear reduction of the motor output. The output of the chains linked in series is directed as the input for the Longitudinal Vehicle block. This block was given a vehicle mass, tire radius, and frontal area of  $0.5 \text{ m}^2$  calculated from the eATV. A rolling coefficient of 0.05 was interpolated from [27] while the air drag coefficient and constant gravity were left as default from the Longitudinal Vehicle block.

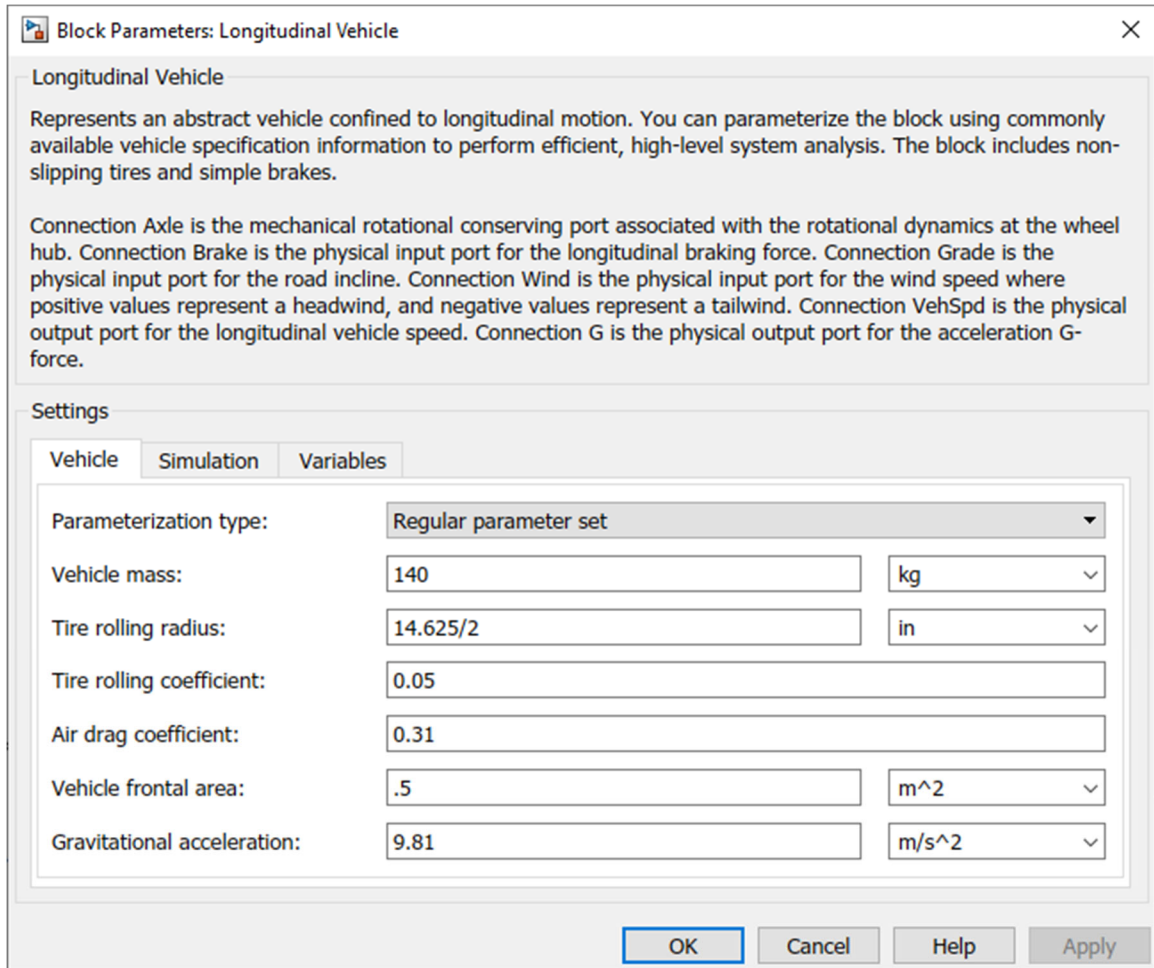


Figure 20: MATLAB Longitudinal Vehicle Block Parameters

The model below shows the final drivetrain control system block diagram in MATLAB Simscape. A PID control system was integrated to increase the simulated throttle [28], increasing the vehicle speed to a determined input setpoint. A KP value of 0.6 and a KI value of 0.1 were determined to most accurately represent the modeled vehicle by experimentation, as shown in Figure 21.

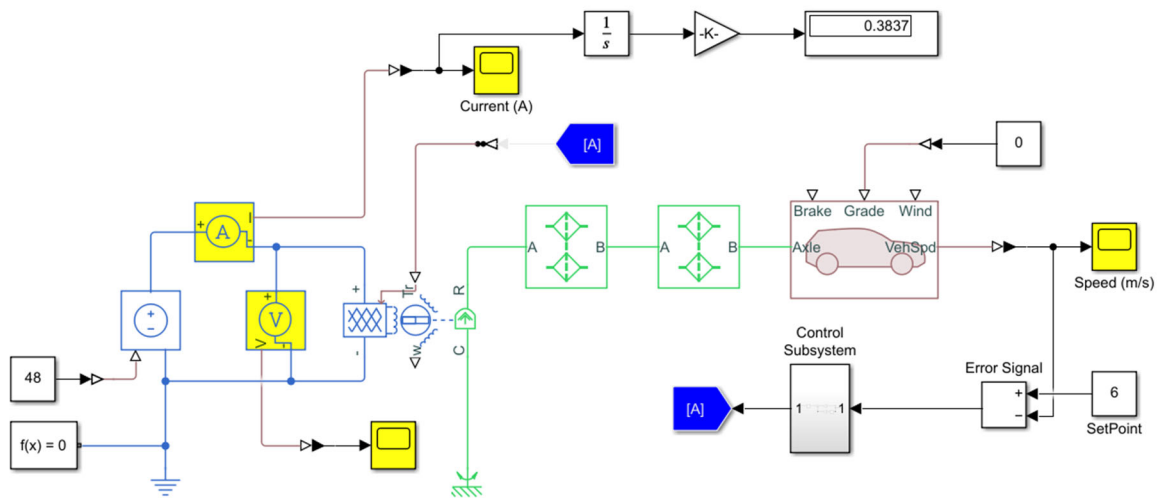


Figure 21: MATLAB Simscape Simulation of eATV

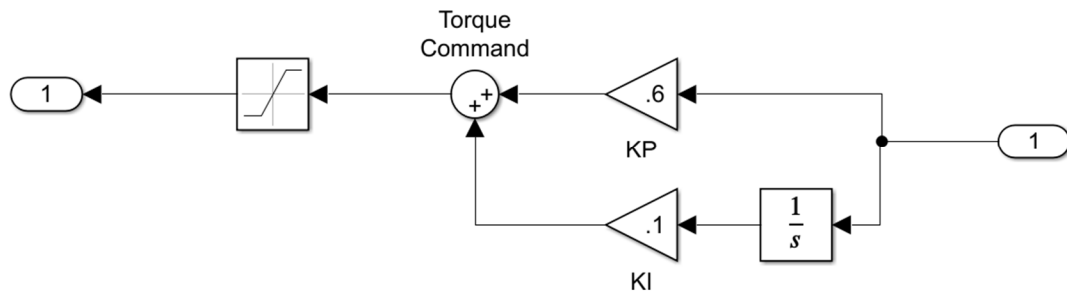


Figure 22: Proportional and Integral Control for Vehicle Speed Simulation

The output plot comparing the anticipated current draw at the 2.5 m/s targeted velocity is displayed in Figure 23. Since the control scheme does not include a derivative gain, the simulation calculates a peak current draw nearing 15 A when accelerating to the velocity setpoint. The significance of the current draw simulation is to ensure that the maximum expected current draw remains in a manageable range for the battery array and EV conversion motor controller.

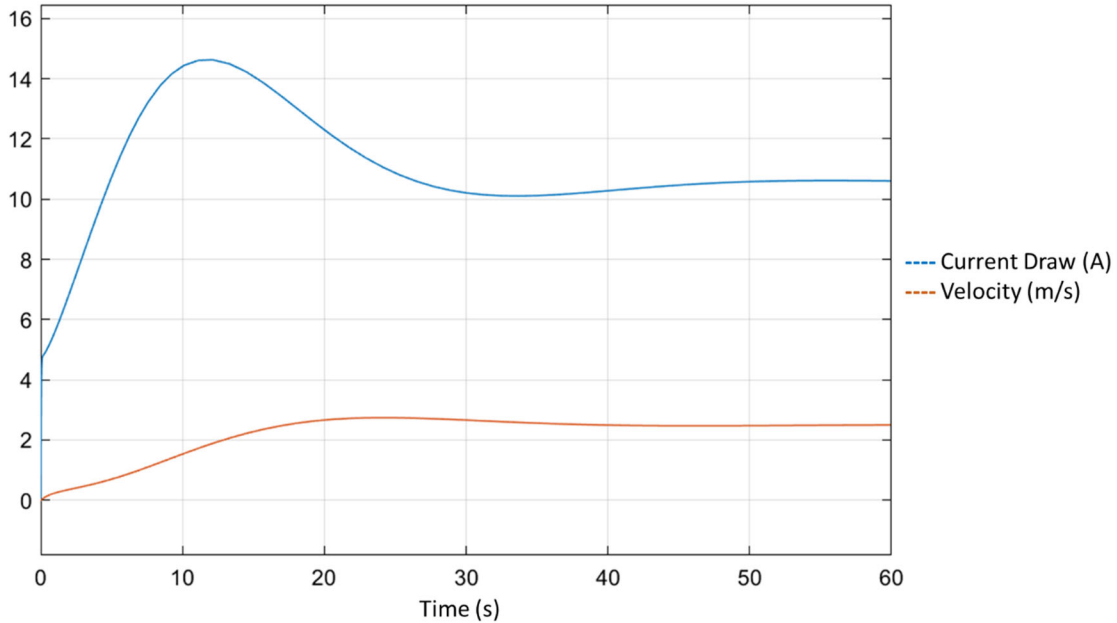


Figure 23: MATLAB Simulation: Current Draw at 2.5 m/s Target Velocity

The anticipated current draw for the 6 m/s targeted velocity is displayed in Figure 24. The peak current draw reaches the maximum current rating of the EV conversion kit at 42 A. The acceleration to the higher velocity setpoint draws more current from the battery array, however, still levels off to 20 A at a steady-state velocity. The EV conversion kit is rated for a continuous 34 A, so the maximum tested speed of 6 m/s (13 MPH) will not stress the system. Additionally, the PI controller simulates a worst-case scenario, where an applied derivative gain would account for various factors and gradually accelerate the current draw. A model with a derivative gain would not illustrate the immediate overshoot as displayed from the discussed model.

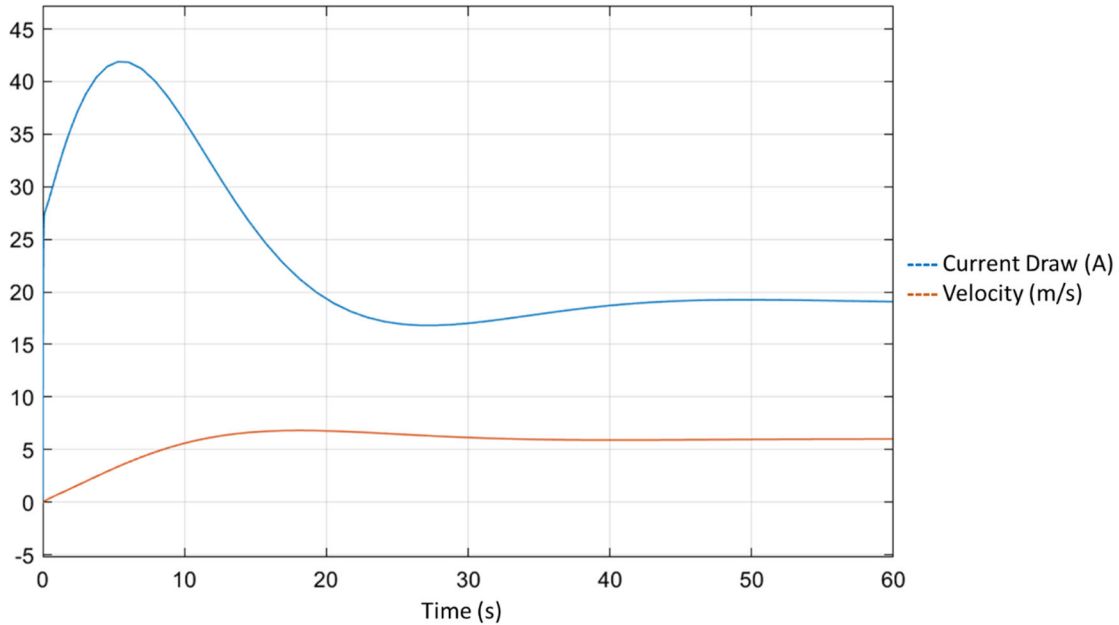


Figure 24: MATLAB Simulation: Current Draw at 6 m/s Target Velocity

### 3.4 System Architecture

The control program for the eATV was developed in NI LabVIEW. The ATLAS vehicle was originally developed using this programming language and it was decided best to retain the original programs for baseline testing. Methods for computing, sensing, and actuation were implemented in the LabVIEW language to integrate some of the existing features of the ATLAS. Computing was conducted using an embedded controller and a combination of laptop devices. Sensing was obtained from a ground speed encoder, GPS unit, and camera system. Actuation was implemented for the steering, braking, and throttle subsystems in addition to the emergency stop devices.

#### 3.4.1 Computing

The NI myRIO served as a processing unit for the eATV. This microcontroller can receive compiled LabVIEW programs as machine code, providing an entry-level



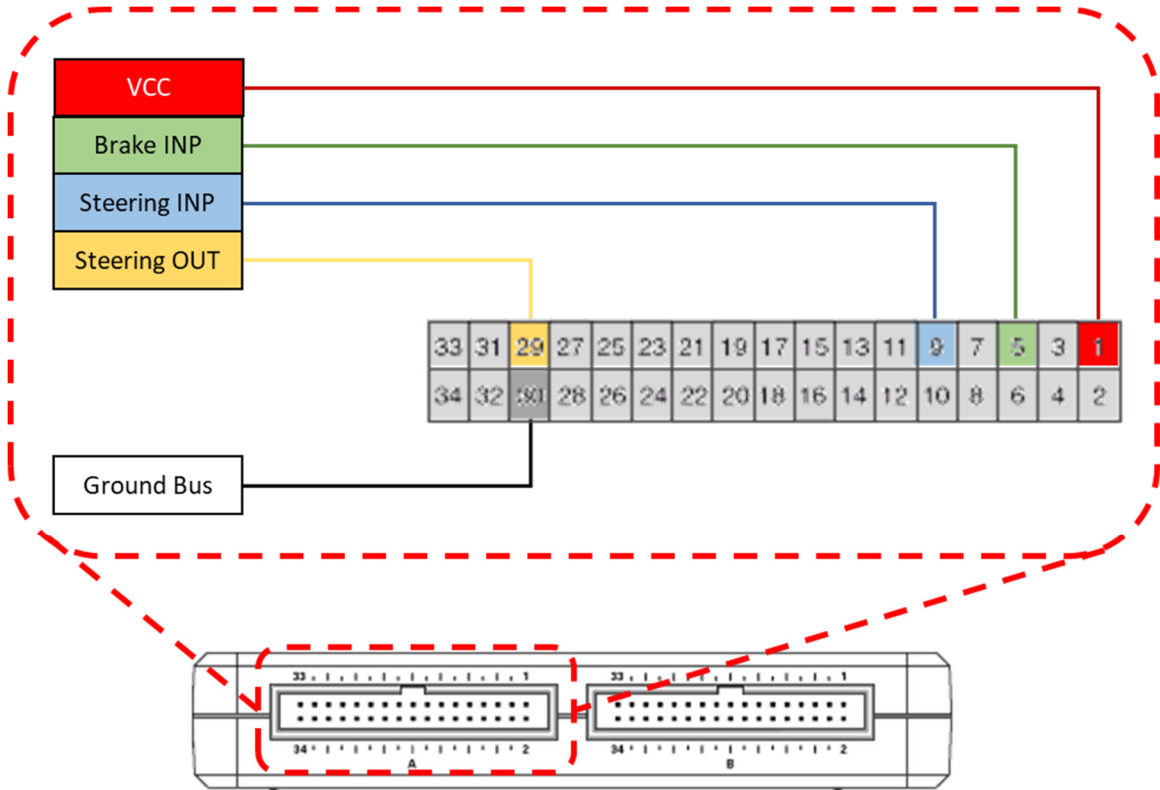


Figure 26: Implemented myRIO Expansion Port A

Figure 27 illustrates the main hardware components connected to the myRIO on port B

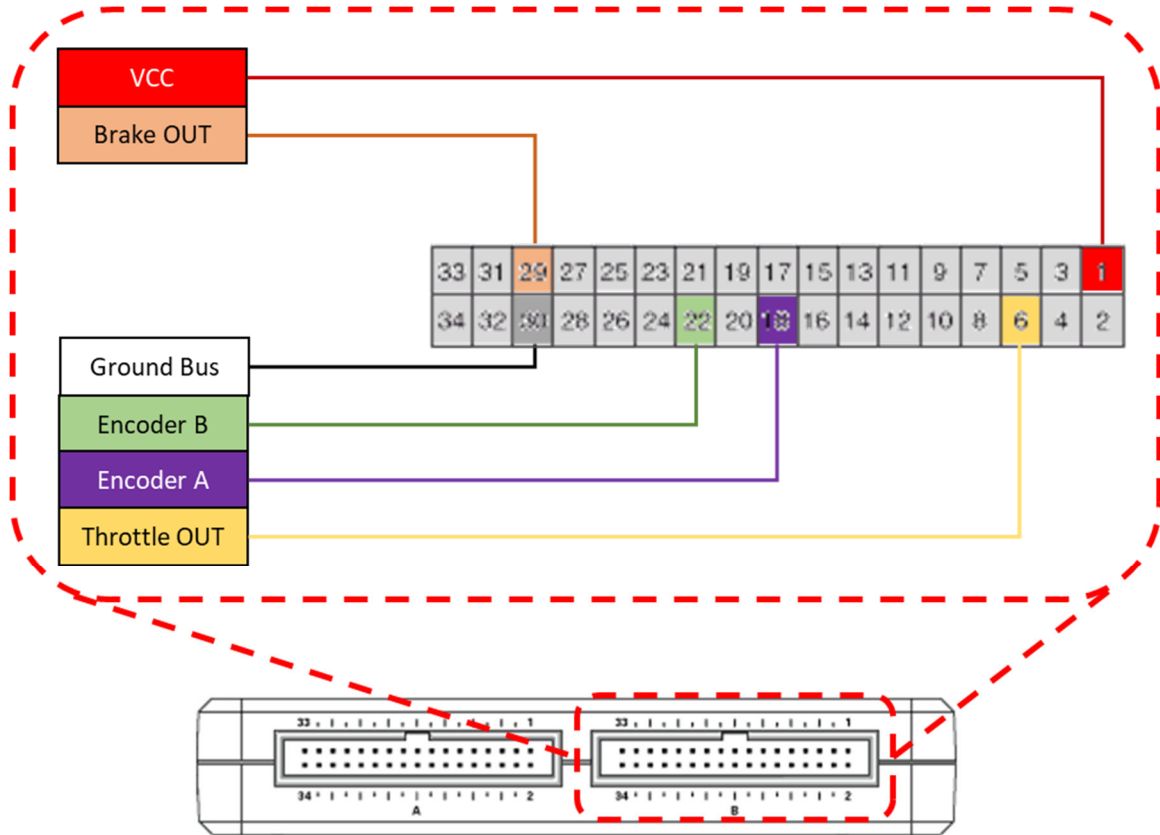


Figure 27: Implemented myRIO Expansion Port B

A vehicle laptop was placed on the eATV to enable remote control testing. The laptop receives user input via Bluetooth from the Xbox One® controller and remotely shares variables to the myRIO via WiFi. An off-vehicle base-station laptop was also connected via WiFi to control and record the main programs running on the myRIO. Figure 28 displays the hardware configuration for the remote-control testing scenario. The rightmost laptop was used as the user base station, while the leftmost laptop resided on the vehicle and communicated with the user controller. The configuration was designed for convenience by allowing the main computing hardware to be off of the vehicle and readily accessible for troubleshooting or on-site programming as necessary.



Figure 28: Hardware Configuration for Remote Vehicle Control

Figure 29 illustrates the revised hardware configuration following the EV conversion for autonomous trail navigation. The user base station was removed from the setup and replaced with an RGB-D camera to relay vision data to the laptop for autonomous control.



Figure 29: Hardware Configuration for Autonomous Vehicle Control

### 3.4.2 Sensing

#### 3.4.2.1 Ground Speed Encoder

The US Digital quadrature encoder [29] added to the rear axle of the eATV is powered by a 5 V supply. The encoder algorithm converts the number of pulses per time constant to determine the ground velocity in MPH.

#### 3.4.2.2 Intel RealSense

The Intel RealSense D455 depth camera offers a 16 m range in the Z-direction and a 90- and 60-degree FOV in the X and Y directions, respectively. Using the RealSense Viewer application, the camera can be fine-tuned for an accuracy of less than 2% at 4 m [30]. To interface with the myRIO, RealSense offers an SDK with several example files to access and command the RealSense API from LabVIEW. This interface and the IMAQ Vision and Motion module in LabVIEW opened the gateway for obtaining

color, monochrome, and depth imaging simultaneously for real-time simulation. NI Vision Assistant is a tool that includes abundant vision processing libraries that can be used to manipulate RGB color scales, apply ROIs and masks, and perform binary analyses. The existing base algorithms serve as a good foundation to begin developing terrain-specific image processing techniques. Throughout the eATV system code, the Intel RealSense vision is evaluated in Vision Assistant to perform navigation maneuvers accordingly.

### 3.4.2.3 GPS

The GlobalSat BU-353s4 GPS module was implemented on the ATLAS and retained in the design of the eATV. The device is readable in the LabVIEW software, providing access to the unit's latitude, longitude, heading, and velocity. The GPS unit was connected via USB 2.0 to the myRIO and mounted to the topmost portion of the vehicle structure.

### 3.4.3 Actuation

#### 3.4.3.1 Steering Sub-system

ATVs are commonly steered using a human-actuated handlebar, providing a leverage system to rotate a steering column. The steering column turns a rack, forcing the front wheels either left or right simultaneously. The ATLAS vehicle implemented an offset steering column to be actuated by a DC motor. Using a DC motor to achieve precise positioning is impossible without feedback. A rotary encoder with an axis of rotation aligned along the offset steering column was implemented to obtain positional

feedback during actuation. The ATLAS steering program was implemented with a pulsing method to actuate the motor in the desired direction for short bursts to allow ample time to receive position feedback from the steering sub-system. The steering program was enhanced for the eATV to increase the frequency of pulses and lower the motor duty cycle. As the DC motor pulses to achieve an input position, the feedback loop has time to calculate its current position and choose to continue pulsing or pause.

#### 3.4.3.2 Braking Sub-system

The stock ATV features a hydraulic braking system actuated by a rider via a hand lever. To remotely actuate the hydraulic cylinder, a linear actuator was implemented on the ATLAS to compress the hydraulic cylinder. The linear actuator implemented on the ATLAS was prone to failure due to the small size and loading experienced in the mechanism. The actuator was upgraded to feature a 100 RPM Uxcell torque motor, providing ample torque to actuate the hydraulic braking system. The actuator can achieve 0.333 inches per second in the forward brake-applying direction while retaining the original Actuonix threaded rod mechanism.

The myRIO was programmed to send commands to the linear actuator via a signal wire. A potentiometer provides a percentage of 5V from the circuit as an input to the myRIO. As the actuator nears the maximum extended or retracted positions, the myRIO is programmed to command the retrofitted torque motor to slow to a stop before over-manipulating the mechanism.

### 3.4.3.3 EV Conversion Kit

The procured EV conversion kit included an electric motor and motor controller designed with a proprietary interface. A method to interface with the added motor controller was developed. The EV conversion kit can be operated with minimal input to the motor controller besides actuating a keyed switch and providing a 0-5 V supply from a twist throttle. When actuated, the keyed switch interrupts the throttle signal, thus preventing unwanted motion. Actuating this switch remotely via the myRIO was deemed an intermediate E-stop for the eATV.

However, since the kit was for a 48 V system, the keyed switch operated by interrupting the connection between two low-amperage 48 V wires. A relay was added to indirectly apply a connection between the existing wires from the Vevor motor controller, as the myRIO cannot supply 48 V.

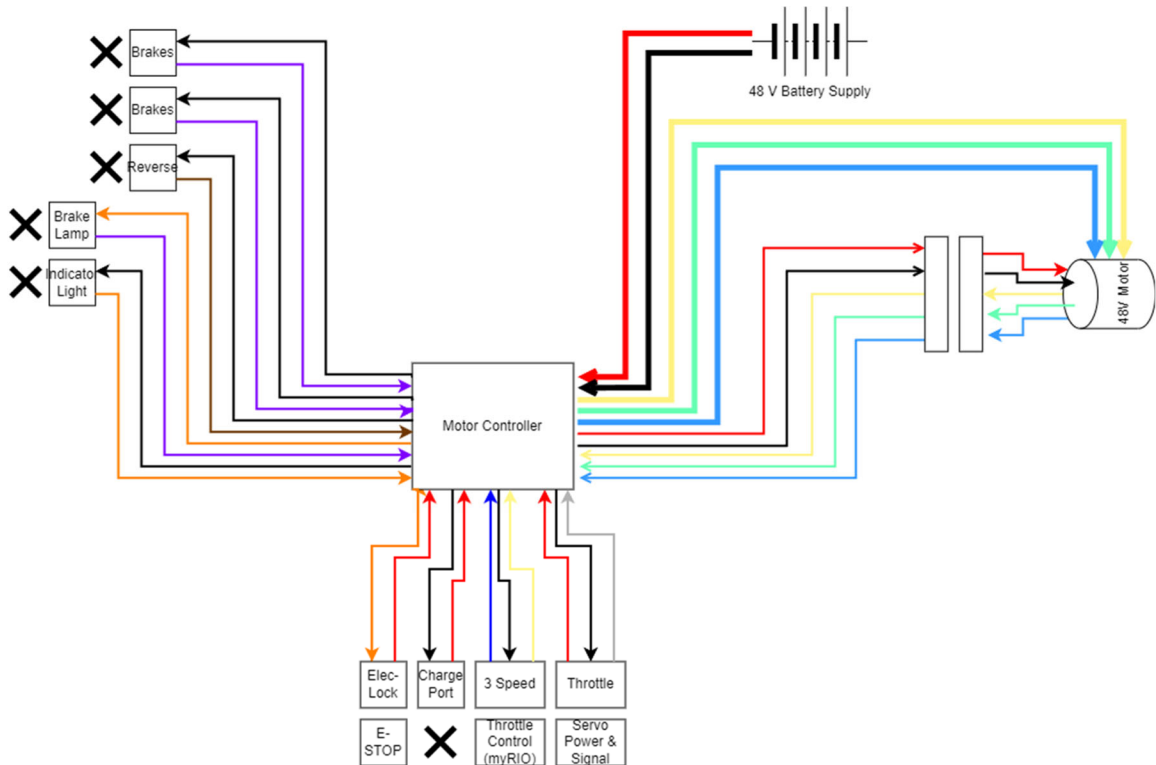


Figure 30: Vevor Motor Controller Wiring Diagram

#### 3.4.3.4 Throttle Sub-system

The stock ATV included a hand-actuated throttle which actuated a cable-drive carburetor. The ATLAS implemented a 3-wire servo to remotely actuate the throttle cable when supplied a 0-5 V signal. For applications such as the stock ATV, the EV conversion kit was also designed for use with a hand-actuated throttle. The drive motor controller receives a signal via a 0-5 V potentiometer within the throttle mechanism. To control the eATV, the existing wiring for the ATLAS throttle servo was rerouted to the drive motor controller in place of the hand-actuated twist throttle. This also allowed the original myRIO pinout for the throttle to be retained. The output PWM signal was changed to a scaled 0-5 V, calibrated from the hand throttle attachment included in the EV conversion kit. When a constant 5 V was applied, the hand throttle would proportionally output 0.85

V to 4.25 V as twisted throughout its range. From the experiment, it was confirmed that the mechanism used a potentiometer.

#### 3.4.3.5 Emergency Stop

To stop the drivetrain in an emergency, a wireless E-stop was implemented to transmit a control signal to a receiver on the eATV. When actuated, the signal removes power from a relay to unlatch the NC circuit where the electric drive motor is enabled. Additionally, a manual E-stop is located at the topmost portion of the eATV chassis to allow for de-powering the electronics in an emergency. In the event of an operating malfunction, the user can wirelessly remove power from the electric motor and then manually press the electronics E-stop if necessary.

### 3.5 Cost of Conversion

The total cost of the electric ATV prototype is displayed in the eATV conversion totals \$2,430.24, accounting for the EV Conversion kit, Vex motor controllers, motor and gearing structure, myRIO, relays, and the Intel RealSense d455 depth camera.

Table 1: Categorized Cost of Prototype and eATV

Category	Expense
Base Vehicle	\$1,499.99
Steering	\$148.33
Braking	\$109.99
Computing	\$2,664.00
EV Conversion	\$759.76
Vehicle Control	\$1,251.48
Vision	\$419.00
Electrical Hardware	\$196.89
Mechanical Hardware	\$2,035.00
Total	\$9,084.44



eATV Platform  
\$2,430.24

## CHAPTER 4: METHODOLOGY

An onboard computer is programmed to drive the myRIO code in response to the processed RGB-D vision data. Obstacles are detected in a timely manner and avoided appropriately using the mobility system. In instances of GPS denial, the vehicle may continue traversing the environment until the next waypoint is achieved. Testing methodologies took place on the UNC Charlotte Fitness Trail along a 500+ m predetermined route. The route is predetermined to ensure the target for the vehicle is an achievable trajectory on the given trail.

### 4.1 Vision Processor

The SDK for LabVIEW was accessed to streamline the integration of the Intel RealSense D455 depth camera. The custom Vision Assistant algorithms were accessed via IMAQ to interpret the captured color and depth images within LabVIEW. In real-time, the eATV vision program implemented a Vision Assistant express VI for path detection via converting the color image to a binary form following the provided contrasting appearance. The program also implemented an analysis of the pre-established depth image for path estimation, obstacle detection, and pedestrian detection. This image was obtained from a screengrab using an IMAQ Extract tool. External pop-up displays within LabVIEW provided the user with a visual cue for troubleshooting purposes on the EUD. All vision scripts were performed remotely on the laptop base station to minimize the computational workload on the myRIO.

#### 4.1.1 Color Vision

The example color image displayed in Figure 31 represents an asphalt portion of the UNC Charlotte Fitness Trail. The image was first processed using an HSL-Saturation color plane extraction, scanned for a threshold of 0-25 for dark objects, and lastly, an advanced morphology and particle analysis were conducted to fill holes and remove unnecessary noise.



Figure 31: Binary Path Detection: Upper Left (UL): Color Image, Upper Right (UR): Saturation Plane. Lower Left (LL): Binary Threshold, Lower Right (LR): Advanced Morphology

#### 4.1.2 Depth Vision

The example depth image displayed in Figure 32 represents the same previous instance of the UNC Charlotte Fitness trail, only using the RealSense depth SDK for LabVIEW. The goal of implementing depth imaging for path detection is to consider the surrounding environment and target the objects furthest away. A color plane extraction of

the green plane was conducted to allow depth data to be interpreted as an intensity plot in the image. Next, a threshold analysis of 0-12 was performed to highlight the far regions then advanced morphology was used to encapsulate the geometry. To determine the location of the targets, a circle detection method was implemented to generate the largest circle in an area and compute the X- and Y-pixel coordinates for each circle. From that, a steering methodology was implemented.

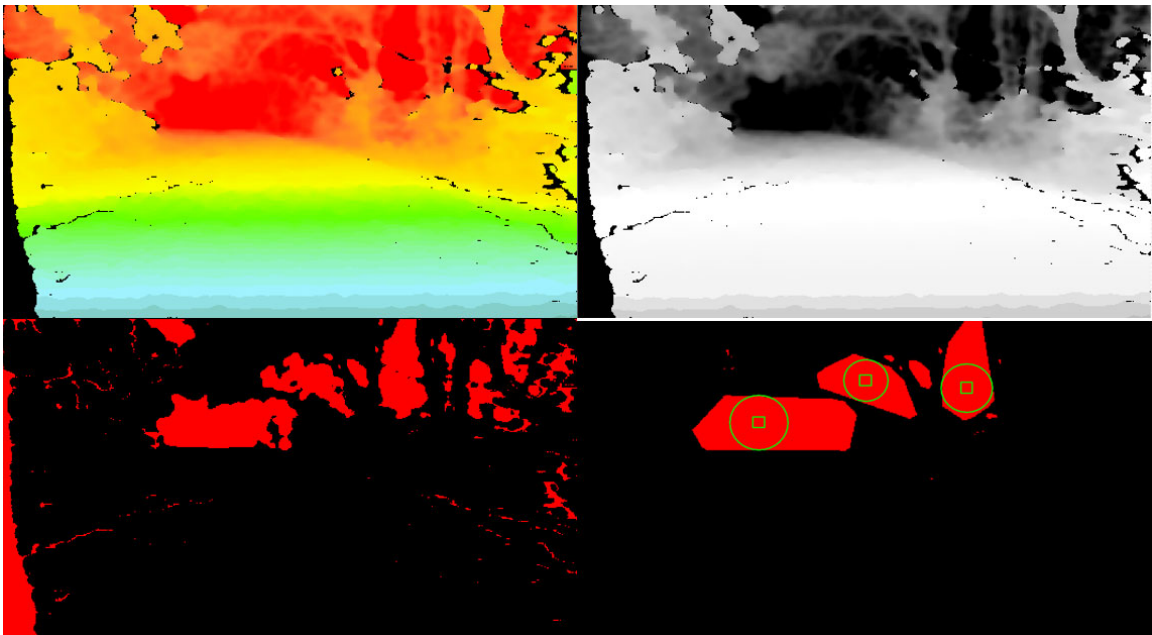


Figure 32: UL: Depth Image, UR: Color Extraction, LL: Binary Analysis, LR: Circle Detection

#### 4.1.3 Obstacle Detection

To evaluate potential obstacles found in the construction or maintenance of the trail environments, a traffic cone, warning sign, and large barrel were placed for processing and obstacle avoidance. This method used depth imaging to locate a specific color in an ROI, as seen in Figure 33. The depth image was first masked to display the upper half only. A color plane extraction of the green plane was performed and converted to binary similar to the distance target, though only for bright images. Circles are then

applied to the advanced morphology geometries and can be used in the mobility system for avoidance as located areas of interest.

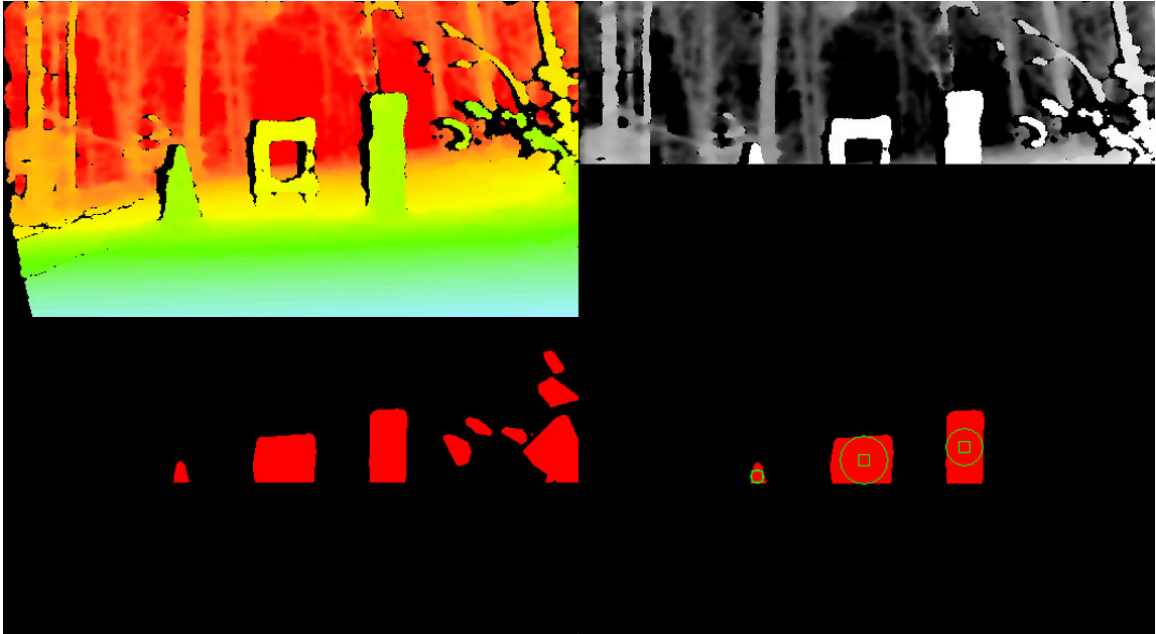


Figure 33: UL: Depth Image, UR: Masked Color Extraction, LL: Binary Analysis, LR: Circle Detection

Pedestrians were considered unique obstacles, so they were identified using an enhanced obstacle detection algorithm. Steps 1 and 2 are the same across both means of obstacle detection; however, pedestrians are matched against a file of example pedestrians viewed in the depth image as displayed in Figure 34. The vision scripts were developed to interpret the image and display an ROI around the targeted pedestrian and assign a numerical quantity and the location of each with a success rate of 85.0 to 97.5%.

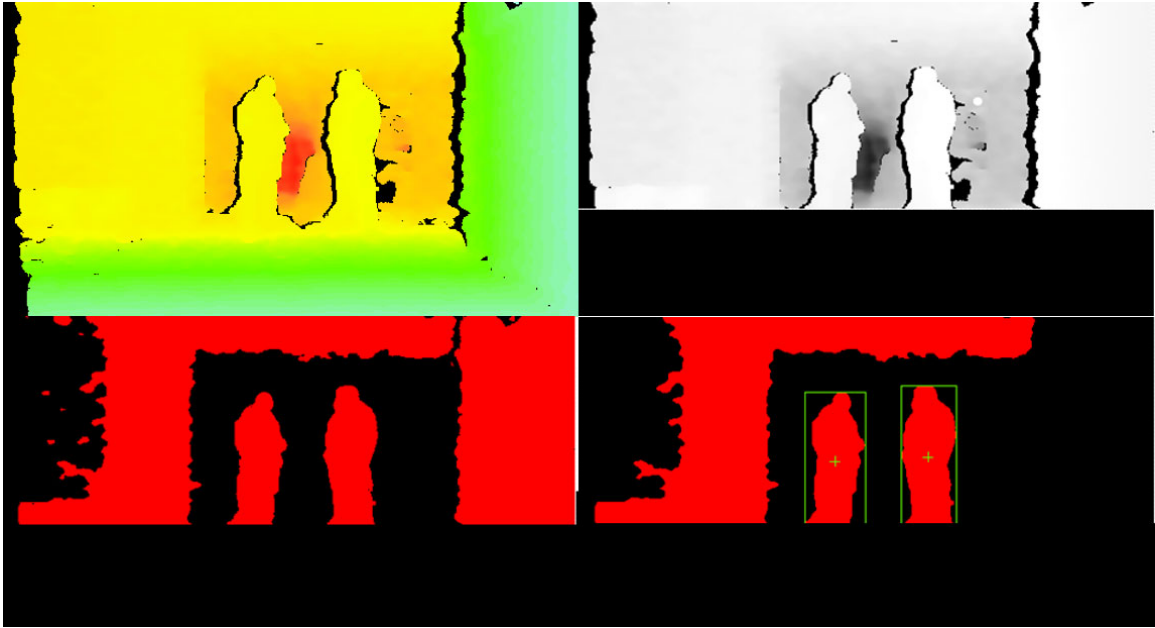


Figure 34: UL: Depth Image, UR: Color Extraction, LL: Binary Analysis, LR: Shape Matching

## 4.2 Mobility System

Following the computer vision analyses, remote variables were adjusted and shared with the myRIO to send commands for the steering, braking, and EV system accordingly. With the primary approach determined to use depth imaging, an image with at least one circle within a specified ROI is prioritized over the path detection from the color image. Initial testing determined that the located areas of interest are more likely to be the trail direction when closest to the horizon versus higher in the Y-direction.

### 4.2.1 Depth Vision Mobility

A scaled weighting was applied to the image in a simplified FOV region achievable by the steering maneuverability to accommodate this realization. A value of four was placed in the center to weight the region appropriately, and a linear decline was applied from the center out to +X and -X in the cartesian directions 3 to 1 and -3 to -1,

respectively. The negative value provides a sense of direction left or right for the steering program. In the Y-direction, to exponentially increase the weights from top to bottom of the ROI, an exponential trend of 2 to 5 to 11 to 23 was introduced. When multiplied through the region, this combination retained the weights under 100 numerically to define the weightings as percentages, as shown in Figure 35.

The three distinct circles were applied to geometries of interest using a developed processing algorithm. The centroid of the largest apparent circle in the geometry was recorded and used in calculating the general location of the most likely trail direction. Figure 34 displays the lower left circle in cell -22 as the successfully selected geometry.

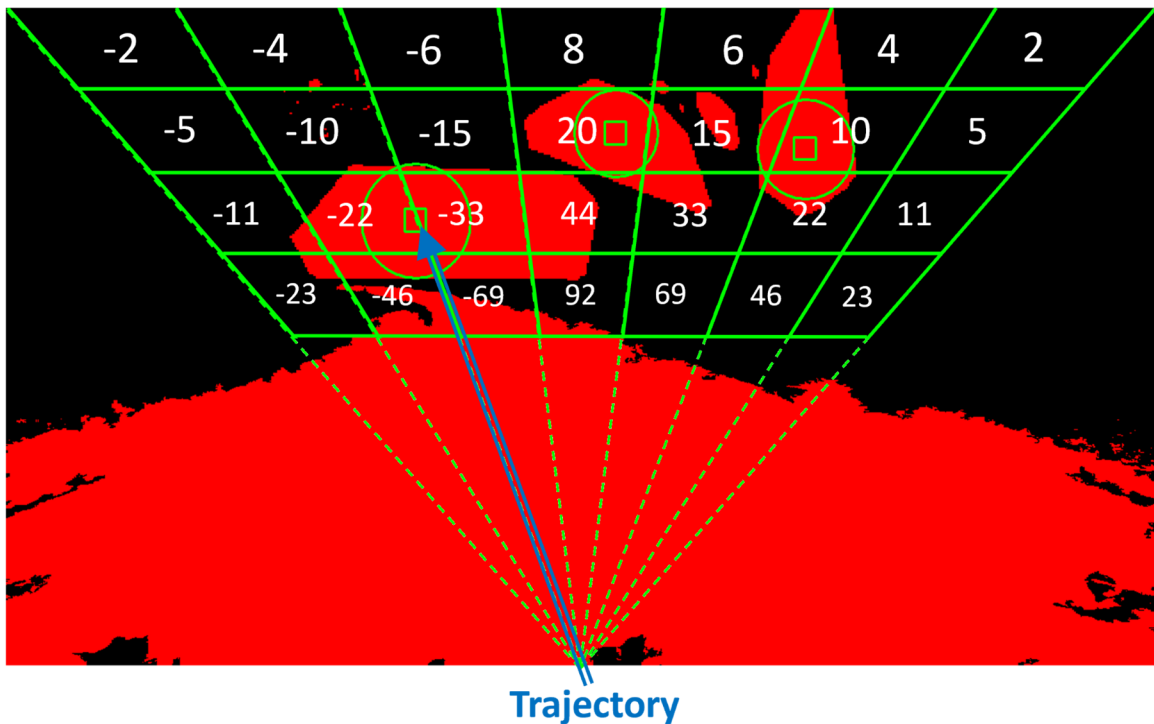


Figure 35: Weight Assignment of Targeted Path Depth Imaging

The weightings were applied to the ROI using a lookup table to minimize computational tasks required to perform analysis on the raw data. Figure 36 was uploaded

into Vision Assistant with a constant lookup table defining the weightings based on the color of the located X or Y pixel coordinate. The color range defined the pixel value for red to be 0 and blue to be 0. The green plane was increased in increments of 9 from 0 to 243, indicating the lookup table from 0 to 27 starting from the bottom to top and left to right. If a geometry of interest was detected outside the green plane lookup table, the off-white color resulted in a 0 weighting for the detected target.



Figure 36: Colorized Lookup Table

#### 4.2.2 Color Vision Mobility

When no geometries of interest were detected, the mobility program defaulted to path detection, searching for the path centroid and turning based on the area centroid. This implementation of path detection is not extensive but effective with the correction color threshold applied to the image. The program would similarly define a scaled steering trajectory based on the calculated location from the processed path detection.

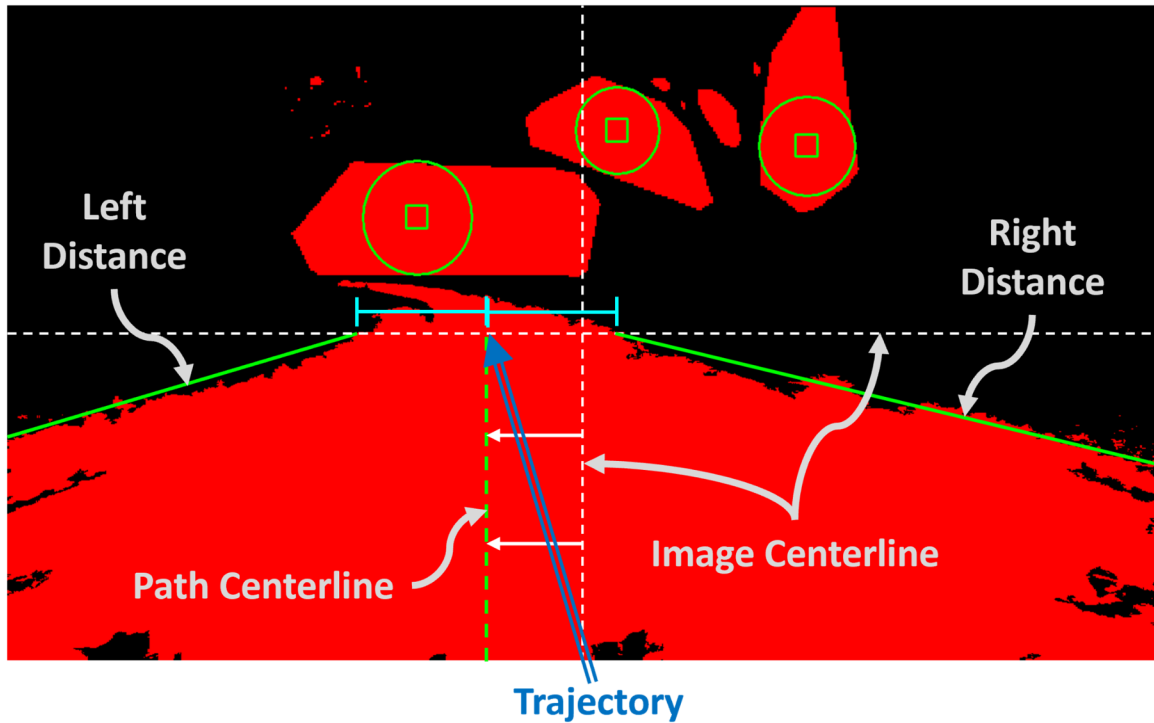


Figure 37: Centroid-based Trajectory for Path Detection Methods

#### 4.2.3 Operational Mobility

Non-vision-related mobility included the adaptive throttle and braking program, essentially cruise control. The UNC Charlotte Fitness Trail is a winding trail with sections of 10% grade or more. Since it was found that the Vevor electric motor did not have regenerative braking capabilities like other, more expensive conversion kits, the vehicle increased speed without throttle when directed downhill. The cruise control model maintained a calculated speed range for the actual encoder velocity given a specified throttle input to prevent any danger to the equipment or passersby. This approach was implemented by feathering the brakes in downhill sections as the actual speed exceeds the threshold and increasing throttle requirements to maintain speed uphill.

### 4.3 GPS Localization

GPS was used to track the eATV location during testing and provide guidance for path selection. The eATV vision scripts do not process any trajectory circles or path detection scenarios at an intersection. The route is defined to only have T-intersections, so the vehicle stops and pings the next waypoint if neither vision processing algorithm produces a valid result. Calculated from the current vehicle heading, current GPS coordinates, and the subsequent waypoint coordinates, the eATV can determine a general direction of the next waypoint and turn either left or right accordingly. It was defined that in a use-case scenario, a user would be knowledgeable of the eATV capabilities and would mark the waypoints as necessary.



Figure 38: Predetermined Waypoint Route

### 4.4 Testing

Testing is necessary to validate the advancements in converting the vehicle to an electric vehicle. Data exploiting acceleration curves to known velocities in flat, uphill,

and downhill scenarios proved the more reliable, consistent, and predictable method of propulsion. The vision testing on both color vision and depth vision methodologies was performed in real-time with the eATV in motion. Due to this, integration testing was partially complete. Further integration testing occurred when implementing obstacle avoidance and intersection detection and maneuvering.

#### 4.4.1 Comparative Testing

Analogous testing was performed to compare the ICE versus the electric conversion at the UNC Charlotte Recreational Field 12 and Charlotte Research Institute (CRI) parking deck. Initially, with the ICE, the vehicle was tested on a large stretch of an open field where no risk was involved for the users and away from pedestrians. The vehicle was tested at varying throttle duty cycles three times each for a 200 ft distance. A low-throttle test (LTT) was conducted at 60% throttle duty cycle, a medium-throttle test (MTT) was conducted at 85% throttle duty cycle, and a high-throttle test (HTT) was conducted at 100% throttle duty cycle or full throttle. To illustrate, Figure 39 represents the three runs of low, medium, and high-speed testing methods. The data captured throughout each test run was recorded for comparison against the eATV. The vehicle was then taken to the CRI deck with a 7% grade slope to perform the same percentage tests three times each uphill for a 100 ft stretch and to record data as the vehicle coasted downhill for the 100 ft stretch. It is necessary to record the uphill and downhill data as there were frequent hills at the final testing location.

Following the first test session, it was determined that the ICE engine becoming heat soaked throughout the test run would not provide an accurate representation of the nature of the vehicle at each independent throttle percentage. Likewise, the tests were

repeated, allowing the ICE to cool down between runs for the flat ground, uphill, and downhill applications. It was also determined that 200 ft was not enough run time for the vehicle to achieve a steady state between the GPS velocity and encoder velocity; therefore, the distance traveled for each test was increased to 250 ft.

After the EV Conversion was completed, testing began in the same manner; the LTT, MTT, and HTT three times each. However, the eATV could be run back-to-back without heat-soaking issues or artificially skewing the data representation.

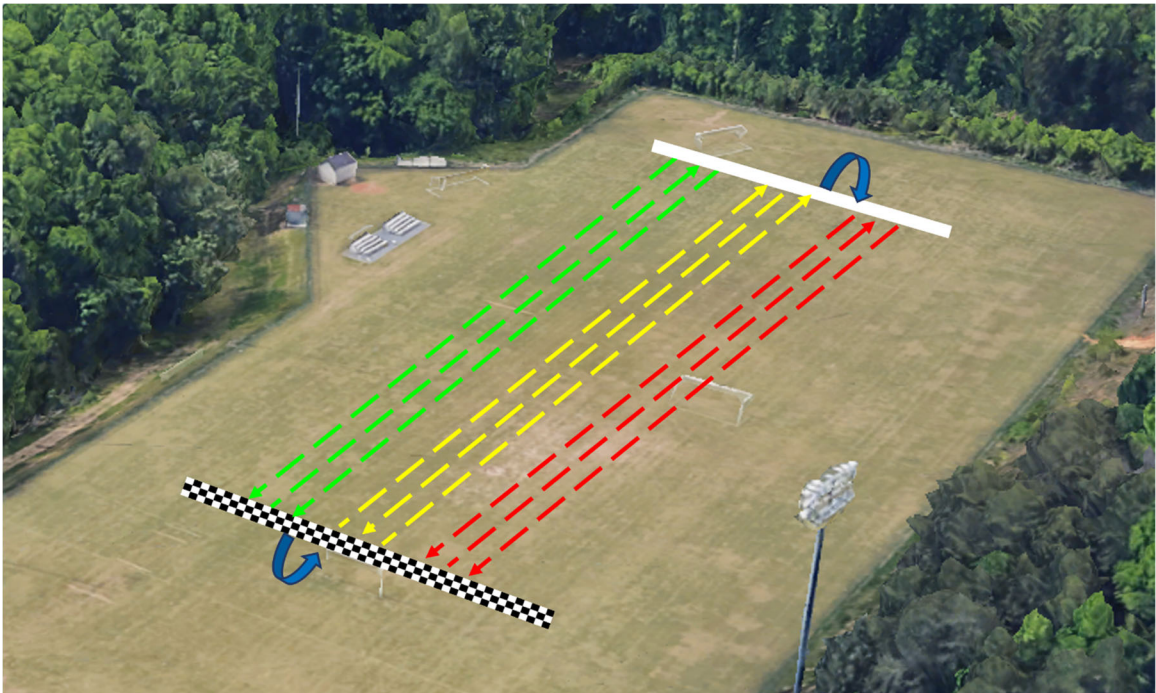


Figure 39: Orientation for Flat Ground Velocity Tests

#### 4.4.2 Color Vision Testing

Testing the color vision implementation included several thousand images of the UNC Charlotte Fitness Trail. Images interpreting the color image for path detection across both asphalt and gravel topographies were conducted to determine a confidence score for each. An image processing algorithm was developed to record and compare the

output score of each path detection script. The algorithm acquires the highest scoring script from each iteration and provides the data associated with the best script available for downstream processing.

#### 4.4.3 Depth Vision Testing

Several thousand images of the Fitness Trail were analyzed to obtain a statistically valid success rate. The LabVIEW algorithms were run through Vision Assistant and analyzed for the successful detection of areas of interest. Obstacle detection was tested by capturing several hundred images of the selected obstacles and measuring the likelihood of detection in the specified ROI.

#### 4.4.4 Operational Testing

Operational testing comprised the entire autonomous system test and integration of the developed features. Independent tests were conducted on the real-time estimated path trajectory, steering response, adaptive cruise control, intersection and obstacle detection, and waypoint tracking. Following the independent testing, an entire system test covered the completion of a 500+ m run and recorded the number of waypoints achieved, instances one or more wheels left the trail, intersections detected, obstacles detected, pedestrians detected, obstacles maneuvered, and average speed.

## CHAPTER 5: RESULTS AND DISCUSSION

Testing provided substantial sample data to validate the electric conversion, GPS localization, implemented vision processing techniques, and autonomous navigation. Comparisons of the ICE versus EV conversion were conducted on flat, inclined, and declined ground levels. Computer vision scripts were implemented and analyzed for success rate following on-site testing. GPS localization was confirmed and validated against a referee device along the UNC Charlotte Fitness Trail. Autonomous navigation and system integration were tested along the trail to successfully traverse 500+ meters and evaluate the eATV research.

### 5.1 Comparative Testing

A comparison between the two vehicle configurations was necessary to evaluate the improvements following the EV conversion from the original ICE platform. The same tests were performed in each configuration to effectively compare, recording the necessary data to capture overall acceleration and speed stability.

#### 5.1.1 ICE Warm Start

The original ICE powertrain was tested before the eATV conversion. The LTT, MTT, and HTT sessions were conducted along a 200 ft distance. Each test session included three runs of each throttle duty cycle back-to-back from high speed to low speed. The ambient temperature at the time of testing was 83 degrees Fahrenheit. During the flat ground test, it was noted that the average velocity changed for each throttle duty cycle as the testing period progressed.

Figure 40 displays the first three runs of the full-throttle test series. It is noted that the vehicle has a nonlinear acceleration curve and does not reach a steady state. For this research, steady state is defined as a test series reaching and maintaining a maximum speed within 1 MPH.

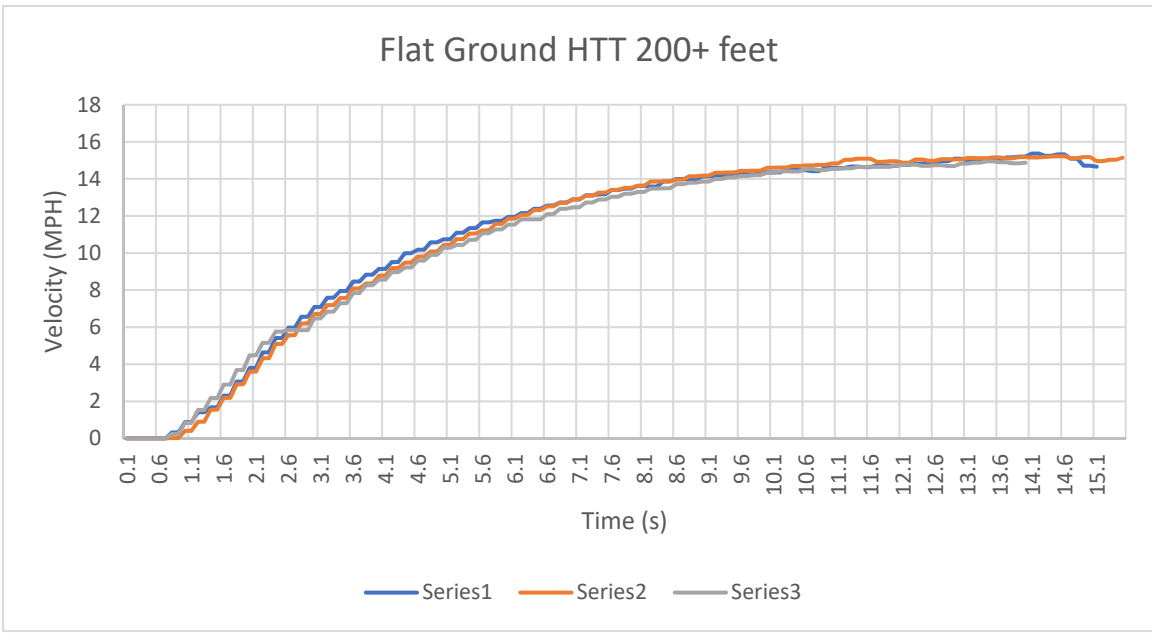


Figure 40: Flat Ground HTT: Warm Start

The test series were overlaid by aligning the first significant value of the collected data, as shown in Figure 41. The variation of the runs is noted to have a significant difference at the beginning of the run. After a few seconds, the variation is minimized as the vehicle nears a steady state and stays around 3% for the remainder of the run.

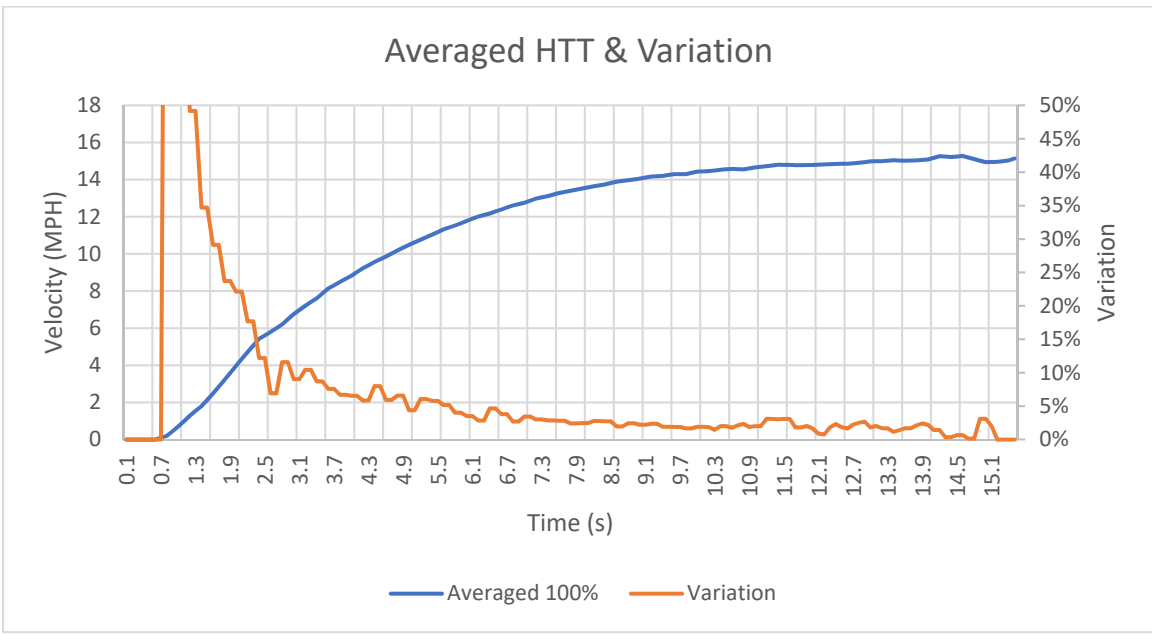


Figure 41: Averaged HTT & Variation: Warm Start

Following the FTT, the MTT was performed for three runs of 200 ft each. This test displayed a decrease in speed between the first and last two runs. Figure 42 displays the data again not reaching a steady state. This is apparent as the data does not reach peak velocity until the end of the run, allowing no consecutive data points for averaging.

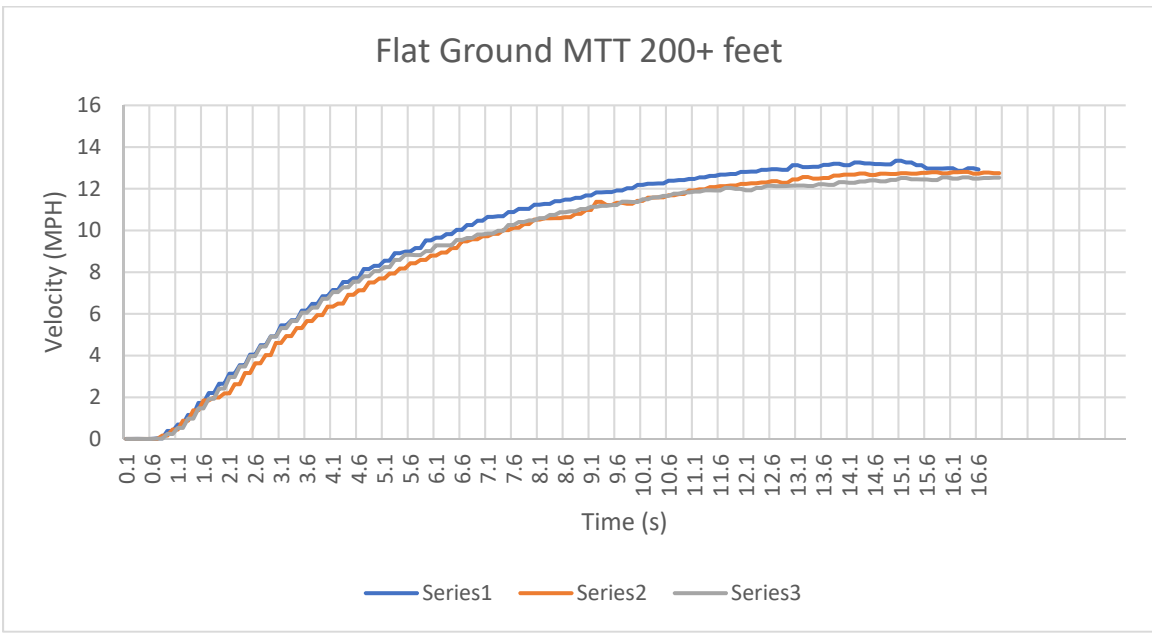


Figure 42: Flat ground MTT: Warm Start

Likewise, Figure 43 displays that the variation between the three MTTs is more significant than that of the previous series, about 7% after three seconds. After six seconds, the variation between the three test series reaches a steady state as the three runs maintain acceleration curves within a tight tolerance of each other.

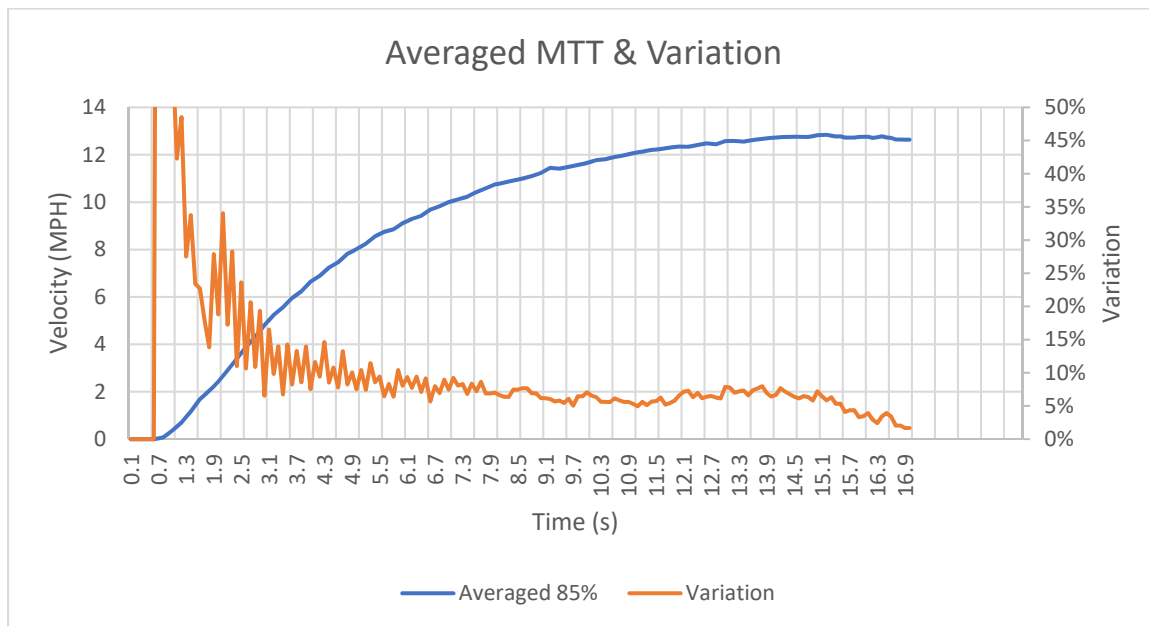


Figure 43: Averaged MTT & Variation: Warm Start

During the LTT, there was a visible decrease in velocity as the vehicle traversed the 200 ft stretch, as seen in Figure 44. The session's third and final test series was nearly 2 MPH slower than the first LTT series attempt, a 20% decrease. At this point, the vehicle experienced a power loss due to the ICE's heat cycling. This was caused by the test sessions being conducted back-to-back. It was also noted that the second and third series began decelerating during the LTT session.

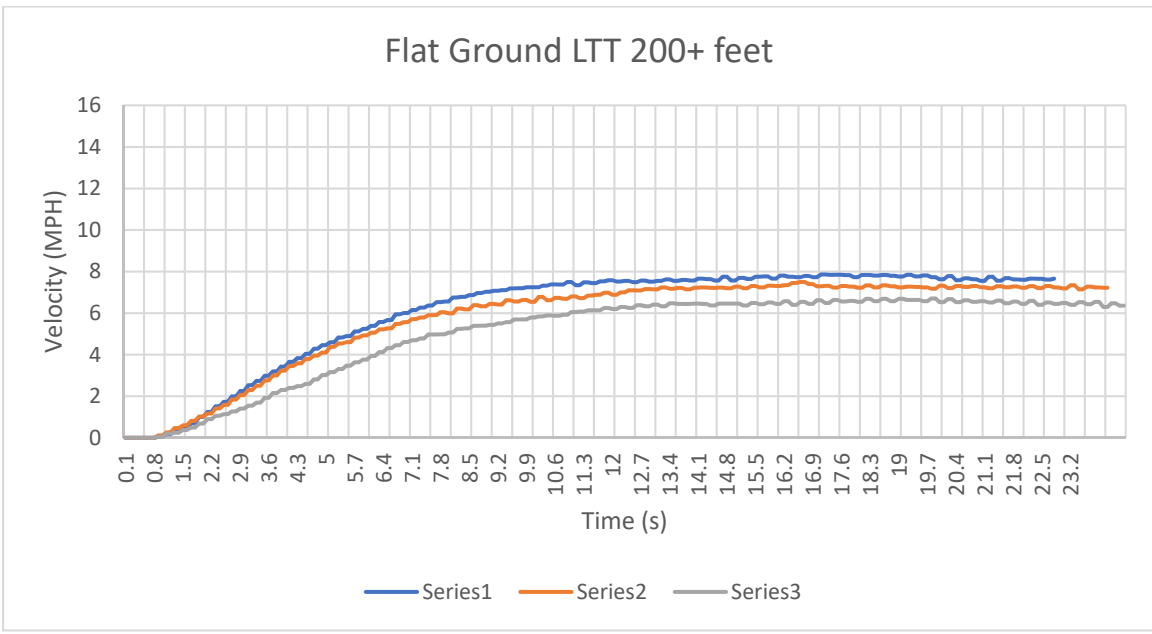


Figure 44: Flat Ground LTT: Warm Start

The variation also displays the increased speed differential, totaling 17% for the steady-state portion after fourteen seconds in Figure 45. The variation is higher, as noted in the previous figure, responding to the heat cycling of the ICE. This differential also caused the variation to reach steady state later in the run compared to the previous tests.

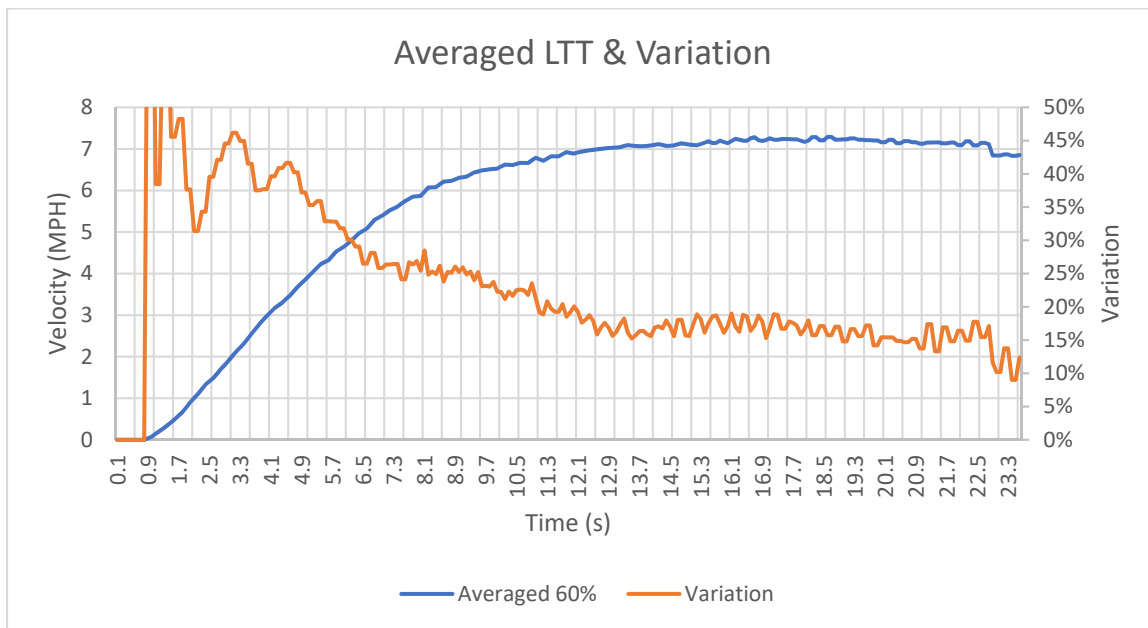


Figure 45: Averaged LTT & Variation: Warm Start

Summarizing the results from the flat ground ICE warm-start test, Figure 46 details an overlay of the three averaged speeds for the LTT, MTT, and HTT to achieve 200+ m. The initial acceleration to reach the maximum speeds for each throttle duty cycle changes between each respective throttle test. If attempted for use in an autonomous control scheme, compensation variation would be necessary to respond to throttle commands accordingly.

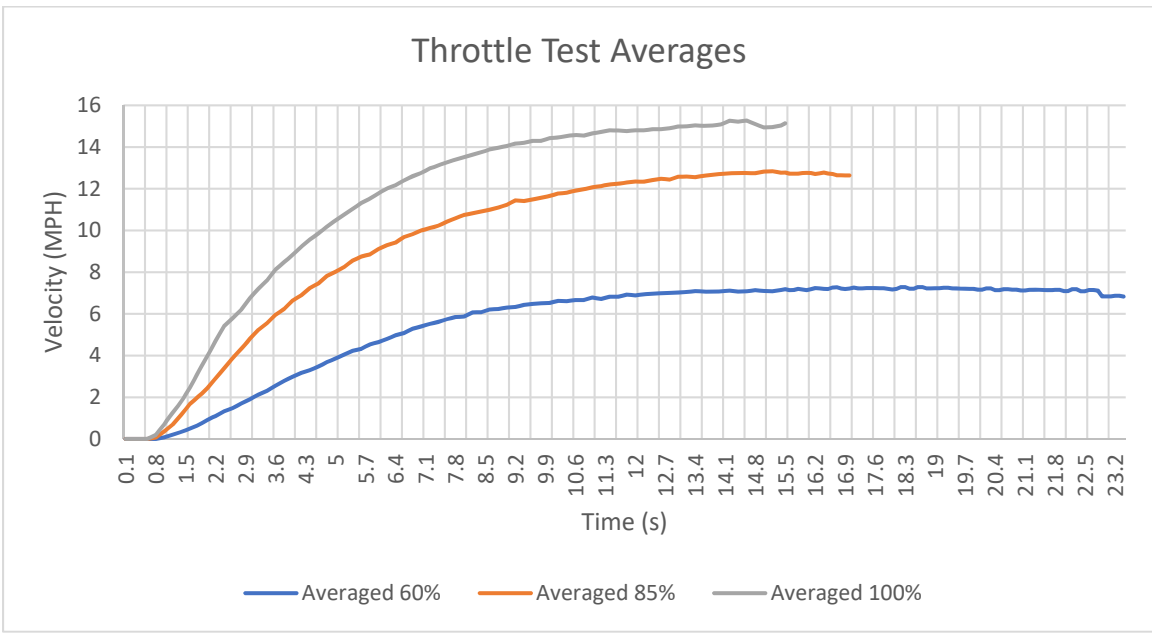


Figure 46: Summarized Throttle Response: Warm Start

The uphill testing was conducted the same day following the relocation of the ICE vehicle from the UNC Charlotte Recreational Field 12 to the CRI deck. Figure 47 represents the uphill test data captured in a 100 ft span. The vehicle did not reach a steady state but did demonstrate a distinct change in acceleration around the 2-second marker.

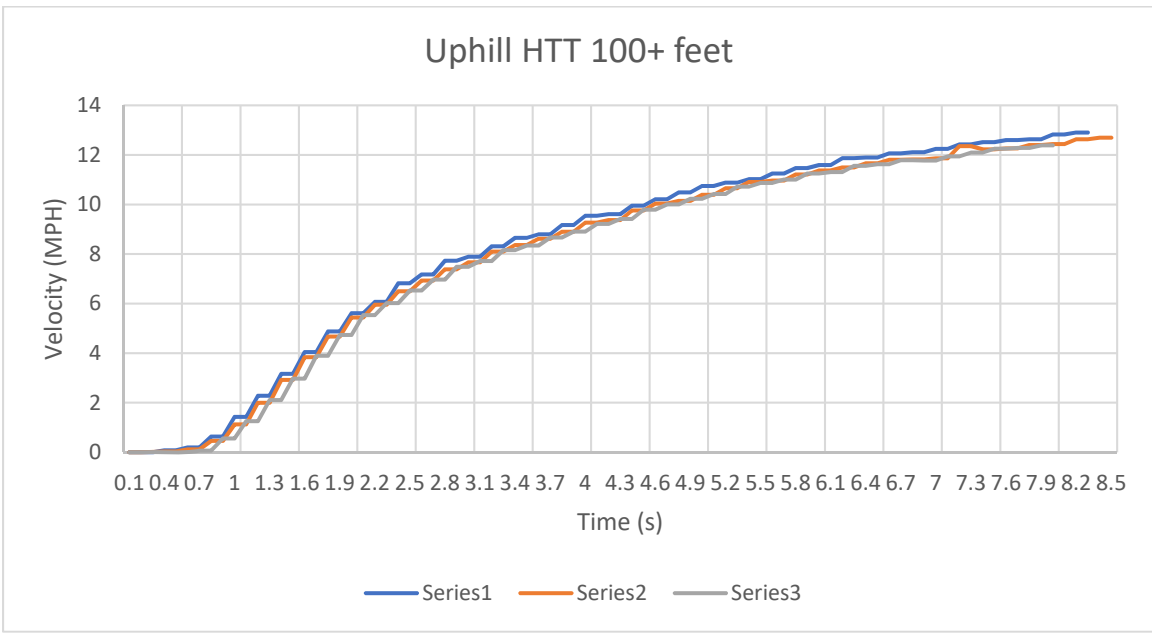


Figure 47: Uphill HTT: Warm Start

Like the flat ground HTT, the variation between the uphill HTT was low, around 4%, as displayed in Figure 48. Various factors may contribute to this, such as cooling aspects of higher velocity travel for an air-cooled ICE, operating conditions for the carburetor at full throttle, and the more rapid initial acceleration to the maximum speed for the HTT.

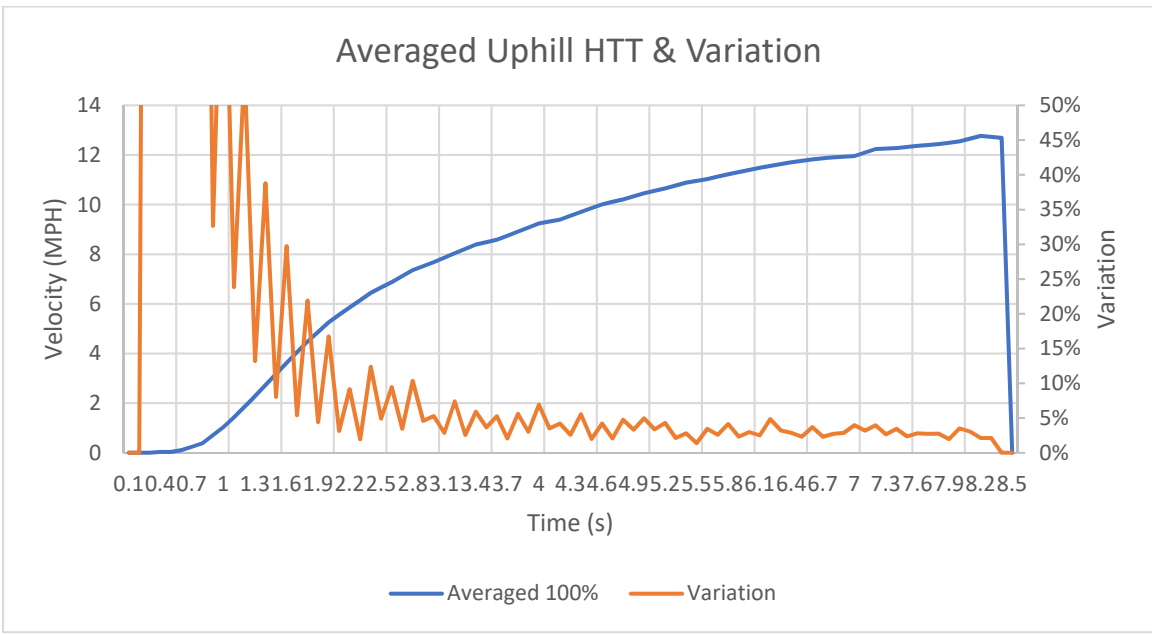


Figure 48: Averaged Uphill HTT & Variation: Warm Start

Figure 49 details the uphill MTT. Similarly, around the 2-second marker, the vehicle changes pace and accelerates less until completing the test series. The MTT does not achieve steady state on the uphill test. This is due to the ICE vehicle accelerating on a more challenging, uphill grade which impacts the rolling friction with the ground and inertia acting on the vehicle in the downhill direction.

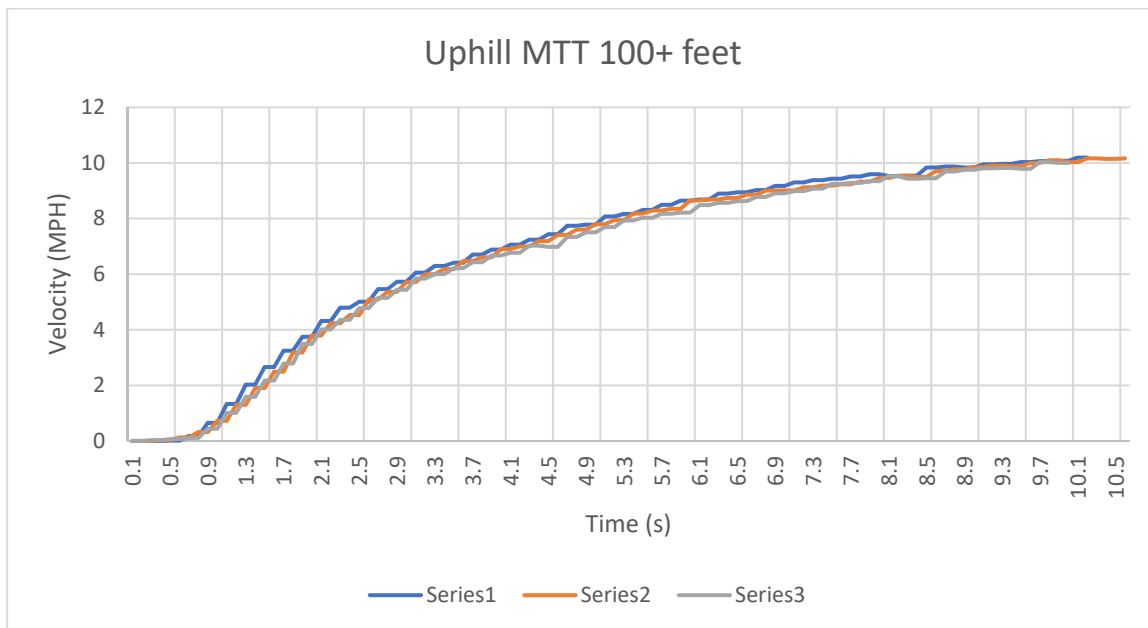


Figure 49: Uphill MTT: Warm Start

Once again, the variation between the three series is low during the middle to the second half of the test in Figure 50. Another attribute of the uphill testing scenario was the concrete topography versus the grassy field of Rec Field 12. This in addition to the shorter testing scenario and more challenging terrain grade may have provided a more repeatable scenario for the ICE-powered vehicle. It is also likely that the loading on the vehicle during the uphill test limited the initial acceleration to respond more like the heat-soaked ICE following the first test series.

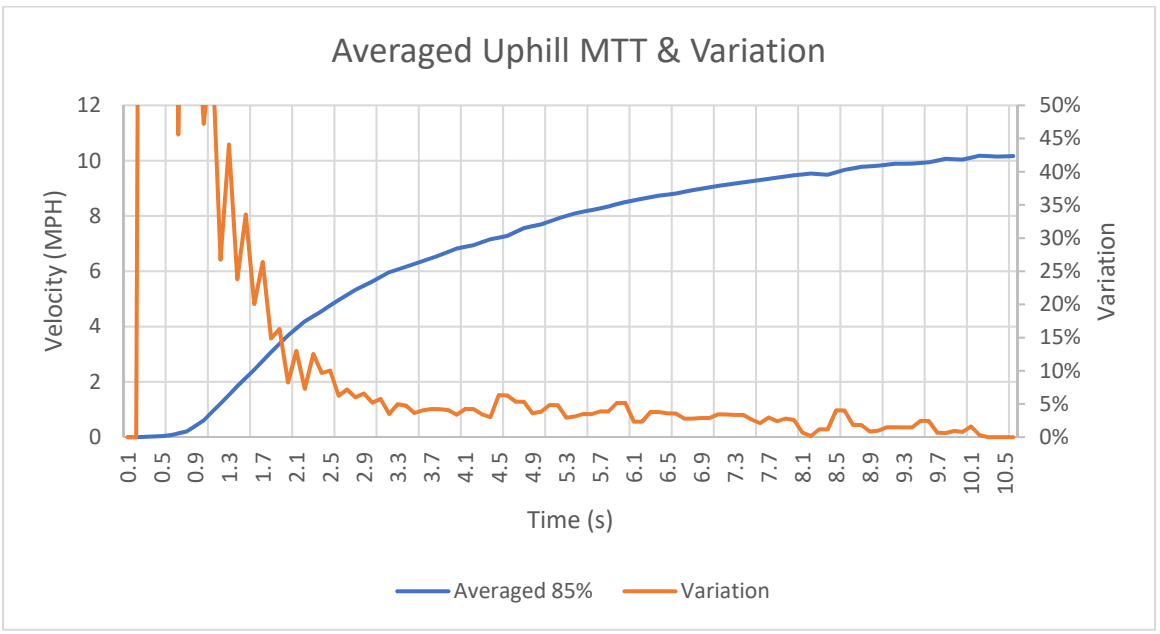


Figure 50: Averaged Uphill MTT & Variation: Warm Start

The LTT of the ICE warm start session concluded with the 60% series. Figure 51 provides the three series, illustrating the same change in acceleration around the 2-second marker. Similar to the flat ground LTT, the vehicle experienced a decrease in acceleration and peak velocity following the first series of the uphill LTT. It is also noted the latter two test series took longer to complete the span as the overall ground speed was slower.

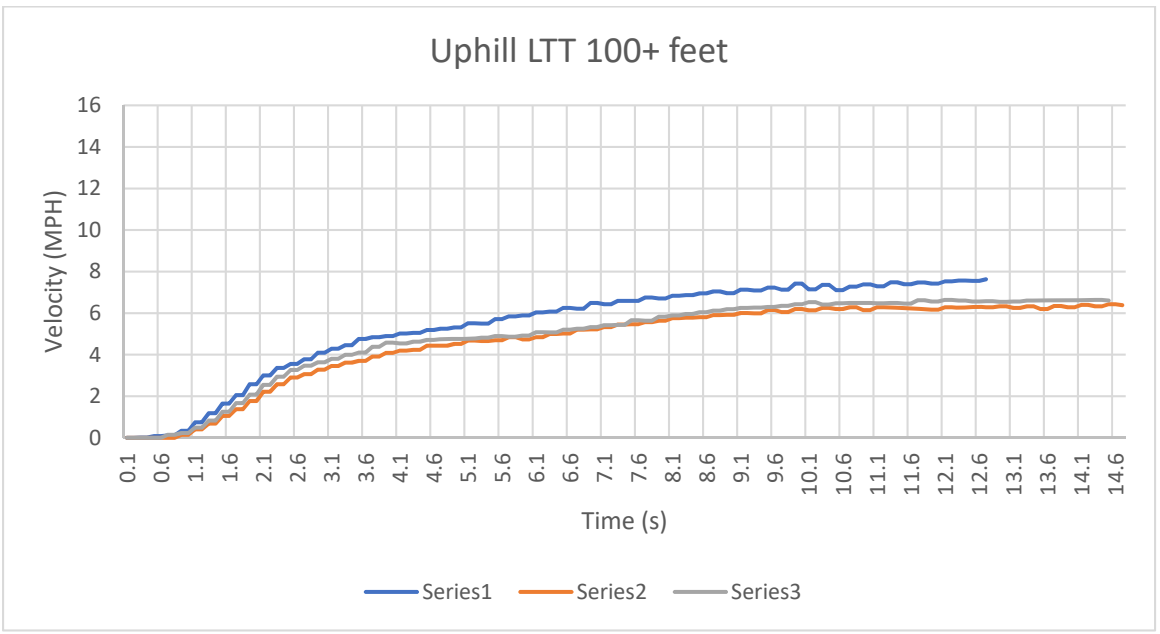


Figure 51: Uphill LTT: Warm Start

The variation between the uphill LTT was on par with that of the flat ground LTT. As shown in Figure 52, the uphill variation averages 19%, excluding the outliers. The outlier shown near the end of the displayed data is due to the first series completing the distance faster than the other two test series. The second and third LTT were more alike, causing the variation to jump down the calculated variation between said series.

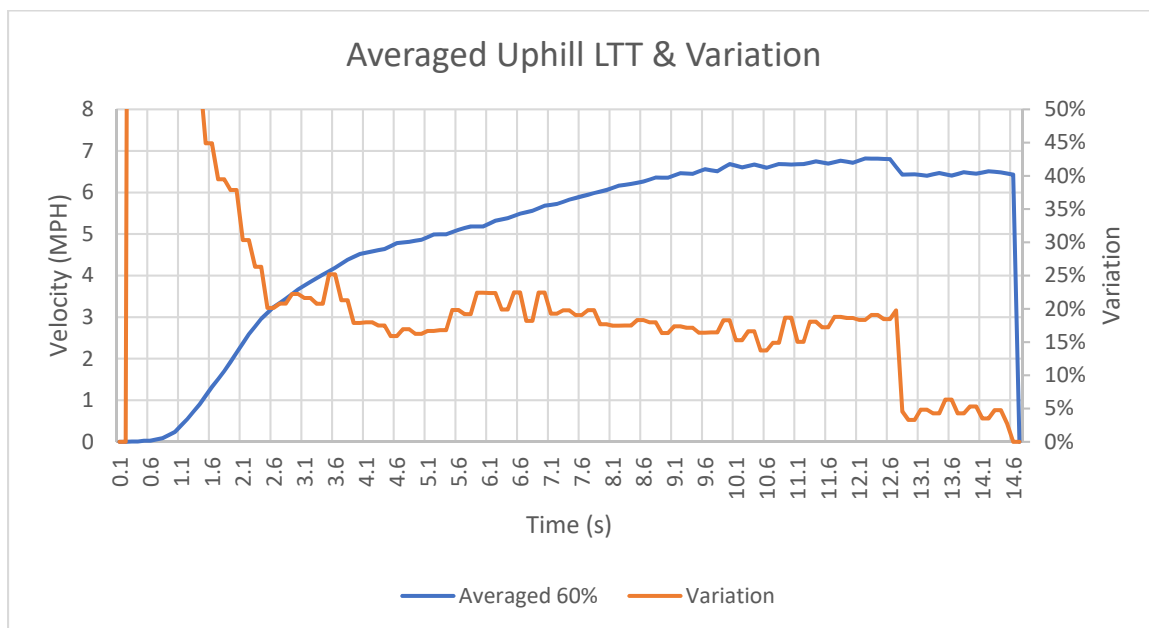


Figure 52: Averaged Uphill LTT & Variation: Warm Start

Three downhill tests were conducted to determine the acceleration and maximum velocity of the ICE-powered vehicle for comparing the downhill aptness. The vehicle was placed at the top of the 100 ft span and the brake was released without providing any throttle. The tests were conducted following the end of each uphill throttle duty cycle session. In Figure 53, the first downhill series increased linearly; however, the following two tests accelerated more rapidly and reached a higher speed each time. This is likely due to the ICE becoming heat-soaked and thus reducing resistance within the vehicle transmission and/or torque converter. The transmission and torque converter inherently apply an amount of torque to engine-brake or slow as the throttle is not commanded. The initial engine-braking torque was greater during the first downhill test series, forcing the vehicle to accelerate linearly down the hill to a steady state. The following two test series did not respond linearly to the downhill test.

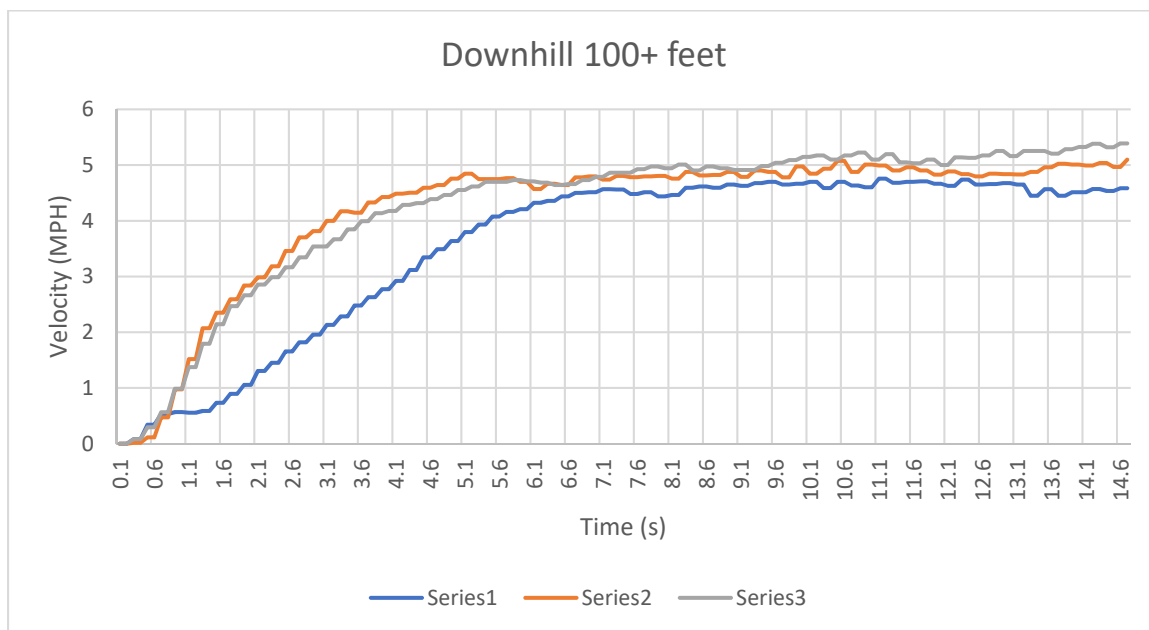


Figure 53: No Throttle Downhill Test: Warm Start

In the case of Figure 54, the more prominent variation between 0 and 2 seconds was apparent, though it decreased to a 4% average during the middle of the run. The ICE-powered vehicle reached and maintained a steady state for the first and second downhill test series. However, the third test series began accelerating again at the twelve second marker. This may be caused by the vehicle surpassing a temperature threshold which allowed the downhill acceleration to stop at a maximum speed. Once the ICE-powered vehicle was heat-soaked, the downhill acceleration would continue passed the initial data points from the first and second series.

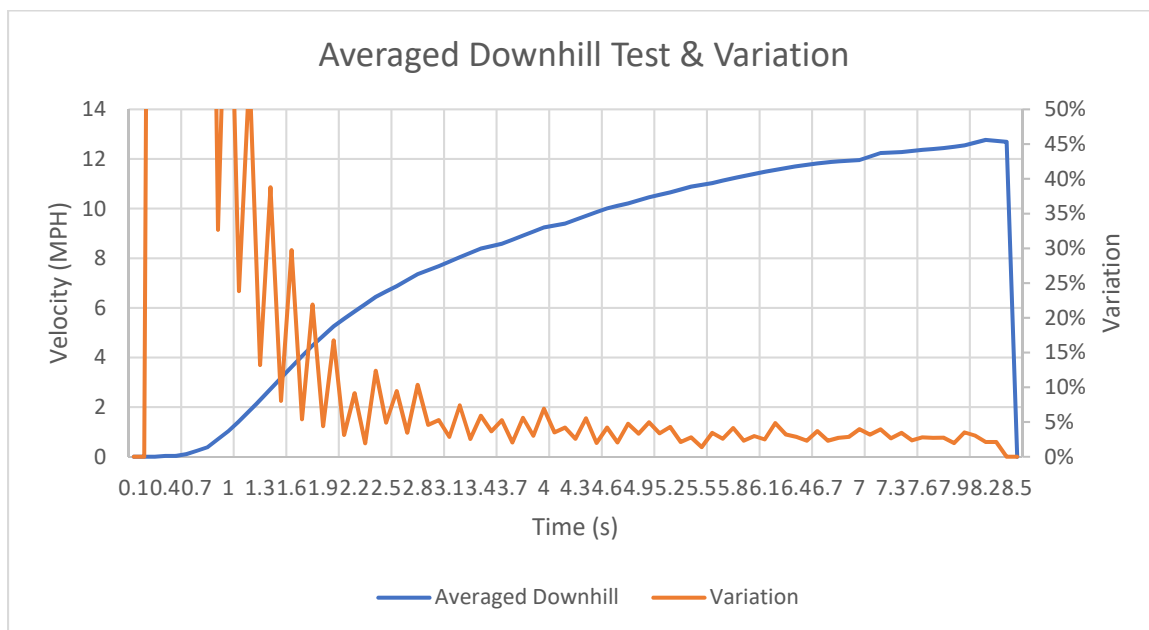


Figure 54: No Throttle Downhill Variation: Warm Start

### 5.1.2 ICE Cold Start

After analyzing the warm start test data, it was questioned whether the back-to-back vehicle operation played a role in the odd variation at lower speeds. To avoid artifacts found during the warm-start testing, the exact tests were conducted again with a rest period between each throttle duty cycle test. This waiting period allowed the ICE vehicle to cool to the same starting temperature of +/- 3 degrees Fahrenheit.

The ambient temperature on the test day was recorded to be 82°F. The vehicle was started to maneuver into position and then allowed time to cool down to a goal of 100°F. Table 2 captures the measured engine temperatures at the start of the test series and following the completion of each test run. As it was determined that 200 ft was not enough room to reach steady states, repeated testing was extended to the 250 ft marker to ensure a steady state was achievable. Note that the individual throttle duty cycle tests were conducted back-to-back to see the temperature and speed change as the ICE warms.

Table 2: HTT Conditions at 82°F Ambient

Condition	Engine Temp. (°F)
Start	99
Run 1	120
Run 2	156
Run 3	168

Figure 55 compares the first three runs of the cold start HTT on flat ground. The test run experienced a more significant difference in speed at a steady state. During this test session, the first test series was slower than the second and third test series; directly opposite of that experienced during the warm start. It was hypothesized that the ICE-powered vehicle performed more consistently within a range of engine temperature rather than simply lower temperature.

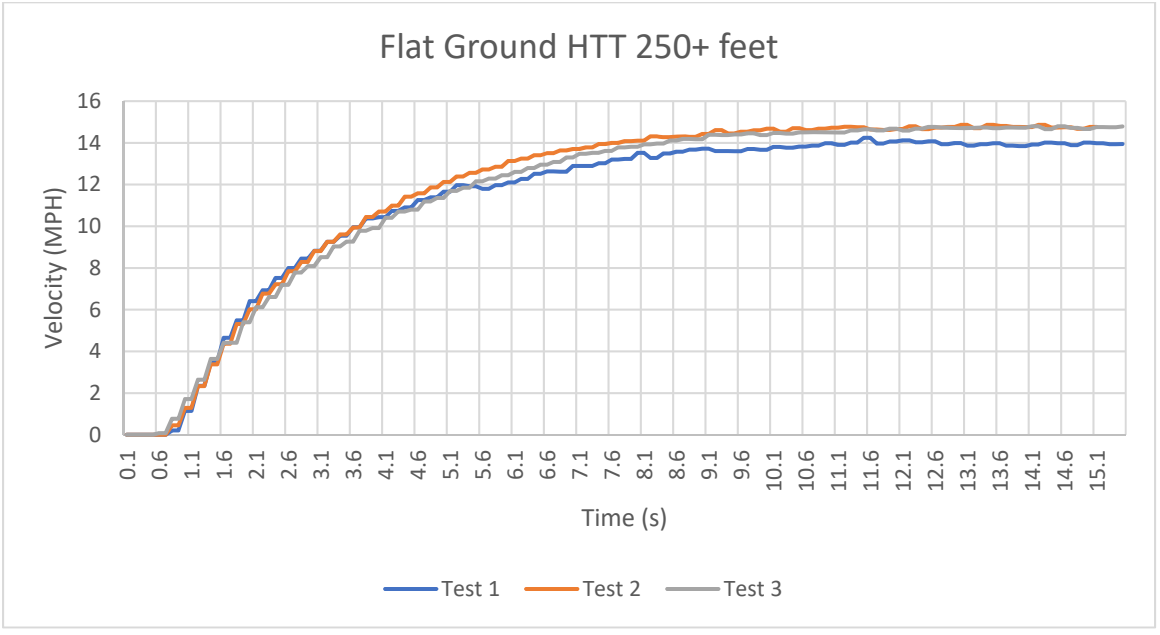


Figure 55: Flat Ground HTT: Cold Start

Likewise, Figure 56 captures a more considerable variation of 6% throughout the test run than the original 100% throttle duty cycle test run. The vehicle does, however, reach a steady state with the newly extended distance in the new testing scenario. The additional 50 ft provided ample room for the vehicle to reach and maintain the ground speed within 1 MPH for each test series of the HTT.

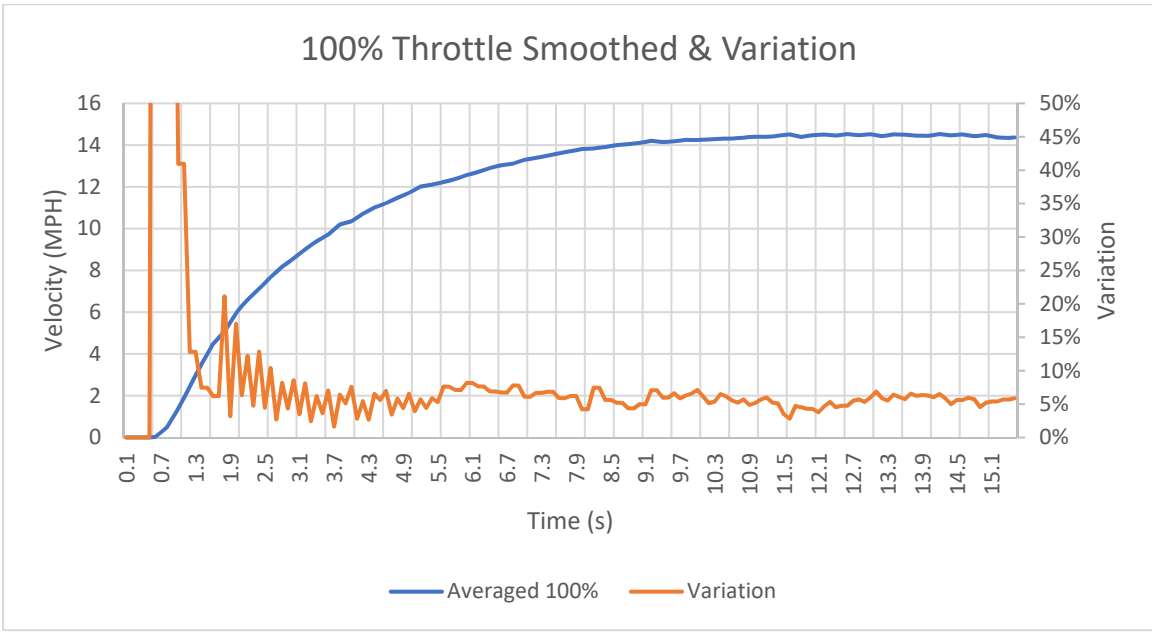


Figure 56: Averaged HTT & Variation: Cold Start

Conducting the MTT started using the same methodology as the previous HTT session. Table 3 details the starting and intermittent temperatures during the MTT. Notably, the ICE-powered vehicle did not exceed the temperature of the previous test session. This is due to the lower throttle requirements, reducing the power output from the ICE to reach the respective maximum speed.

Table 3: MTT Conditions at 82°F Ambient

Condition	Engine Temp. (°F)
Start	104
Run 1	123
Run 2	142
Run 3	161

Figure 57 captures 3 test runs from the ICE vehicle with a cold start during the MTT. An end speed difference of 1.5 MPH was common during earlier testing but recording three opposing acceleration curves from the same test scenario was not. The first and third test series have a similar initial acceleration; however, the first and second test series have a similar steady-state velocity.

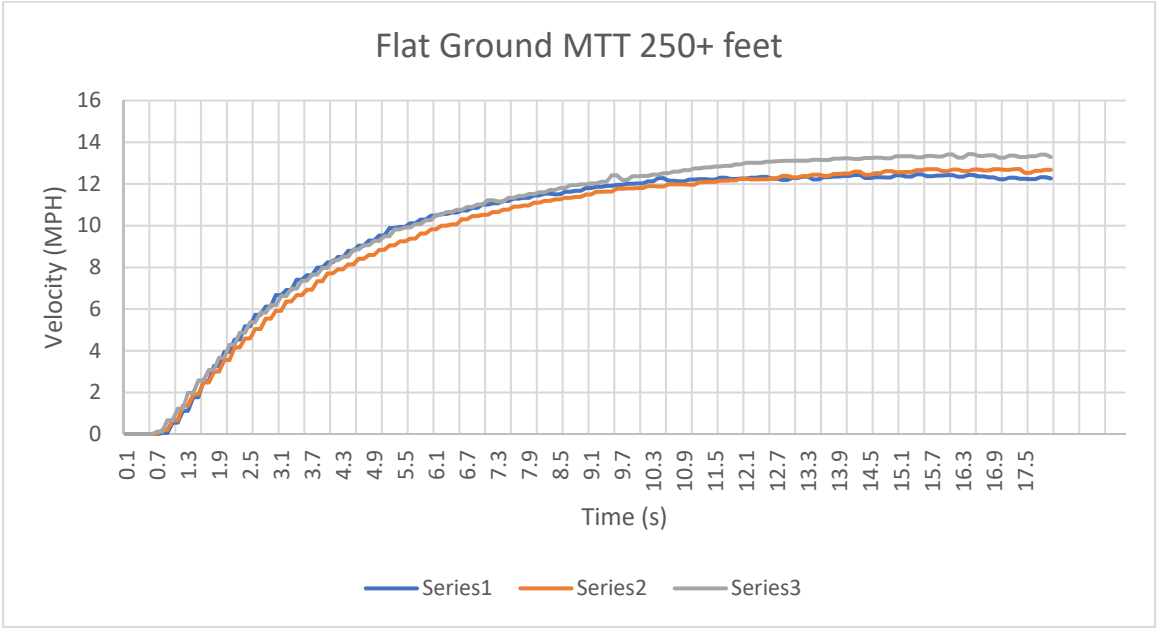


Figure 57: Flat Ground MTT: Cold Start

The variation of the three test series from the MTT hovered around 7%, as seen in Figure 58. The averaged MTT data displays a steeper acceleration curve, thus allowing the vehicle to reach a steady state in the final quarter of the test. As noted in the Figure 57 discussion, the acceleration curves do not exactly align in this MTT session. Likewise, the variation for the averaged MTT dips during the middle of the run where the vehicle velocities are nearest and begins to rise with the third test series.

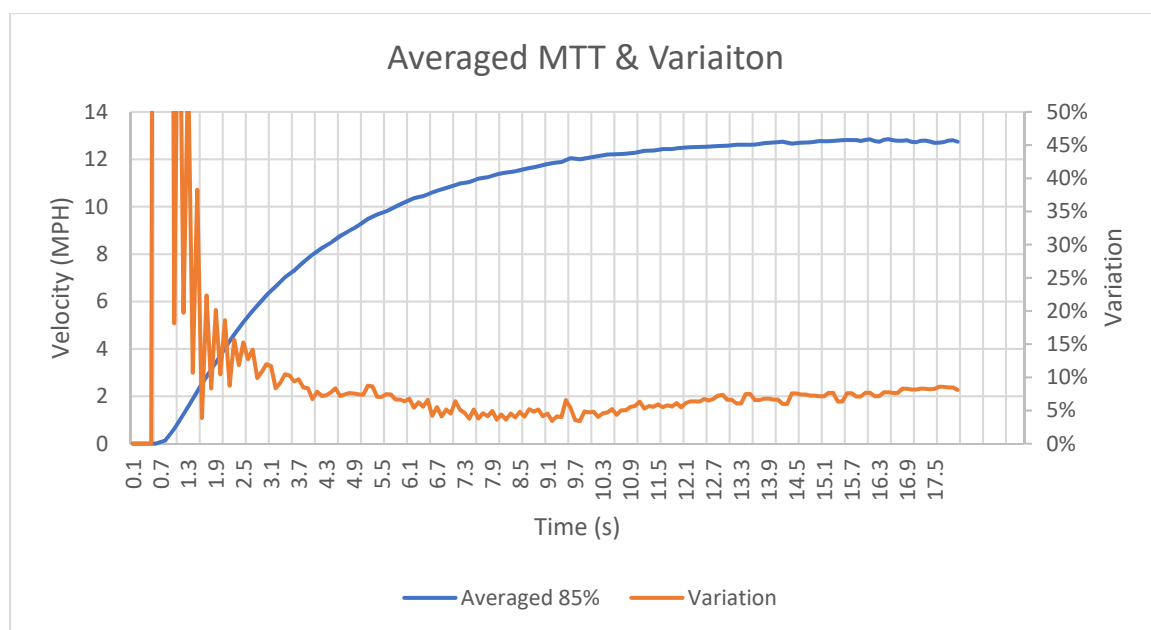


Figure 58: Averaged MTT & Variation: Cold Start

The last flat ground test session concluded with the three LTTs. Table 4 delivers the starting and intermediate temperatures for the three test series. It is noted that the final ICE temperature following the third test of each session does not drop linearly: HTT of 168°F, MTT of 161°F, and LTT of 159°F. This is due to the lower ground speeds limiting the available airflow to the ICE. The relationship between vehicle speed and engine temperature varies due to several variables as discussed.

Table 4: LTT Conditions at 82°F Ambient

Condition	Engine Temp. (°F)
Start	101
Run 1	116
Run 2	145
Run 3	159

Figure 59 represents the three recorded LTTs. Compared to the flat ground LTT with a potentially heat-soaked ICE, the vehicle performed more smoothly when allowed to cool down prior to testing. This procedure could be used in autonomous vehicle operation but would require stopping the vehicle every few hundred feet and waiting ten minutes or more to allow a cool-down period without a form of adaptive throttle control or machine learning.

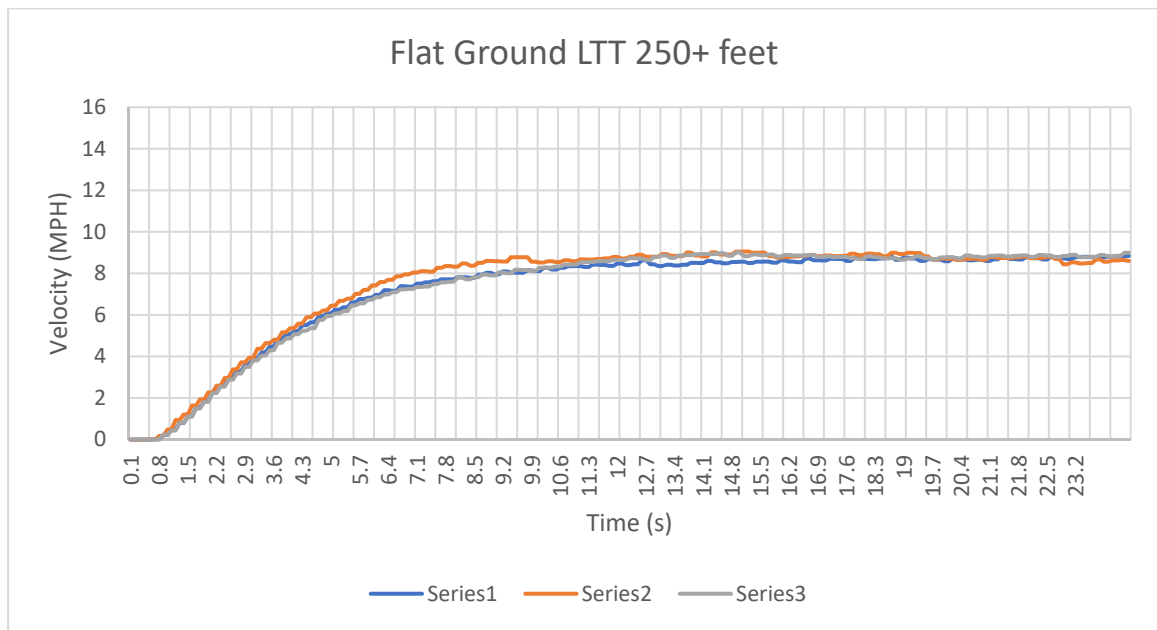


Figure 59: Flat Ground LTT: Cold Start

Figure 60 displays the variation throughout the run. It is possible that the vehicle hit a bump or an unlevel portion during the flat ground test to generate a rapid decrease in velocity. Despite the anomaly, the ICE-powered vehicle reached a steady state after ten seconds of the LTT with a 5% variation between the three test series.

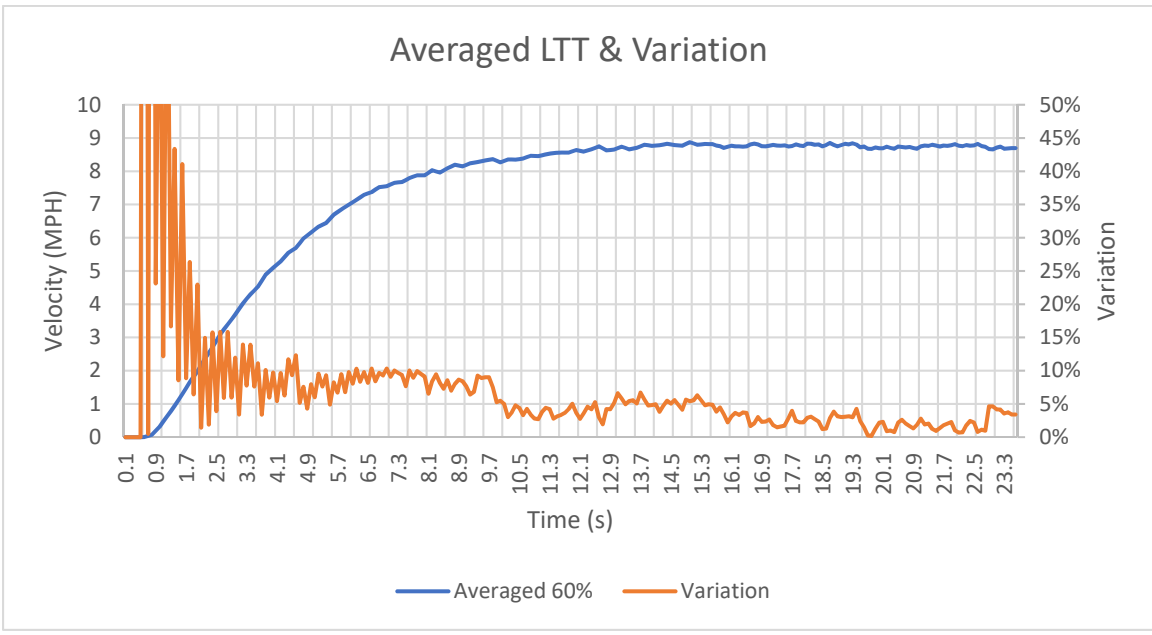


Figure 60: Averaged LTT & Variation: Cold Start

To summarize the flat ground cold start testing LTT, MTT, and HTT, Figure 61 provides an updated overlay of the three averaged runs to achieve a span of 250+ ft. The results were more promising, providing ample room for the ICE vehicle to achieve a steady state.

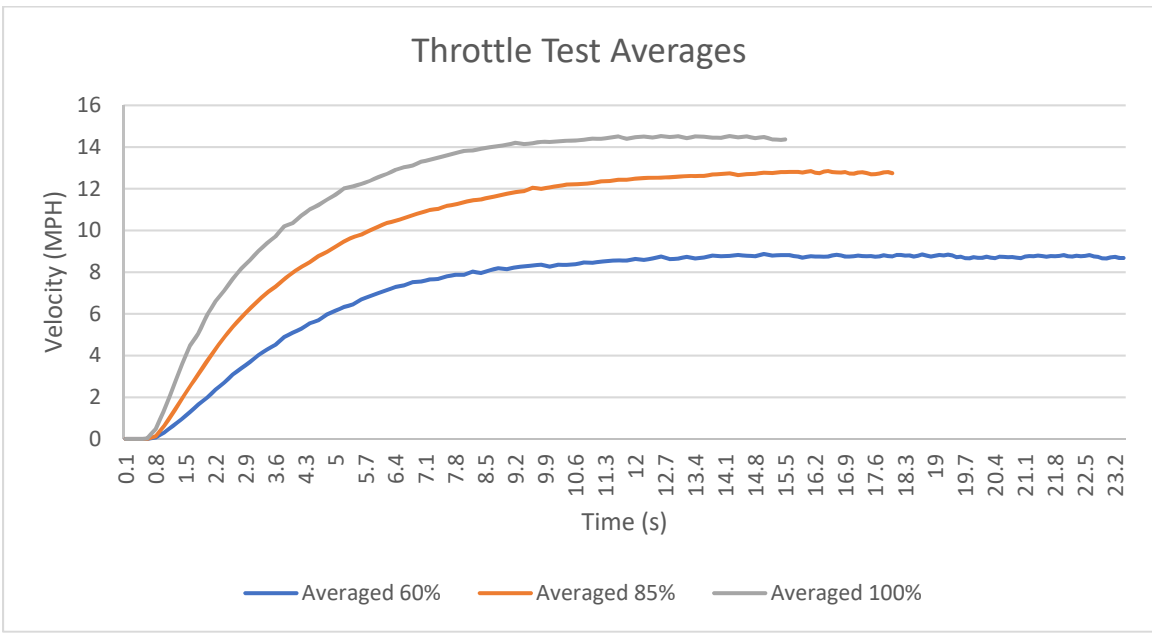


Figure 61: Summarized Throttle Response: Cold Start

Having recognized the change in response to cold starts versus warm starts on flat ground, it was also decided to redo the uphill tests. The respective starting and intermittent temperatures were recorded in Table 5, though the start temperature was increased to 120°F as the first run of each prior session in the flat ground testing appeared slightly lower than the average acceleration curve.

Table 5: Uphill HTT Conditions at 83°F Ambient

Condition	Engine Temp. (°F)
Start	123
Run 1	141
Run 2	169
Run 3	183

Figure 62 details the first series of uphill HTT. It is noted that there is a more considerable variation in the initial acceleration discrepancy between runs. All three were conducted as a full-throttle start, though the second series lagged much further behind. There is a greater difference between the initial acceleration curves of the three test series but they do reach the same maximum velocity at the end of the test session.

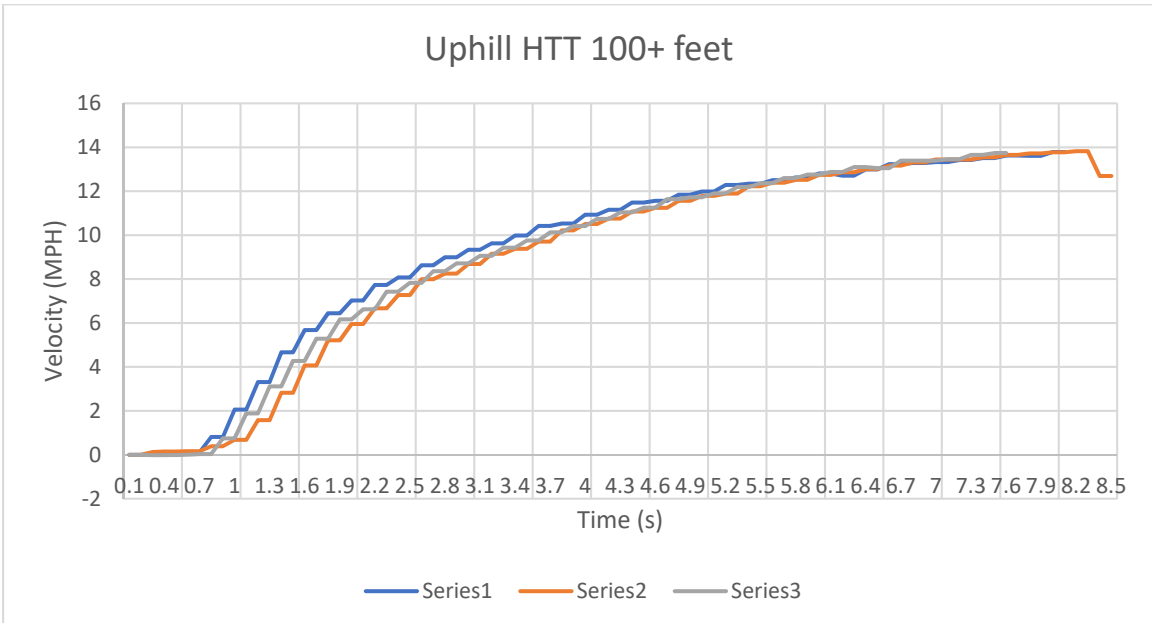


Figure 62: Uphill HTT: Cold Start

Figure 63 captures the variation between the three runs, indicating the significant difference at the beginning of the test. Unlike other tests conducted thus far, the variation between the three test series neared 0% by the end of the recorded data. As mentioned previously, the uphill HTT applies a more substantial loading on the vehicle.

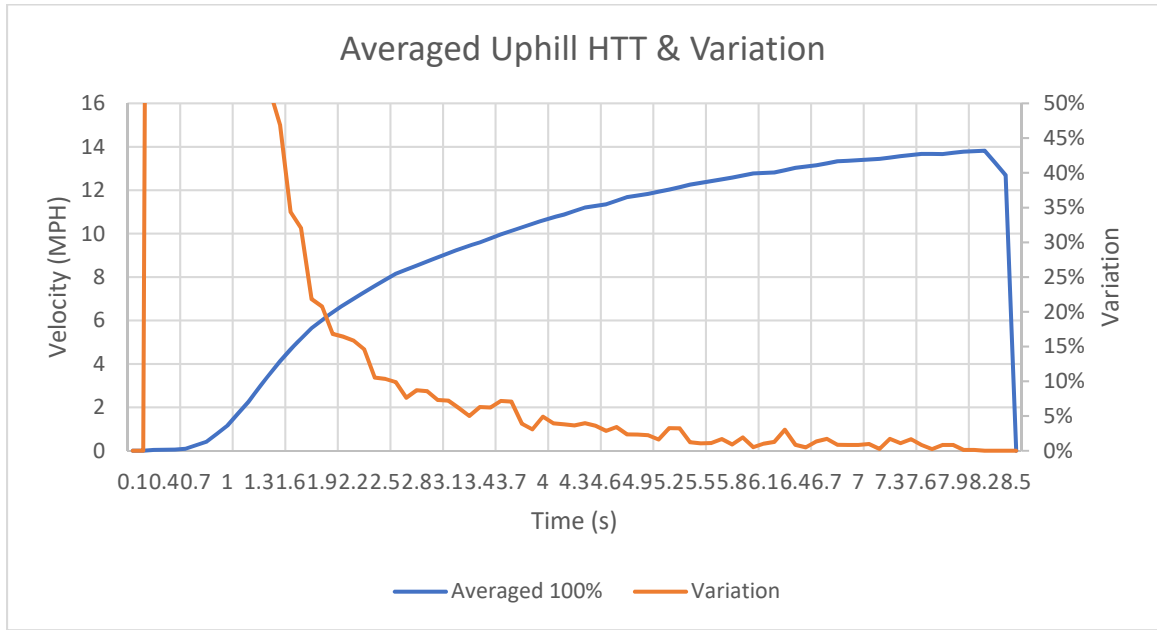


Figure 63: Averaged Uphill HTT & Variation: Cold Start

The ICE temperature was also recorded at the start of the test session and intermittently between each series. Table 6 details a higher end temperature compared to the HTT.

Table 6: Uphill MTT Conditions at 83°F Ambient

Condition	Engine Temp. (°F)
Start	119
Run 1	135
Run 2	154
Run 3	170

Figure 64 displays the three runs to record the uphill MTT. Similar to the prior uphill test session, there was a change in acceleration at the 2-second marker. The ICE-

powered vehicle is still incapable of reaching a steady state during the uphill MTT test session.

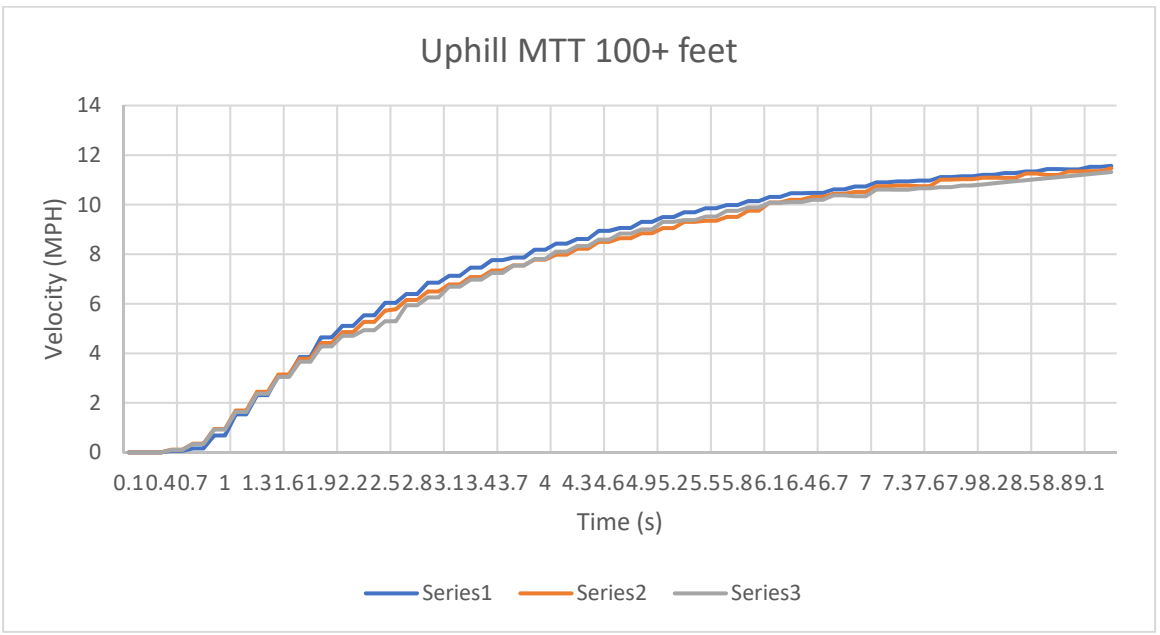


Figure 64: Uphill MTT: Cold Start

At the 2-second marker, the variation spike momentarily before returning to 4% on average during the second half of the test of Figure 65.

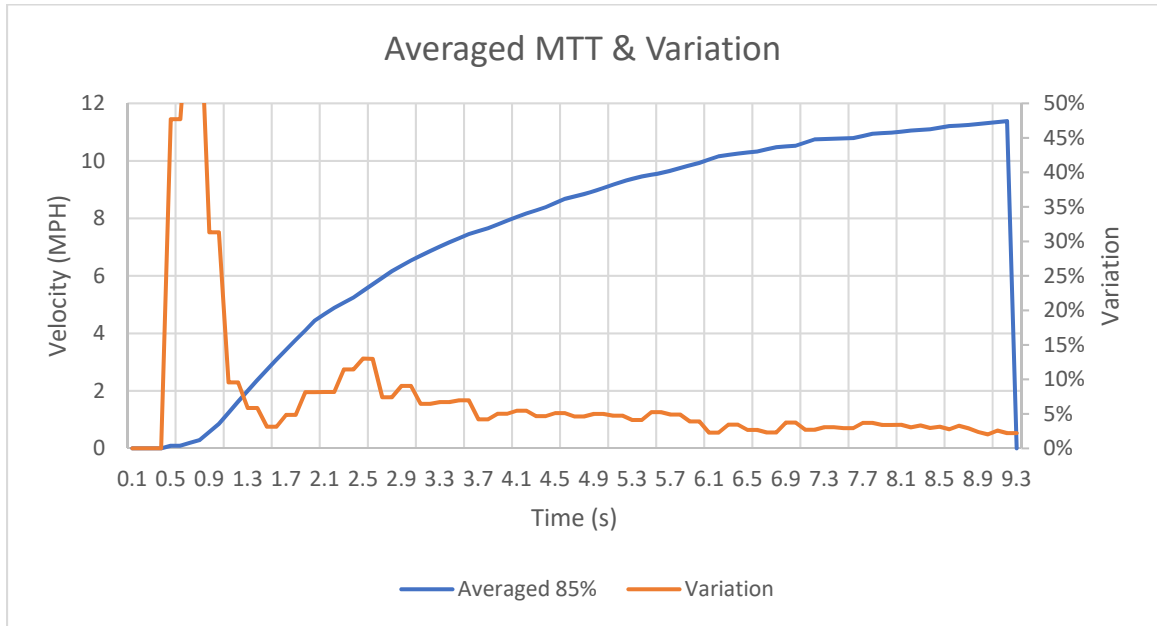


Figure 65: Averaged Uphill MTT & Variation: Cold Start

The uphill LTT intermittent temperatures were recorded as detailed in Table 7.

Table 7: Uphill MTT Conditions at 83°F Ambient

Condition	Engine Temp. (°F)
Start	121
Run 1	138
Run 2	155
Run 3	174

Figure 66 displays the uphill LTT, which also experienced a change in acceleration at the 2-second marker. The first run maintained a higher speed traversing the 100 ft uphill. The second and third test series were again slower than the first test series during the uphill LTT.

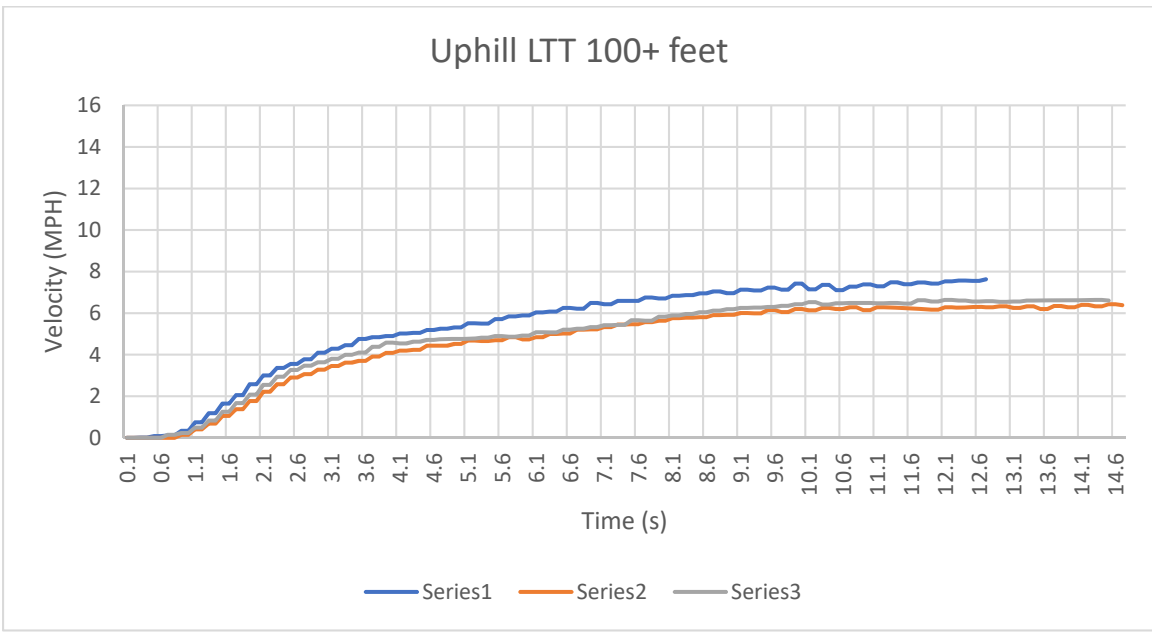


Figure 66: Uphill LTT: Cold Start

Likewise, that caused a higher variation of the uphill LTT, again reaching 19%, ignoring the outliers in Figure 67. The outliers are due to the first test series reaching the 100 ft marker prior to the second and third tests.

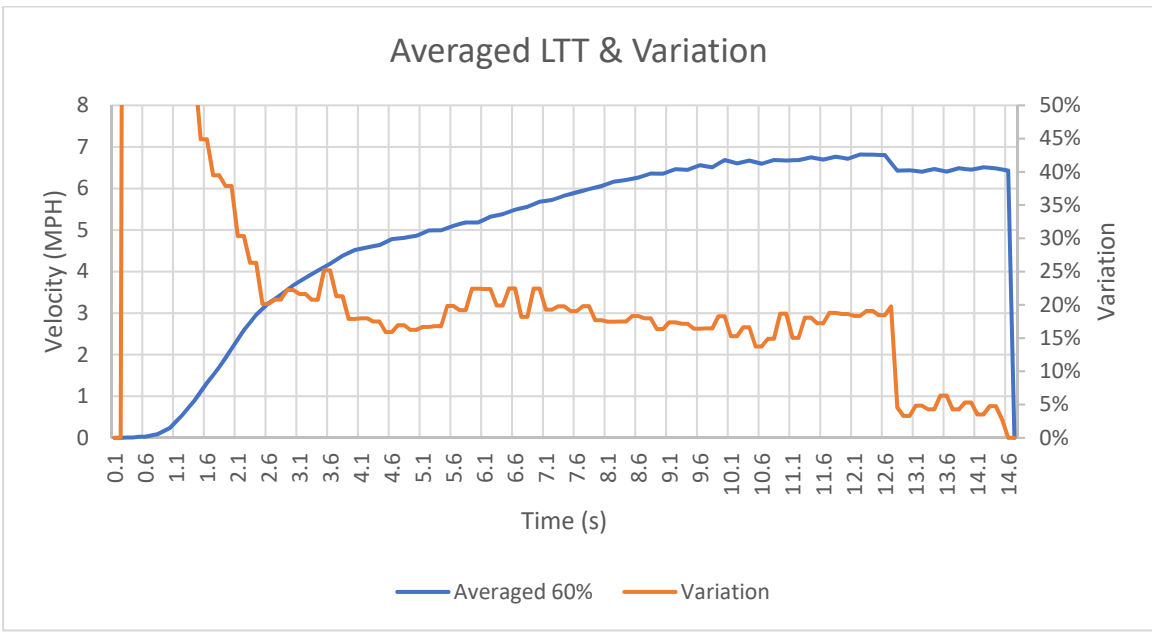


Figure 67: Averaged Uphill LTT & Variation

### 5.1.3 Electrified

Following the EV conversion, the previous testing scenarios were repeated with the newly upgraded eATV. Figure 68 displays the consistent acceleration curves of the three series in the HTT. Without the worry of the eATV becoming heat soaked, the final electric portions of the tests were run back-to-back, further demonstrating the repeatability of EV versus ICE.

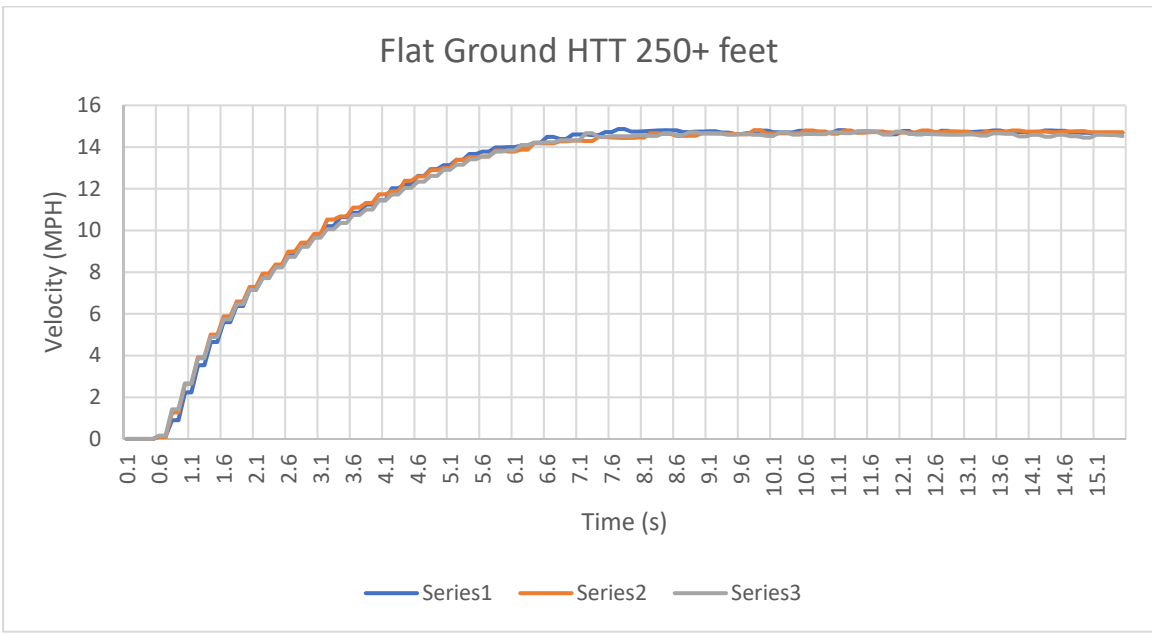


Figure 68: Flat Ground HTT: EV

Figure 69 displays the minimal variation between the 3 test runs with a 2% margin. This minimal variation begins at the 1.5 second mark, reducing the variation experienced at the beginning of the test session found in the ICE-powered vehicle testing. The test also displays the eATV reaching a steady state two times faster.

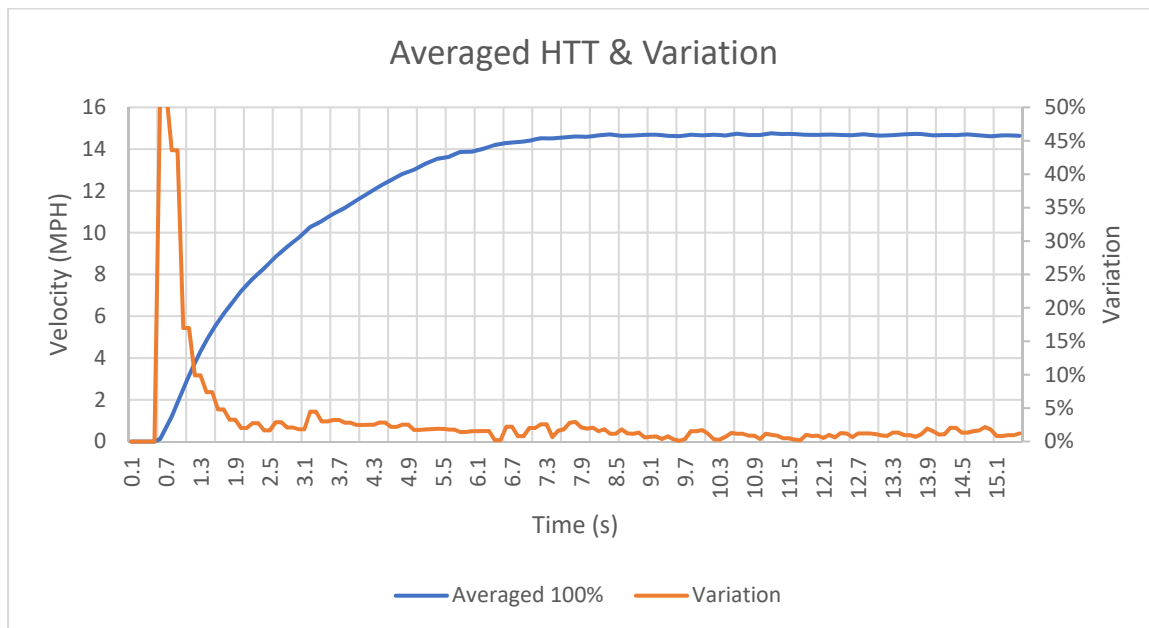


Figure 69: Averaged HTT & Variation: EV

Similarly, for the MTT session, the eATV glided through the flat ground terrain with minimal fluctuations in speed. Figure 70 illustrates a couple of minor peaks in the acceleration curve, likely caused by a bump or two in the UNC Charlotte Recreational Field 12 environment.

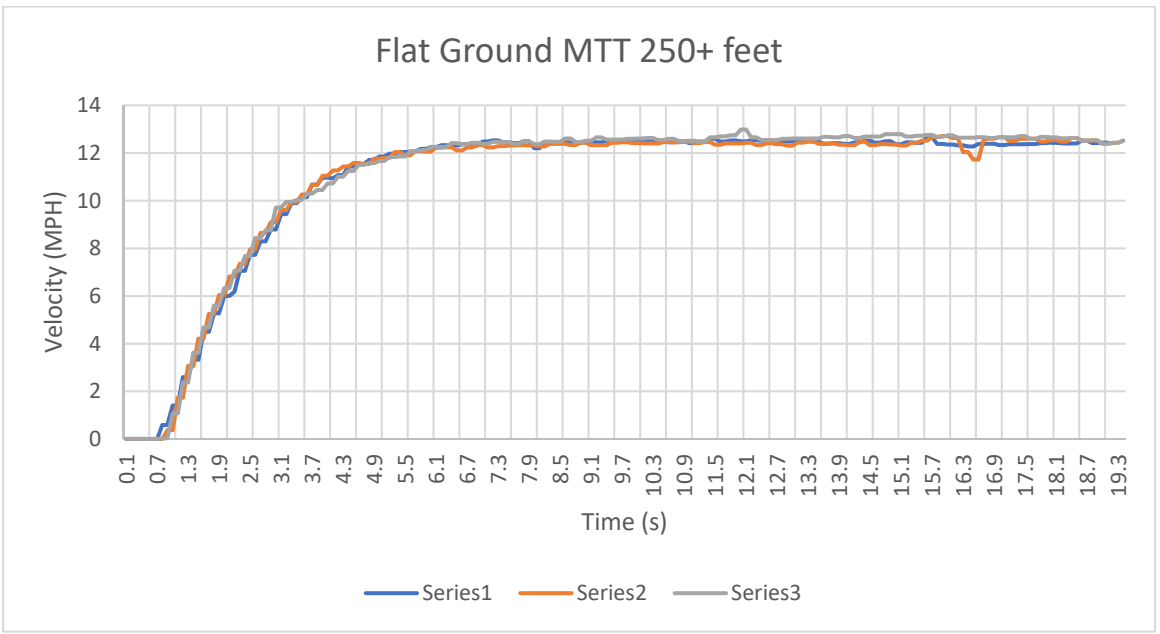


Figure 70: Flat Ground MTT: EV

Figure 71 demonstrates the variation in the flat ground MTT, which displays the peak nearing the end of the 250 ft stretch. It was decided this anomaly was negligible in the scope of the testing scenario as the bump was not likely to affect the vehicle if tested again.

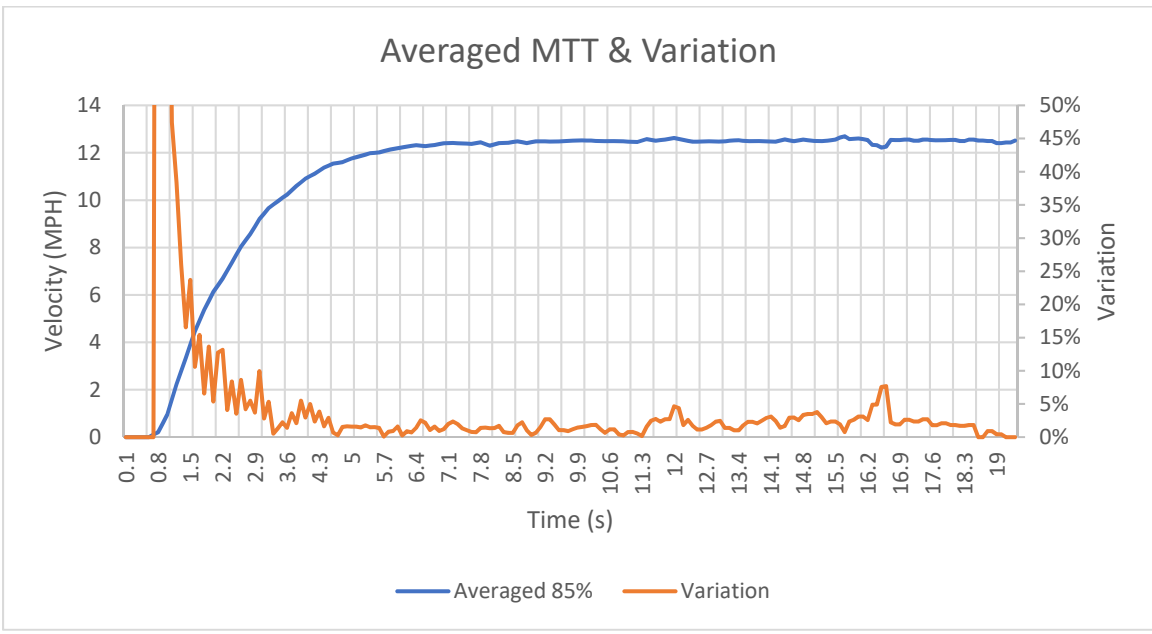


Figure 71: Averaged MTT & Variation: EV

The LTT displays the smoothest repeatable data of the three tests. As shown in Figure 72, the eATV accelerates linearly until reaching the throttle duty cycle threshold and remains at that commanded speed throughout the 250 ft. Additionally, this was the final test session of the flat ground EV testing and resembled no fade due to excessive battery consumption or heating.

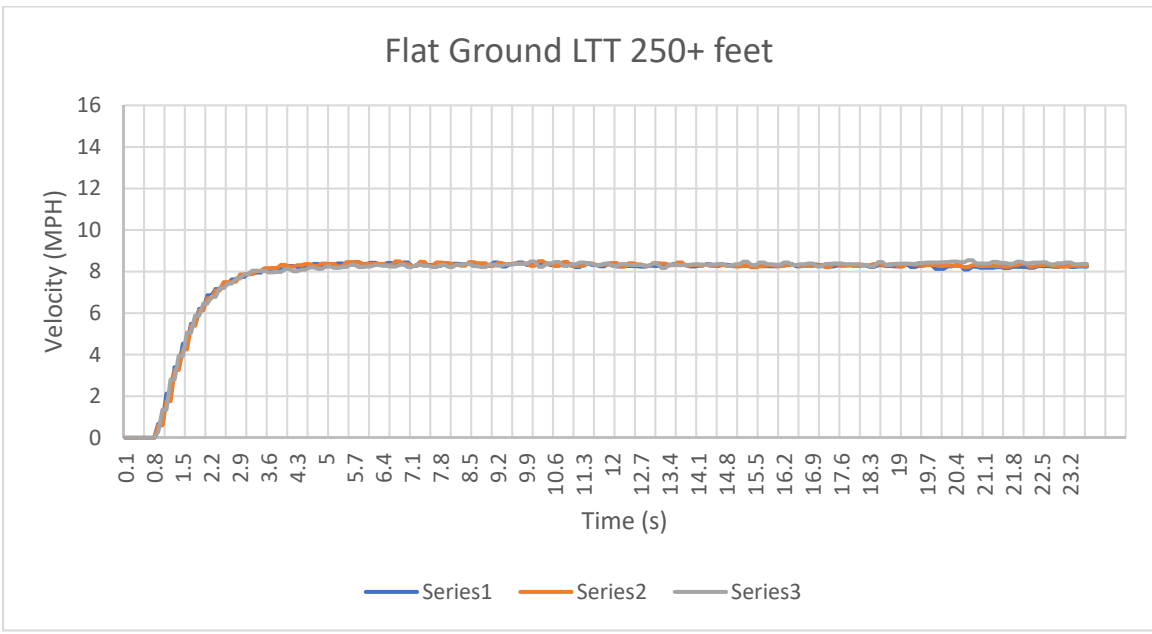


Figure 72: Flat Ground LTT: EV

The variation from the LTT is the most consistent of the tested speeds, featuring a sub-5% variation for the entire steady-state portion of the run. Figure 73 displays that the average variation for this test series was 2%. A 2% variation along a 200 ft span after conducting six test prior is a prime example of the eATV capabilities.

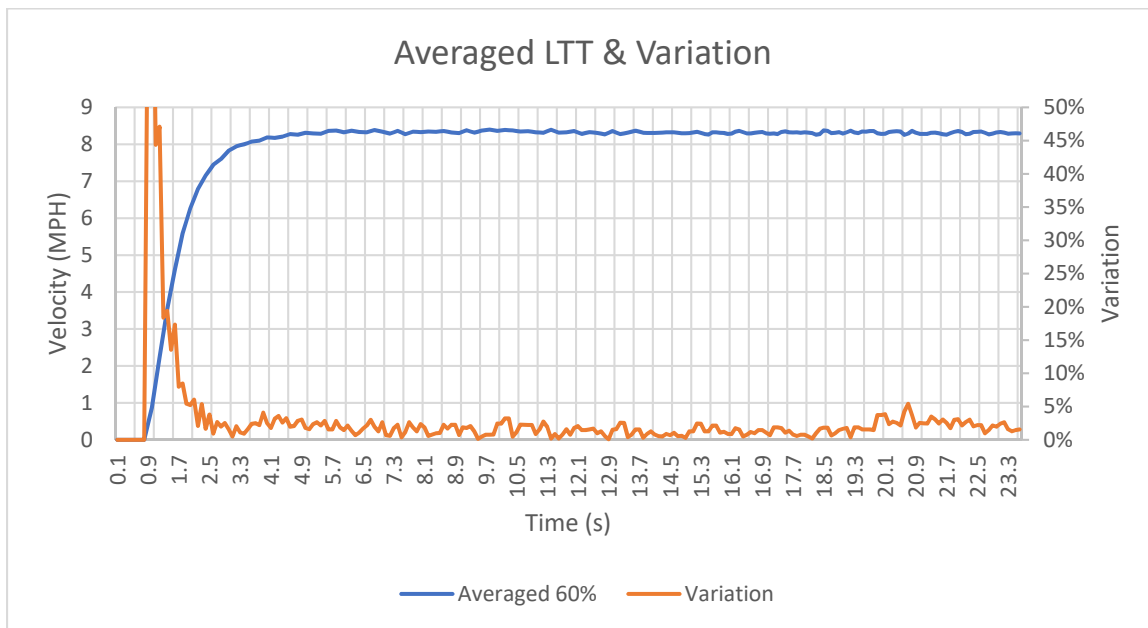


Figure 73: Averaged LTT & Variation: EV

To summarize the flat ground EV testing, the three average plots were overlaid, illustrating the linear control offered by the EV conversion versus the ICE configuration in Figure 74. The initial acceleration for each of the throttle tests followed the same slope. The eATV control scheme was able to provide a steady-state velocity at each of the throttle tests. Here, it was decided the eATV would allow greater consistency in speed control versus the ICE-powered vehicle on flat-ground terrains.

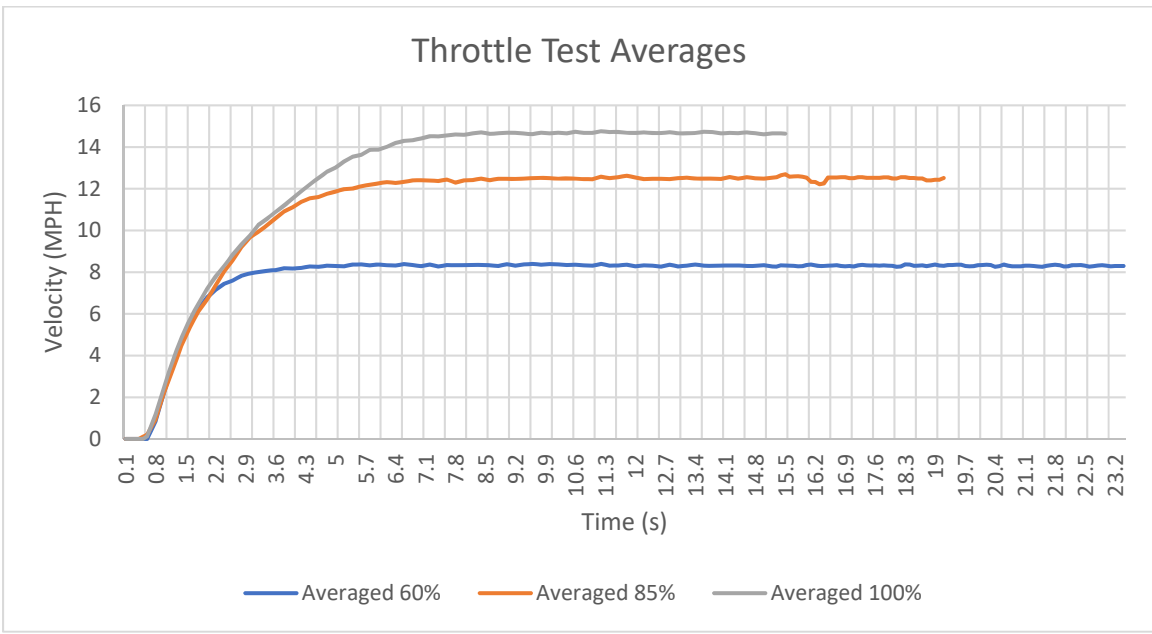


Figure 74: Summarized Throttle Response: EV

The uphill HTT was again performed for the eATV. The test data depicted a repeatable acceleration curve, according to Figure 75. The HTT recorded three alike acceleration curves from the three test series.

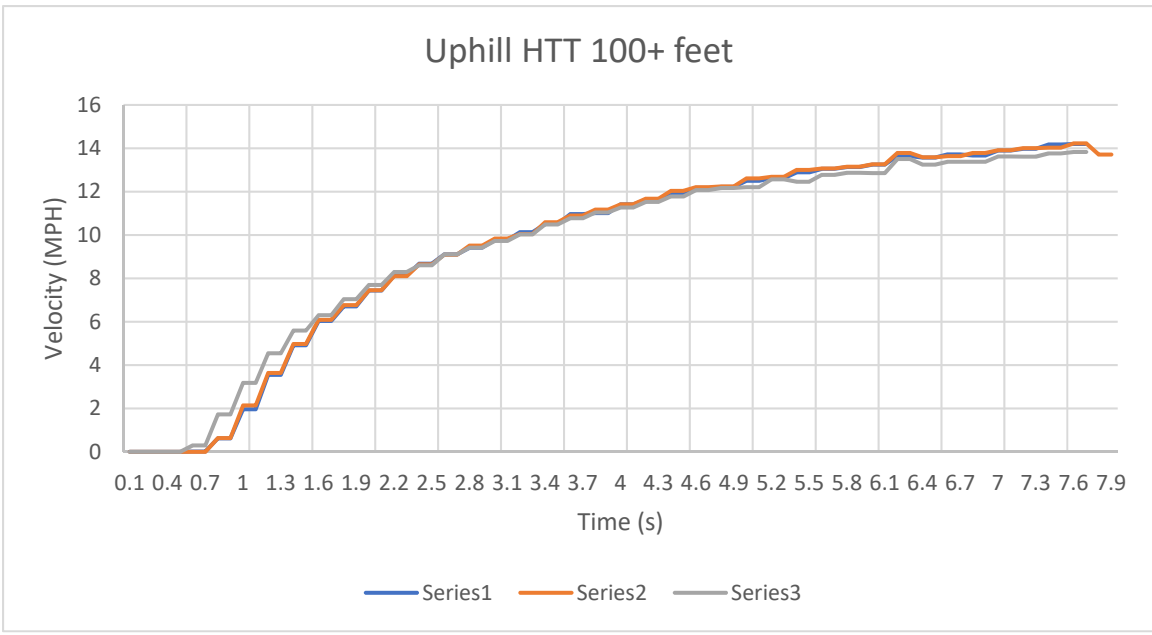


Figure 75: Uphill HTT: EV

Figure 76 displays the variation throughout the test run. The 100% testing was capable of a 2% variation through the midrange of the test. The variation increased slightly towards the end of the test session as a bump was introduced in the environment.

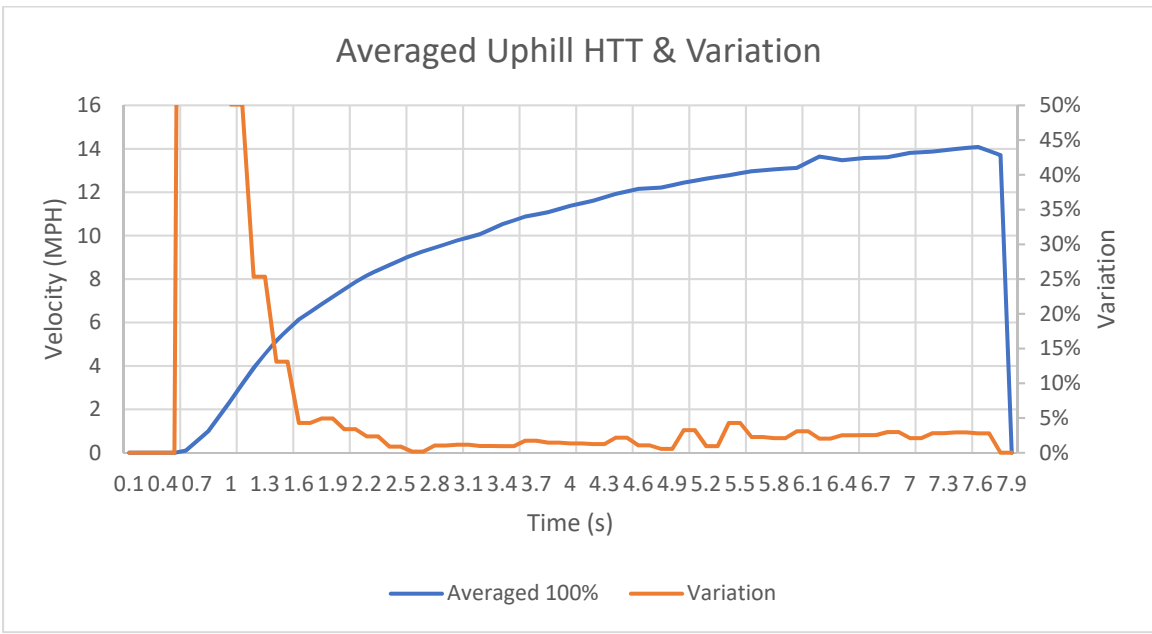


Figure 76: Averaged Uphill HTT & Variation: EV

Figure 77 details the uphill MTT, capturing three near-identical test runs. The acceleration curves express that the eATV responded to the terrain grade consistently and even reached a steady state at the 5-second marker. The ICE-powered vehicle was not capable of reaching a steady state at any of the uphill speeds tested.

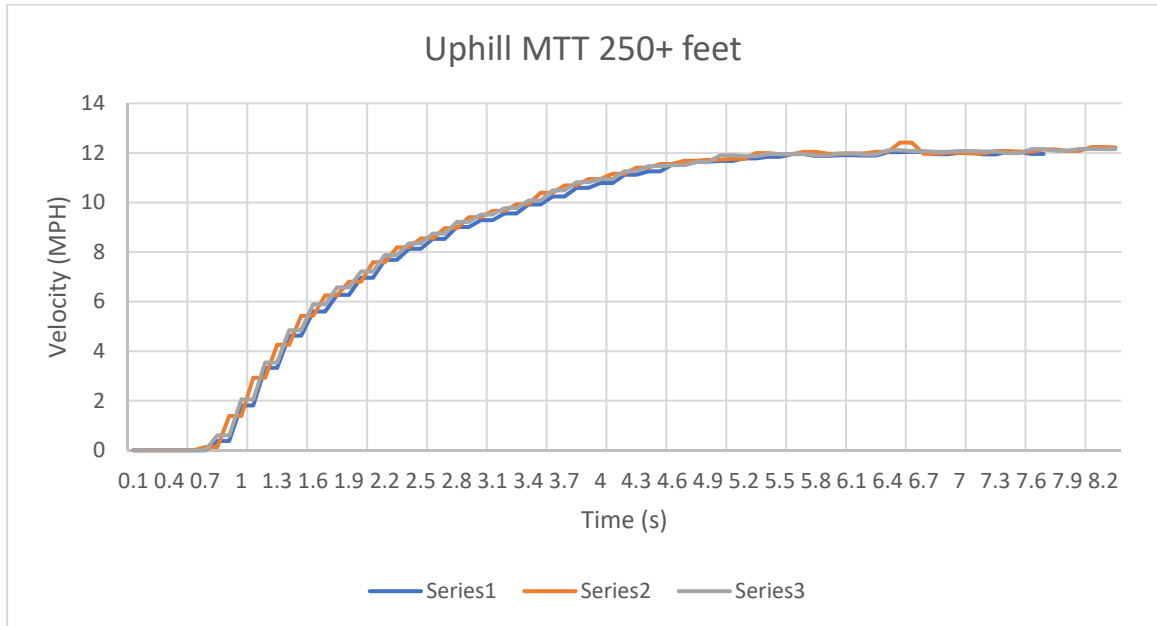


Figure 77: Uphill MTT: EV

The variation of the run initially tapers down to a consistent 3% in Figure 78. The end of the collected data also shows that the uphill MTT neared 0% variation. The eATV was capable of sub-5% variation throughout the test session after the 2 second marker. This is significant in considering the autonomous control aspect of the eATV, now capable of repeating commanded throttle duty cycles within a minimum of 2% margin of variation. The bump depicted in the prior two throttle test sessions was also captured in the variation calculation as shown in Figure 78.

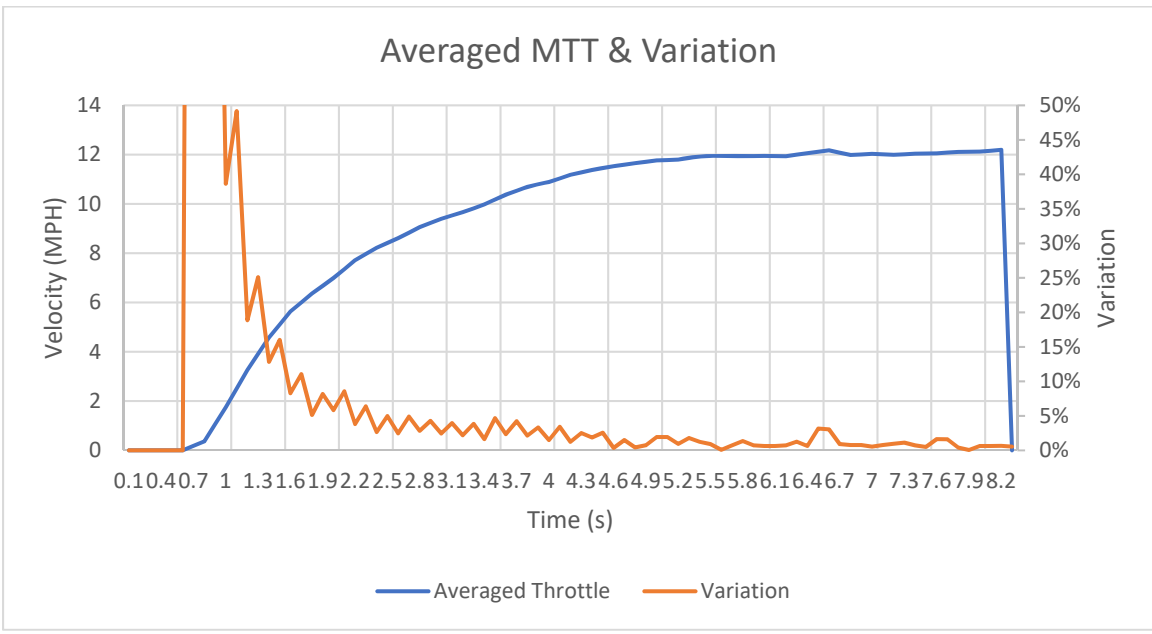


Figure 78: Averaged Uphill MTT & Variation: EV

The uphill LTT again displays a repeatable performance. In Figure 79, the eATV achieved a steady state 80% of the time while traversing up a 7% grade for 100+ ft. This is possible due to the low-rpm torque available from the gear-reduced electric motor as compared to the ICE.

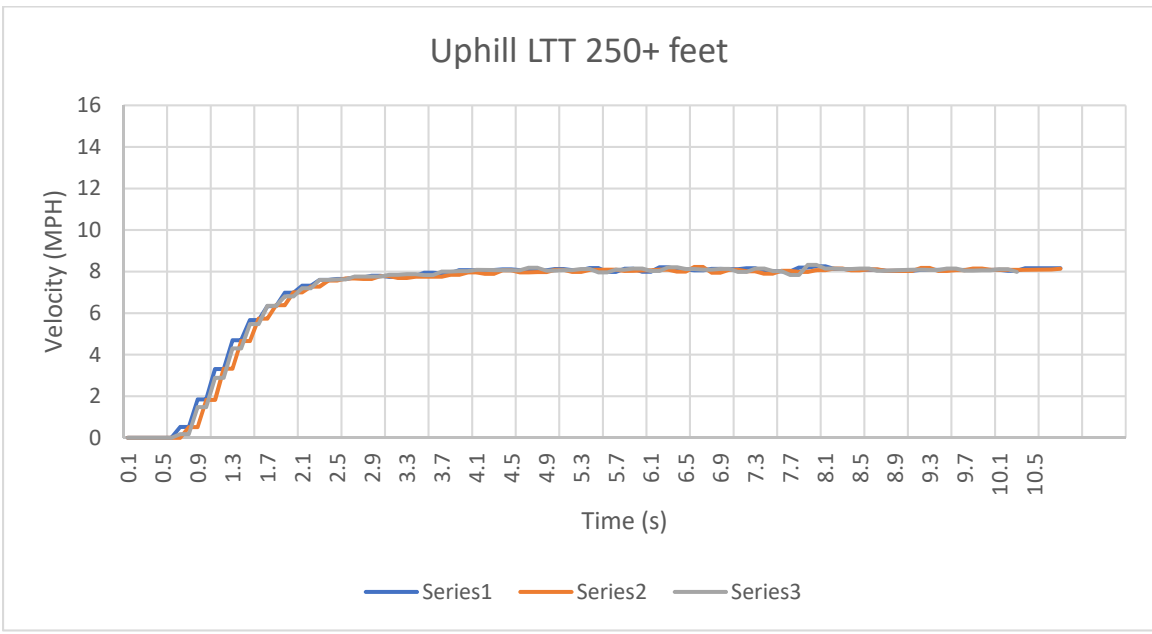


Figure 79: Uphill LTT: EV

Figure 80 provides the low variation of 3% for the uphill LTT throughout the steady portion. The eATV provided a repeatable platform for uphill travel at the LTT duty cycle percentage. The data variation drops at the 2-second mark and averages 3% for the remainder of the test session.

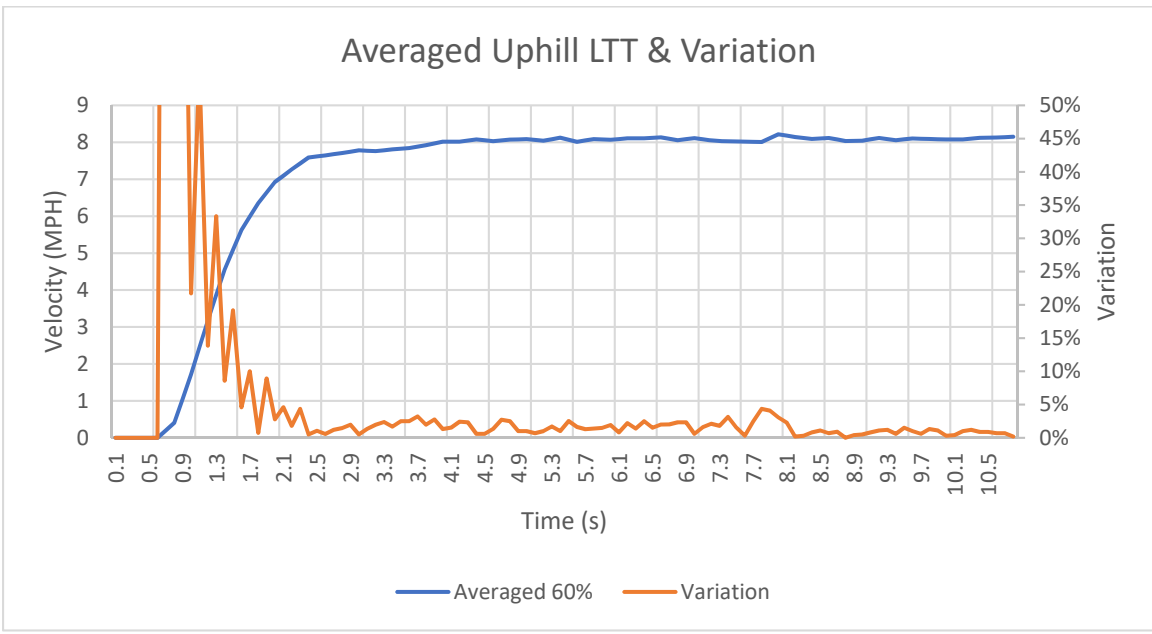


Figure 80: Averaged Uphill LTT & Variation: EV

To summarize the uphill testing of the eATV, the three average runs of each respective speed were overlaid to provide a glimpse of the linear acceleration output by the EV conversion in Figure 81. The eATV unexpectedly achieved a steady state within 3 seconds during the LTT and nearly 6 seconds during the MTT.

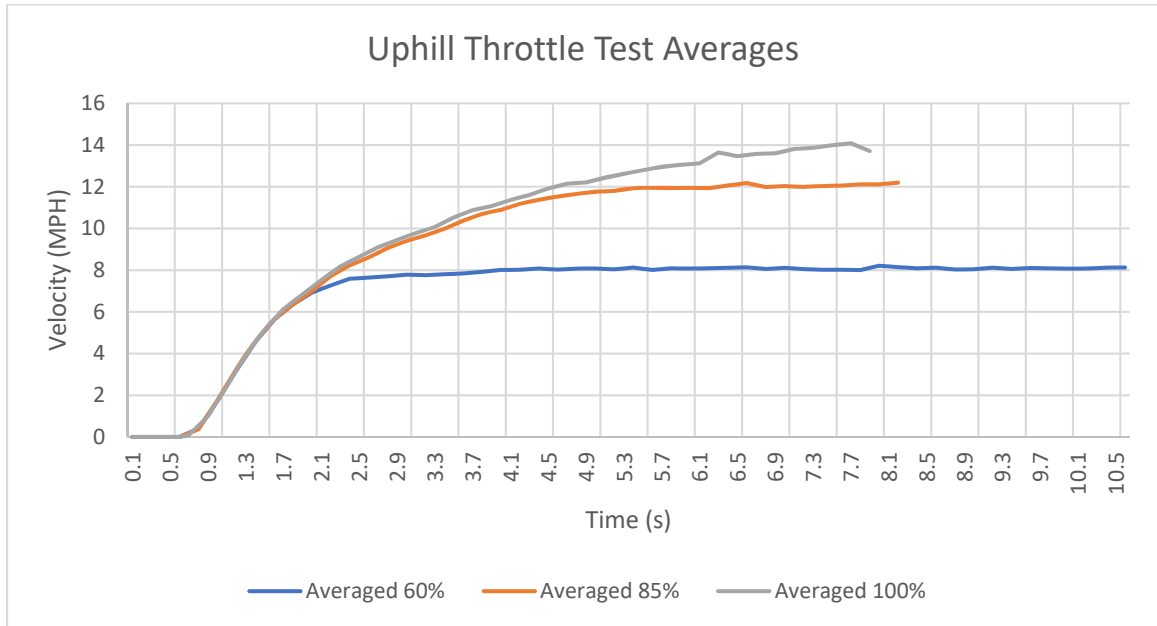


Figure 81: Summarized Uphill Throttle Response: EV

While testing the eATV, an observation was made during the downhill testing sessions. The EV conversion kit does not incorporate any regenerative or forced braking method while the eATV is in motion without throttle input. As displayed in Figure 82, the eATV accelerated linearly throughout the 100 ft downhill region of the CRI deck. Programming accommodation must be implemented to prevent the eATV from accelerating downhill unexpectedly or undesirably.

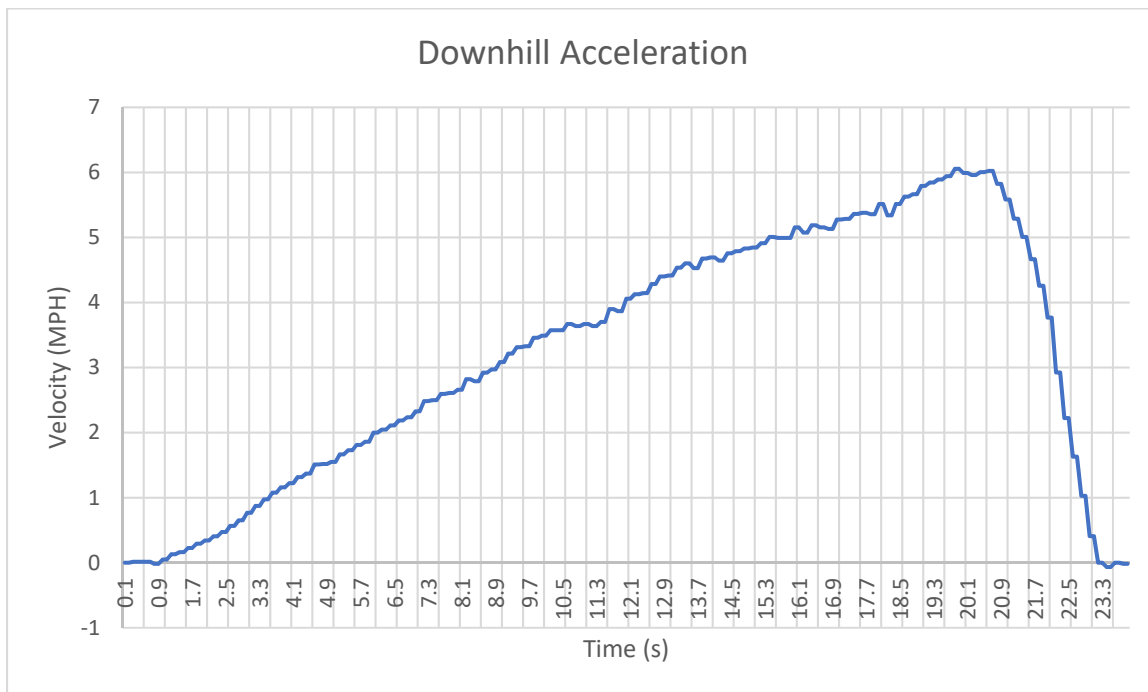


Figure 82: No Throttle Downhill Test: EV

#### 5.1.4 Overview

From the comparative testing, it was quickly noted that the ICE engine proved inconsistent as the speed varied widely throughout its operational temperature. The ICE warm start test session showed a decline in speed over time and as the temperature increased, while the ICE cold start test session showed an increase in speed as the temperature increased. This relationship is illustrated by Figure 83, detailing the change in output as the ICE vehicle approaches or exceeds the operational temperature range.

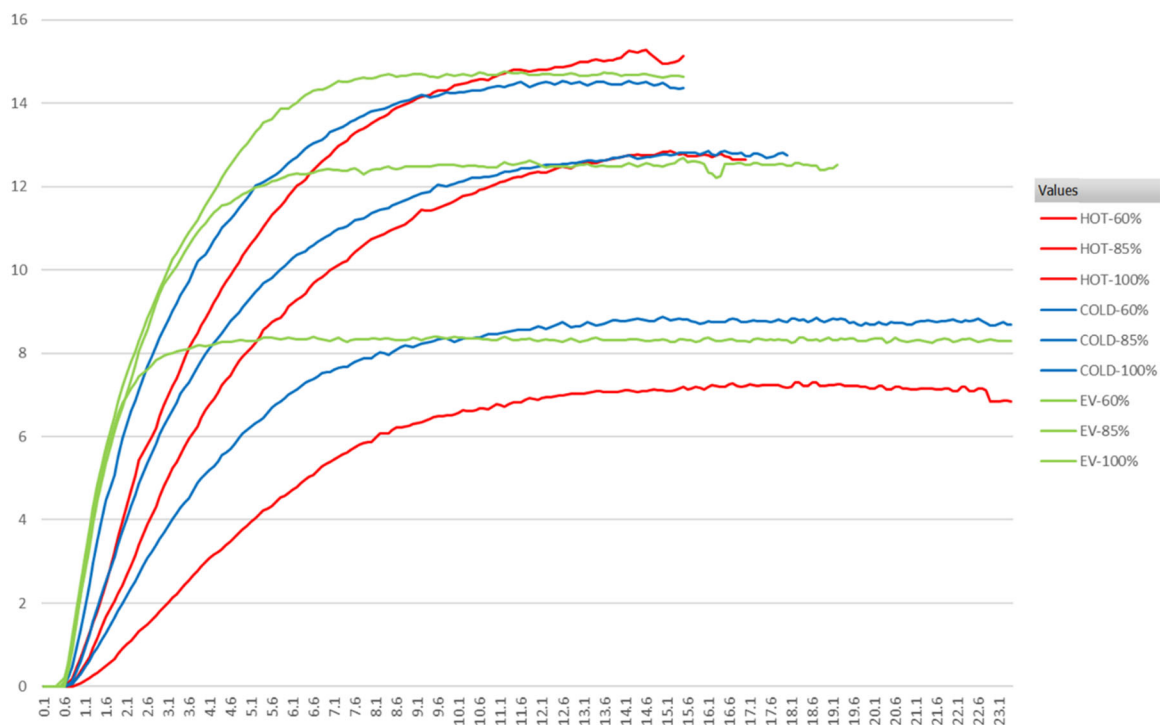


Figure 83: ICE Warm Start, ICE Cold Start, and EV Acceleration Curves

The variation in velocity was greatly reduced following the electric conversion. Most significantly, the determined operating speed range of less than 60% throttle duty cycle shows an improvement of 12 times between the warm start and electrified tests.

Table 8: Variation in Velocity

Throttle %	ICE Warm Start	ICE Cold Start	Electrified
60	23%	5%	2%
85	8%	7%	2%
100	4%	6%	2%

## 5.2 Computer Vision Testing

The vision algorithms were tested against thousands of captured images from the UNC Charlotte Fitness Trail. Average success rates for each method were calculated from the vast dataset, such as depth images for path estimation, color images for path detection, and depth images for obstacle detection, including pedestrians.

### 5.2.1 Tunnel Vision

As the LabVIEW SDK for the RealSense RGB-D camera contains the functions required to appropriately assign Z values based on the X - and Y-pixel map, there is minimal user performance required to retrieve the depth image for analysis. The SDK runs a series of programs to display the depth image on the front panel of the source program and is exported to the image processing program.

Testing the depth imaging for estimating a path direction was conducted using a combination of LabVIEW and Vision Assistant. The images were run through a developed program intended to acquire stored images on the computer and record the success of each image. A confidence value was calculated based on the likelihood that the vision script successfully defines the path location using the implemented weighting mask, prior circle location, and circle radius. Through the predetermined route along the trail, an average success rate of 93.0% was calculated for the test. The success rate based on location and imaging technique was recorded for the duration of the loop, indicating areas that were successful and other areas that required further improvement.

Occasional complications were introduced in the scenario where low-hanging branches, the horizon or sky, gaps in the tree line, or leaves would interfere with the

vision scripts. Low-hanging branches were problematic during the warmer weather, where natural foliage was dense and weighed down tree limbs. In contrast, the UNC Charlotte Fitness Trail is primarily surrounded by deciduous trees, so as the foliage began to drop, the requirements for successful vision processing changed. Figure 84 displays the well-represented seasonal changes of the UNC Charlotte Fitness Trail environment.



Figure 84: UNC Charlotte Fitness Trail: Summer (left) and Autumn (right)

To accommodate this change in scenery, the tunnel-detecting vision script was revised to target a specific red color threshold, simulating the most distance detection from the depth imager. Using the same example as in the 4.1.2 Depth Vision section, Figure 85 displays the updated processing method for the tunnel vision approach. It was determined that, given the updated environment, this method would perform with a success rate of 93.0%.

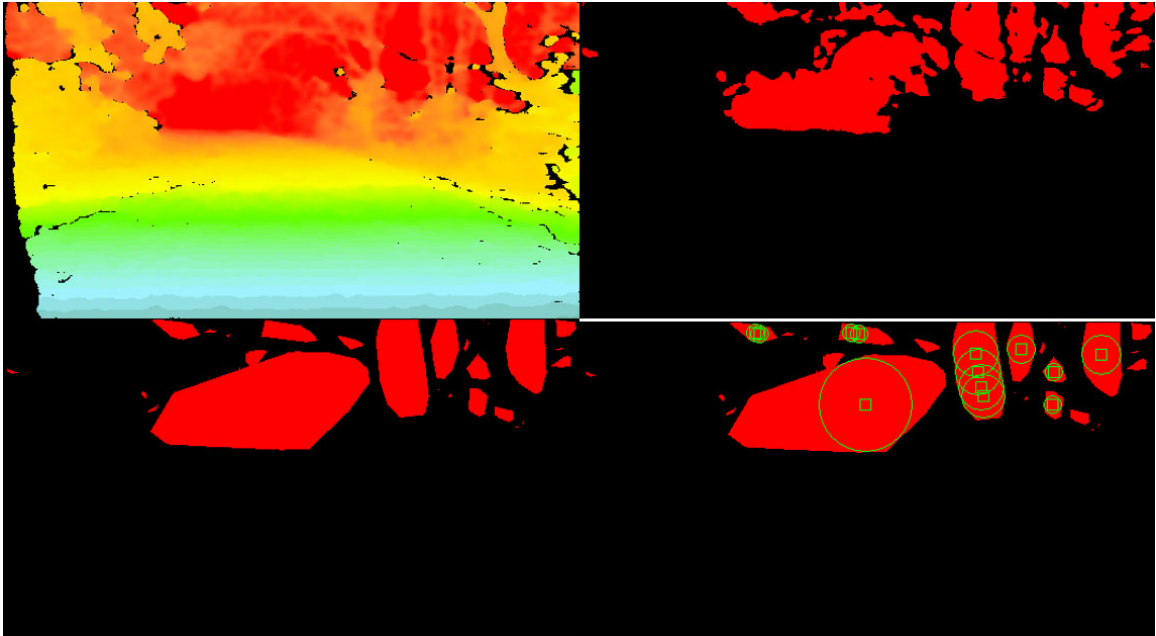


Figure 85: UL: Depth Image, UR: Binary Extraction, LL: Advanced Morphology, LR: Circle Detection

This implementation significantly reduced the noise when nearing a wiry bush. Figure 86 displays the binary analysis of an example image before and after the targeted color was revised to indicate a range of red colors instead of the dark portions of an image following the red color plane extraction.

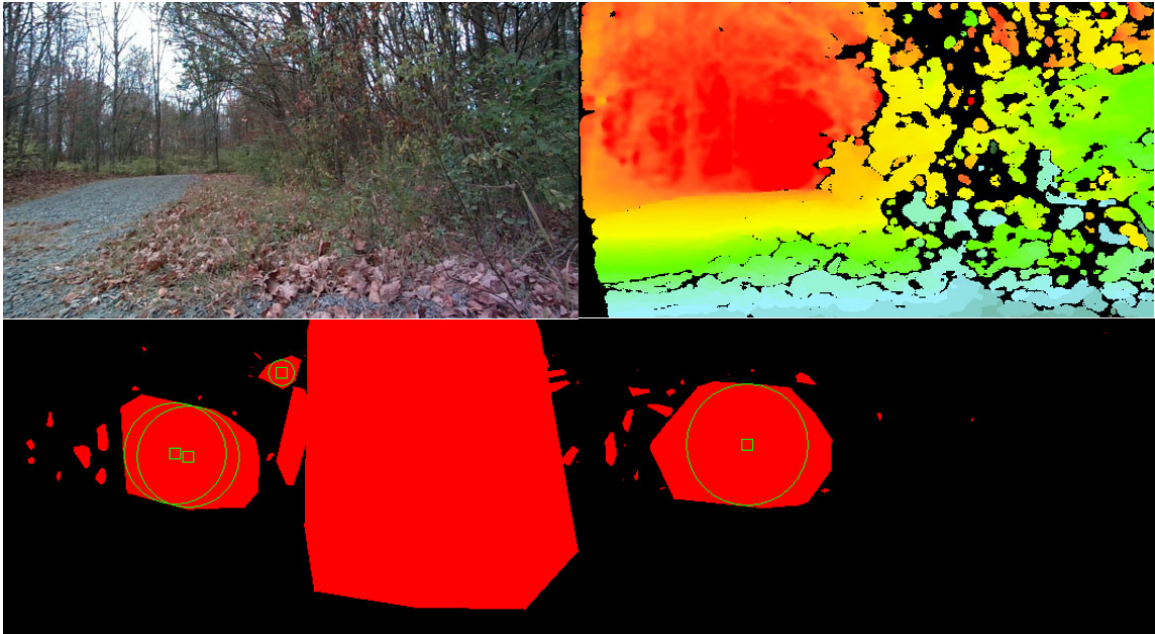


Figure 86: UL: Base Image, UR: Depth, LL: Orig. Method, LR: Rev. Method

### 5.2.2 Intersections

When the processed RGB-D vision could not detect or estimate a path direction, the eATV was programmed to halt and scan for the following GPS waypoint location. After receiving the GPS waypoint coordinates and transforming from the global to the local coordinate system determined by the GPS heading, a specific left or right direction was supplied to the main autonomy program. The autonomy program would take the input direction and actuate the steering in the new direction before applying the throttle. The main program would remain in the loop until a specified turning angle was reached or a targeted circle was processed, providing the eATV with an estimated path direction to continue along the route. Figure 87 details the methodology for processing intersections.



Figure 87: Intersection Detection Approach

Several tree lines were tested using this vision processing script; Figure 88 displays the T-intersection type found on the UNC Charlotte Fitness Trail and illustrates an intersection example where no direct path or targeted circles are recognized. It was determined that the intersections along the predetermined route were recognized with a confidence of 96% and a reaction distance of 12 meters.

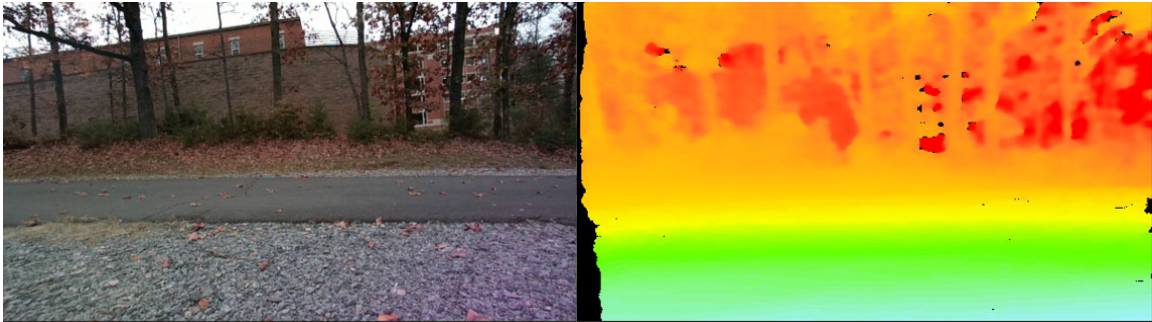


Figure 88: Intersection: Color Image (left) and Depth Image (right)

Given the user-specified route, it is noted that a wider variety of intersection scenarios may be present in other environments; however, this model provides similar results in other scenarios that may include a range-limiting drop-back, as shown in Figure 88. The reaction time could be decreased by increasing the number of sample iterations per second as the number of targeted circles drops.

### 5.2.3 Path Detection

For path detection of the gravel and asphalt portions of the trail environment, the vision scripts were revised slightly to produce a simplified shape for calculating a trajectory. Figure 89 displays the gravel path detection using a script with color plane extraction, binary conversion, particle erosion, and advanced morphology to achieve the simplified shape. It was confirmed that the confidence value for path detection of gravel and asphalt was 89.9%. Depending on the environmental factors, a third developed vision script may be selected for gravel sections with extensive leaf coverage. This was also incorporated into the processing model and the success rate for all path-detection-specific

scripts. Generally, the autonomy program can retrieve the final prioritized path image and import the shape centroid to determine the required steering angle to follow the path.

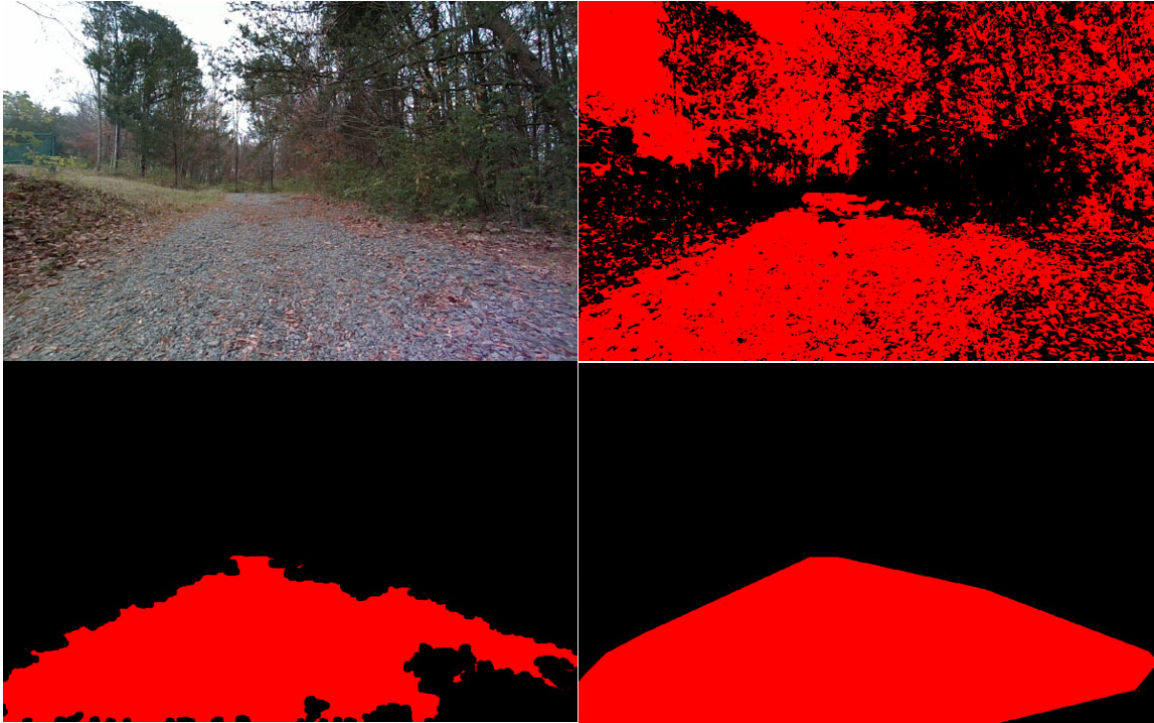


Figure 89: UL: Color Image, UR: Binary Extraction, LL: Binary Erosion, LR: Advanced Morphology

The autonomy program can alternate between the terrain-specific algorithms by comparing the confidence of both detected paths if one or more is detected simultaneously. Another approach tested required a pattern-matching scheme to detect whether the trail topography was gravel or asphalt. This was completed with minimal confidence during testing.

#### 5.2.4 Obstacle Detection

Obstacle detection was initially planned to implement a plug-and-play approach for pedestrian detection using the Intel RealSense library. It was later learned that the

advanced recognition methods offered by RealSense were not implemented into the SDK for LabVIEW and, therefore, could not simply interface with LabVIEW. An alternative methodology was developed to use the depth feature to recognize elevated surfaces within a specified range from the eATV. As the vehicle nears an obstacle, the displayed color from the depth image changes from red to green, following the natural visible spectrum. This feature was implemented to detect objects within an 8 m range, providing time for the eATV to maneuver around the obstacle or stop as necessary. The vision script for pedestrian detection was also developed simultaneously with additional shape-matching functionality. The vision script was tested with dozens of templates of pedestrians captured by the depth camera until a select few templates were deemed appropriate for the majority of pedestrian detection scenarios. A specific pedestrian detection confidence score of 77.6% was obtained from several hundred pedestrian observation events between 2.5 and 7 meters. This value is the multiple of the recorded success rate and the confidence of each pedestrian detection via the Vision Assistant script, thus providing a lesser confidence score.

For the common obstacle detection, a traffic cone, folding sign, and tall barrel were demonstrated via the obstacle detection scheme. The obstacle detection purely searches for any pixel count of a specific size within an ROI located around the travel path of the eATV. A circle detection method was implemented on the located area of interest to indicate an X- and Y-pixel value to maneuver based upon. This value was stored and recorded in the data logs for later analysis of the steering effectiveness for obstacle avoidance. Each obstacle was successfully detected within a range of 3 to 8 meters with a success rate of 97.2%. The success rate was calculated from the ratio of

successful obstacle detection against the total number of obstacle detection tests conducted.

### 5.3 GPS Testing

The predetermined waypoint-guided route was determined based on the capabilities of the eATV. It was proposed that when a user was scouting an area and leaving a trail of breadcrumbs for the eATV to follow, the user would be aware of the vehicle characteristics and would have placed the waypoints in the appropriate setting. The vehicle was placed at an intersection with two opposing directions to test the GPS waypoint susceptibility to eATV success rate. The GPS next waypoint was acquired and located with respect to the eATV orientation. If the vehicle autonomously maneuvered to orient itself toward the waypoint in question, the test was considered a success. This test series was conducted several dozen times to achieve an intersection waypoint retrieval success rate of 95.9%. The waypoint navigation runs to record the location and trajectory of the eATV throughout the test runs. Successfully arriving at a waypoint was determined by the autonomous program based on the minimum interval between the current location and the waypoint location. The waypoints were additionally confirmed via user supervision alongside the eATV test. In the scenario where a GPS waypoint is denied, the eATV would continue traversing the terrain despite the lost connectivity toward the next available GPS waypoint.

Overall validation of the onboard GPS module was conducted using a cellular device with GPS capability. The device was capable of precise measurements on the same order of magnitude as the GPS module. In practice, it is often necessary to validate

a device with an accuracy 10x that of the device being used. In this case, the eATV is guided through the walking trail with waypoints determined to have a bounding perimeter of a 2.5 m radius for each. There are no circumstances where the accuracy of the measuring device would cause the eATV to veer from the trail due to the physical limitations of the trail type (i.e., the tree line on either side). This is due to the peripheral surroundings acting as a boundary outside the detected path. Thus, after confirming that the GPS coordinates were precise with the second measuring device, a comparison was conducted. As shown in Figure 90, the waypoint coordinates from the measuring device and the actual eATV-traveled route were compared.

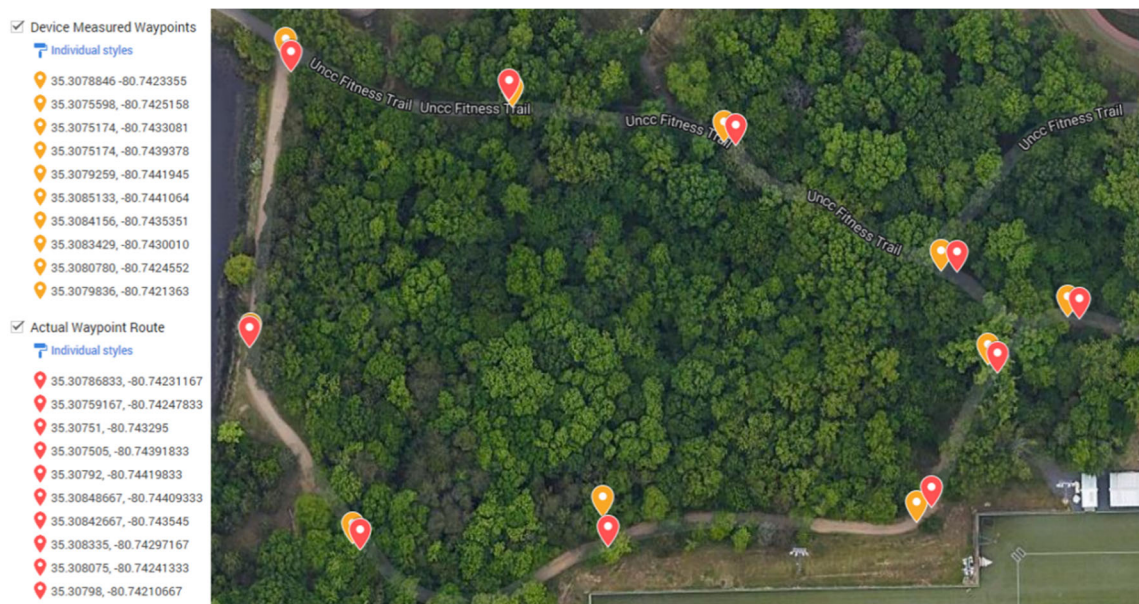


Figure 90: Onboard GPS Module Validation

Table 7 demonstrates the calculated distance between the two measured points indicating each waypoint. The compared values are the coordinates determined by both the vehicle GPS unit and a referee device. The latitude and longitude were recorded from each at the determined waypoint. The output latitude and longitude were compared, and a

delta was calculated to provide a distance between the two points. The recorded data did not exceed a delta of 5 m throughout the test.

Table 7: Onboard GPS Module Validation

Waypoint	Method	Latitude	Longitude	Delta (m)
WP 0	referee device	35.3078846	-80.7423355	<b>2.820</b>
	GPS unit	35.30786833	-80.74231167	
WP 1	referee device	35.3075598	-80.7425158	<b>4.911</b>
	GPS unit	35.30759167	-80.74247833	
WP 2	referee device	35.3075174	-80.7433081	<b>1.446</b>
	GPS unit	35.30751	-80.743295	
WP 3	referee device	35.3075175	-80.7439378	<b>2.247</b>
	GPS unit	35.307505	-80.74391833	
WP 4	referee device	35.3079259	-80.7441945	<b>0.735</b>
	GPS unit	35.30792	-80.74419833	
WP 5	referee device	35.308513	-80.7441064	<b>3.159</b>
	GPS unit	35.30848667	-80.74409333	
WP 6	referee device	35.3084156	-80.7435351	<b>1.525</b>
	GPS unit	35.30842667	-80.743545	
WP 7	referee device	35.3083429	-80.743001	<b>2.804</b>
	GPS unit	35.308335	-80.74297167	
WP 8	referee device	35.308078	-80.7424552	<b>3.814</b>
	GPS unit	35.308075	-80.74241333	
WP 9	referee device	35.3079836	-80.7421363	<b>2.715</b>
	GPS unit	35.30798	-80.74210667	

## 5.4 Autonomy Testing

Prior to integrating all autonomous features of the eATV, it was necessary to individually test and confirm the programs regarding speed control, steering, image prioritization, and obstacle avoidance.

### 5.4.1 Speed Control

The adaptive throttle and braking program was tested at a constant 45% throttle duty cycle and permitted a maximum of 6MPH. The dead band between the actual speed at 45% throttle and the speed threshold of 6 MPH was calculated to be 1.2 MPH. In testing, this value provided ample response time to maintain a constant speed downhill +/- 1 MPH responding to the trail grade.

Figure 91 illustrates the active cruise control for the eATV along the predetermined route. This test was conducted with remote control steering, allowing an independent test scenario of the throttle and braking functionality.

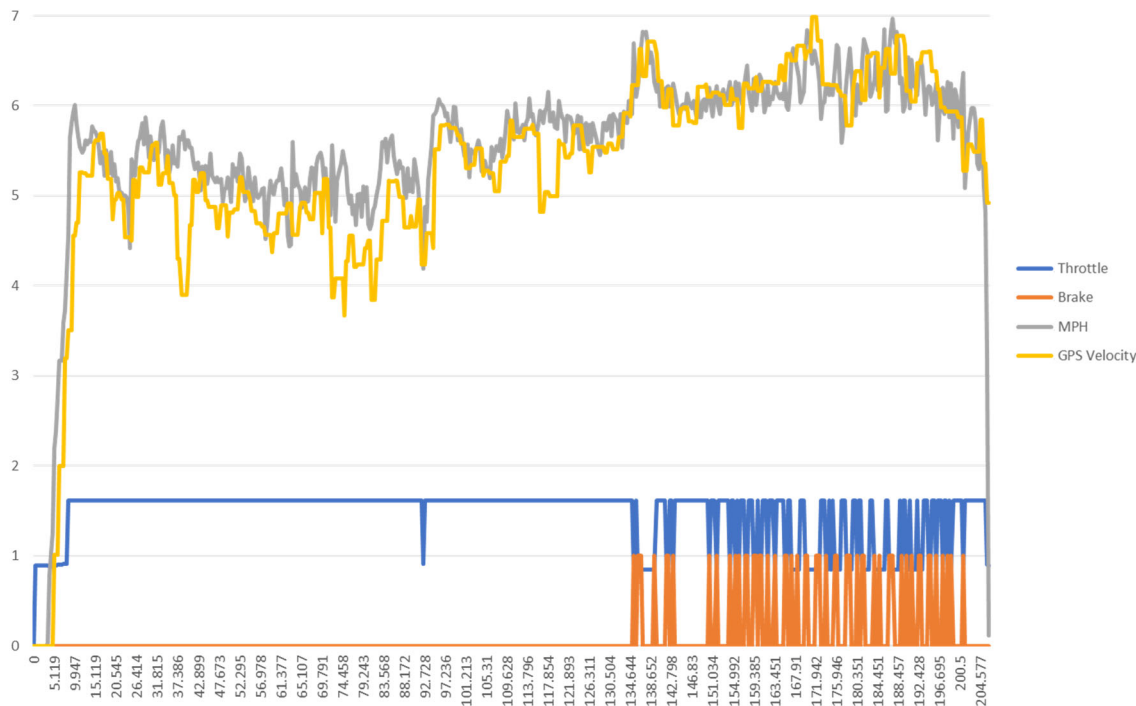


Figure 91: Adaptive Throttle and Braking Performance from 500+ meter Test

A throttle ramp and scaling were tested to accelerate from a stop and apply increased throttle uphill to retain a specified speed. The throttle ramp was able to maintain the eATV velocity within 28.9% of the specified test speed at all times.

#### 5.4.2 Vehicle Steering

The responsive steering model was tested using values directly calculated from the vision model. This test method provided the direct linkage between targeted path estimation X- and Y-pixel values with scaled values forcing the eATV to either steer left or right from the center of the image. The steering model responded accurately to the vision model 94.3% of the time. Data were collected from several test runs and analyzed, as shown in Figure 92.

It was noted that some noise interfered with the relationship between the targeted path trajectory and the vehicle steering. The output path trajectory detected the appropriate target for the vehicle, but the vehicle would occasionally respond incorrectly to the received vision data. However, this did not impact the autonomous driving performance, as the loop iterates frequently enough to provide a new value before adjusting for the erroneous calculation past a point of no recovery. This accuracy value was recorded and used in the success rate analysis for the steering sub-system.

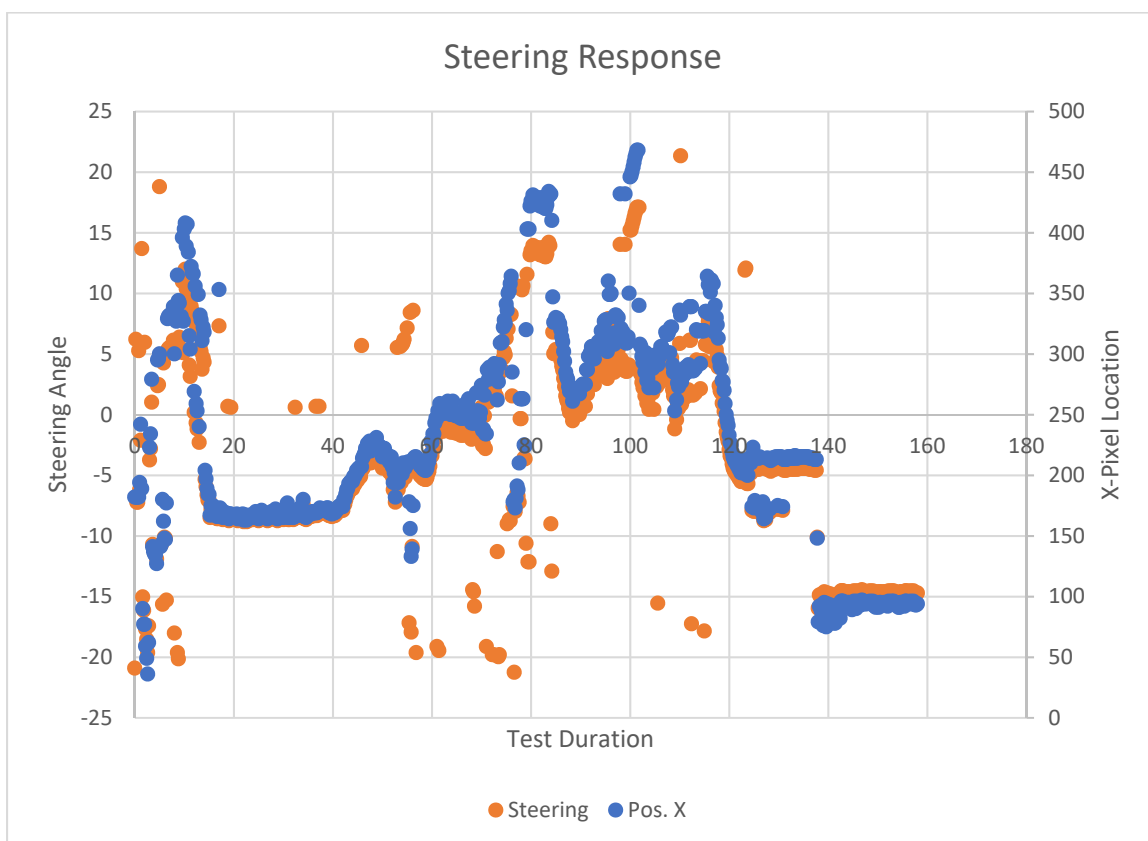


Figure 92: Steering Performance from Autonomous 50+ meter Test

### 5.4.3 Image Prioritization

To prepare the image prioritization, a series of tests were performed to analyze susceptibility to select the wrong image processing case given the variety of visible

features. Combinations of obstacles, intersections, pedestrians, allowed path detection, and targeted path estimations were provided to the vision program to determine the confidence value of the script, prioritizing the most significant case. For example, if the circle detection script has a low confidence value, but the path detection is available with a higher confidence level, the autonomy program would temporarily switch commands to receive input from the path detection vision script. A success rate was applied to the numerous cases performed and recorded.

#### 5.4.4 Obstacle Maneuvering

To verify autonomous obstacle avoidance, the first specification is that as long as a portion of the vehicle remains on the path at all times, the maneuver is considered successful. The second specification is that the eATV may not hit the obstacle. Testing provided a success rate of 91.6%, determined as the number of successful obstacle maneuvers compared to the number of obstacle maneuvers completed. The maneuvering success rate was lower than the obstacle detection confidence due to the more considerable reaction time required to navigate around the obstacle.

#### 5.5 Integration Testing

A remote-control test was conducted to test the capability of the eATV along a route on the UNC Charlotte Fitness Trail to capture rolling distance and analyze the eATV mobility in the terrain before attempting to autonomously traverse the terrain. A 35% throttle cap was applied to the controller output to allow the user to provide complete throttle control when applicable. This test concluded that the responsive braking program was necessary to apply the brakes as the eATV began accelerating

unintentionally down hills. This was captured as the eATV velocity increased past a threshold for the applied throttle percentage. The data from this first route test is displayed in Figure 93. In this test, the onboard laptop battery failed to retain power throughout the entire run, so the logger did not capture the last 30 m of the route. The DC-AC converter was implemented to prevent data loss for future testing.

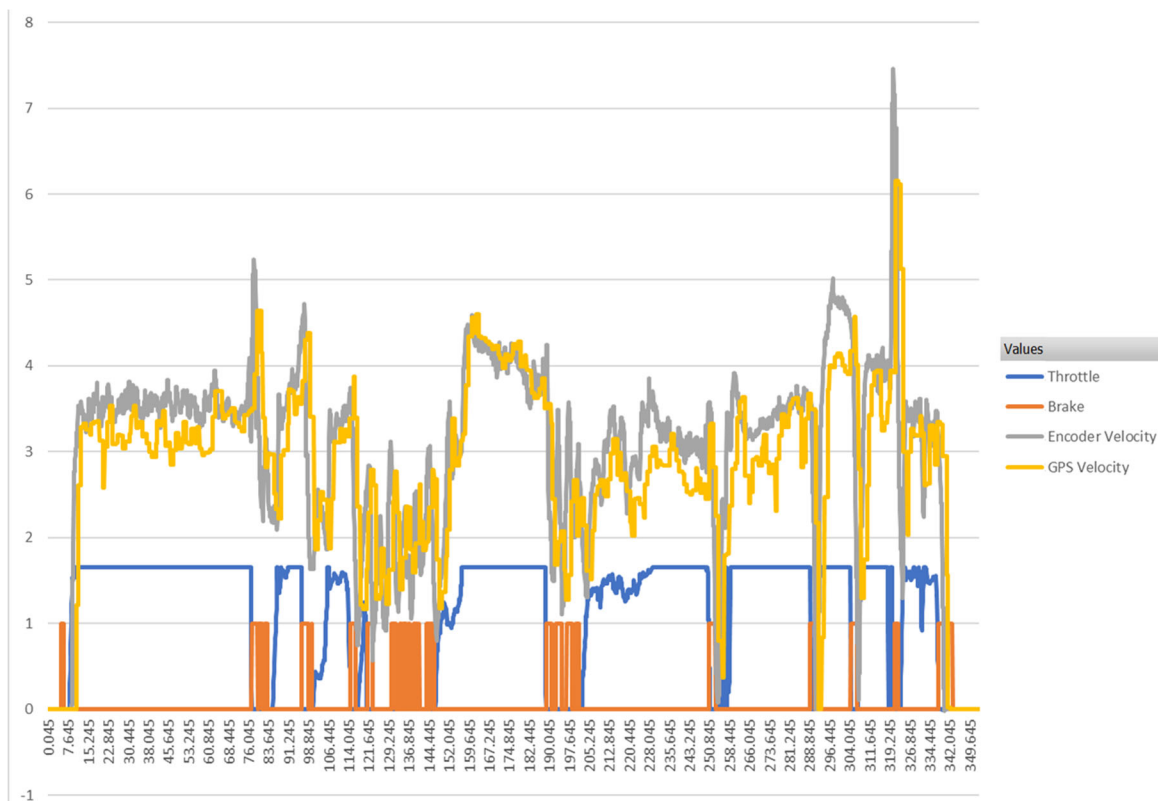


Figure 93: Initial Remote Control eATV Test on UNC Charlotte Fitness Trail

Following the initial base test run and independent autonomy testing, the integration of all vision methods, steering, and adaptive throttle and braking programs was completed allowing system testing to commence. The entire 500+ m test run required several boxes to be checked before and during the operation. Before starting the operation, all LabVIEW control programs and procedures were engaged and verified

operational. The randomly selected waypoints were disengaged from the lookup table during the test run after the first confirmed waypoint achievement. In addition to each waypoint confirmation, the total distance was confirmed at the time of the test, and the time was recorded both manually and in LabVIEW. The guidance system could be monitored in real-time by the user via LabVIEW display modules for user awareness of the operating computer vision task. An external light display on top of the eATV was also implemented to display a specific color or combination of colors during each operation.

From a programming standpoint, integrating the individual autonomous testing programs proved more difficult than anticipated. Most detection and navigation methodologies relied upon depth imaging, and the program using the RealSense SDK was further developed to include the aforementioned features. The developed system code ran remotely on the laptop to minimize computational intensity on the myRIO microcontroller. The best run of the eATV was completed with 0 missed waypoints and exceeded 500 m in a time of 3.53 minutes.

## CHAPTER 6: CONCLUSIONS

### 6.1 Overview

The EV conversion kit was integrated with the existing ATLAS hardware using appropriate wiring, relays, additional 12V batteries, and a new control scheme. From the comparative analysis, it was confirmed that the EV conversion was more suitable for autonomous applications as compared to the ICE powertrain. The improved linear acceleration, steady-state stability, and performance repeatability all contribute to the eATV successfully traversing off-road environments autonomously.

The control system architecture uses a myRIO-based processing unit supplemented with a laptop. The laptop provides a calculation-intensive platform for interpreting data from the developed vision algorithms; the myRIO is responsible for calculations involving autonomous control. The vision, navigation, and localization methodologies are adapted to the system via algorithms developed in Vision Assistant and LabVIEW. A revised autonomous steering scheme was developed, allowing for smoother mobility along the UNC Charlotte Fitness Trail in response to the commanded trajectory determined by the vision processing routines. GPS was implemented for waypoint-guided navigation through the terrain, and accommodations were programmed in the instance of GPS denial at one or more given waypoints along the predetermined route.

The tunnel vision approach for estimating path trajectory is practical for budget-conscious autonomous off-road navigation methodologies. Success rates ranging from 89.8 to 98.5% were achieved using the variable gravel and asphalt path detection and

depth imaging. The combined image processing techniques provided a 98.5% success rate. The depth imaging presented a more consistently estimated path trajectory, but the vision processing algorithms needed minor edits as environmental changes occurred through the summer and autumn seasons. Prioritization algorithms of the implemented vision processing methods were developed and allowed successful path detection to be achieved in the environment.

The obstacle detection and avoidance methodologies developed for the eATV proved successful, rating 97.2% and 91.6%, respectively. Likewise, depth imaging was an acceptably accurate means of obstacle detection within the 3- to 8-meter range. Prioritization of the imaging techniques in scenarios including obstacles and pedestrians allowed the eATV to maneuver appropriately through the trail and adjust vehicle speed as necessary. The developed intersection methodology using depth imaging provided an accurate algorithm for detecting T-intersections.

The robust waypoint-guided eATV is capable of traversing walking trail environments with asphalt and gravel terrains. The eATV prototype provides a substantial, reliable, and predictable platform while retaining a budget-conscious approach for entry-level off-road autonomy research.

## 6.2 Future Work

With additional enhancement, the eATV could perform high-fidelity operations to maneuver through a targeted trail environment. Several discoveries were made along the way and should be considered when building a budget-conscious autonomous waypoint-guided electric all-terrain vehicle for walking-trail-type environments. In retrospect,

using a state machine within LabVIEW could have drastically reduced troubleshooting efforts during final testing. Integration of the various autonomous features would ideally be programmed in fluid state transitions instead of on a case-by-case basis.

Further development could be introduced to enhance tasked-based operation for the eATV in less densely wooded walking trail environments. A streamlined comparison of disparity images for faster depth image processing would aid in the response time to path trajectory changes and obstacle maneuvering. The implementation of task-based operations could be extended into the autonomous functionality of the eATV to perform evaluations of an environment, lengthened excursions across challenging terrains, or unguided terrain scouting for reconnaissance and search-and-rescue missions.

## REFERENCES

- [1] Erian, Karim H. System Integration over a CAN Bus for a Self-Controlled, Low-Cost Autonomous All-Terrain Vehicle. ProQuest LLC, 2019.
- [2] Woodworth, Albert H. *Carburetor*. United States Patent 4,298,549, 1981.
- [3] H. Lee, N. Kim and S. W. Cha, *Model-Based Reinforcement Learning for Eco-Driving Control of Electric Vehicles*, in IEEE Access, vol. 8, pp. 202886-202896, 2020, doi: 10.1109/ACCESS.2020.3036719.
- [4] Vex Robotics. *Vex Robotics DC Motor Introduction*. Available at <https://motors.vex.com/introduction>, Last Retrieved on December 1, 2022.
- [5] Krämer, Marc & Kuhnert, Lars & Kuhnert, Klaus-Dieter. *Realtime Visual Off-Road Path Detection*. 10.24132/CSRN.2018.2801.9. 2018.
- [6] G. Csaba, L. Somlyai and Z. Vámosy, *Mobil robot navigation using 2D LIDAR*, 2018 IEEE 16th World Symposium on Applied Machine Intelligence and Informatics (SAMI), 2018, pp. 000143-000148, doi: 10.1109/SAMI.2018.8324002.
- [7] YalÇin, Özkan & Sayar, Ahmet & Arar, Omer & AKPINAR, Samet & Kosunalp, Selahattin. *Approaches of Road Boundary and Obstacle Detection Using LIDAR*. IFAC Proceedings Volumes (IFAC-PapersOnline). 1. 10.3182/20130916-2-TR-4042.00025. 2013.
- [8] J. Li, X. He and J. Li, *2D LiDAR and camera fusion in 3D modeling of indoor environment*, 2015 National Aerospace and Electronics Conference (NAECON), 2015, pp. 379-383, doi: 10.1109/NAECON.2015.7443100.
- [9] Y. Zhang, J. Wang, X. Wang and J. M. Dolan, *Road-Segmentation-Based Curb Detection Method for Self-Driving via a 3D-LiDAR Sensor*, in IEEE Transactions on Intelligent Transportation Systems, vol. 19, no. 12, pp. 3981-3991, Dec. 2018, doi: 10.1109/TITS.2018.2789462.
- [10] Vision Team. *What is a stereo vision camera?* Available at <https://www.e-consystems.com/blog/camera/technology/what-is-a-stereo-vision-camera-2/>, Last Retrieved on December 1, 2022.
- [11] Chen, David. *Depth Cameras Can Fill LiDAR's Autonomous Vehicle Blind Spots—Here's How*. Available at <https://www.vision-systems.com/astech-autonomy/article/14280541/depth-camera-can-fill-lidars-autonomous-vehicle-blind-spots-heres-how>, Last Retrieved on December 1, 2022.

- [12] Rychlicki, Mariusz, Zbigniew Kasprzyk, and Adam Rosiński. *Analysis of Accuracy and Reliability of Different Types of GPS Receivers*, Sensors 20, no. 22: 6498. <https://doi.org/10.3390/s20226498>. 2020.
- [13] Y. Morales and T. Tsubouchi, *GPS moving performance on open sky and forested paths*, 2007 IEEE/RSJ International Conference on Intelligent Robots and Systems, 2007, pp. 3180-3185, doi: 10.1109/IROS.2007.4399307.
- [14] K. Chiang, D. Le, K. Lin, & M. Tsai. Multifusion schemes of INS/GNSS/GCPs/V-SLAM applied using data from smartphone sensors for land vehicular navigation applications. <https://doi.org/10.1016/j.inffus.2022.08.012>, 2022.
- [15] Charroud, A., Moutaouakil, K.E. & Yahyaouy, A. *Fast and accurate localization and mapping method for self-driving vehicles based on a modified clustering particle filter*. Multimed Tools Appl. <https://doi.org/10.1007/s11042-022-14111-4>, 2022.
- [16] E. Ackerman & E. Guizzo. iRobot Brings Visual Mapping and Navigation to the Roomba 980. IEEE Spectrum, 2015.
- [17] Zhang, Lintong & Helmberger, Michael & Fu, Lanke & Wisth, David & Camurri, Marco & Scaramuzza, Davide & Fallon, Maurice. *Hilti-Oxford Dataset: A Millimetre-Accurate Benchmark for Simultaneous Localization and Mapping*. ResearchGate, 2022.
- [18] D. P. Grabowsky, J. M. Conrad and A. F. Browne, *A Breadcrumb System for Assisting Outdoor Autonomous Robots with Path Identification and Localization*, SoutheastCon 2021, 2021, pp. 1-6, doi: 10.1109/SoutheastCon45413.2021.9401846.
- [19] Pfeifer, Elijah Killian. *Autonomous Vehicle Navigation and Obstacle Avoidance Along a Predetermined Vector*. ProQuest Dissertations Publishing, 2021.
- [20] Boche, Simon & Zuo, Xingxing & Schaefer, Simon & Leutenegger, Stefan. *Visual-Inertial SLAM with Tightly-Coupled Dropout-Tolerant GPS Fusion*. 10.48550/arXiv.2208.00709. ResearchGate, 2022.
- [21] Brake, Jeremy Mckenzie. *Prototype System for Autonomous Detection and Extraction of Floating Pollution from Aquatic Environments*. ProQuest Dissertations Publishing, 2021.
- [22] Kelly, A. et al. *Toward Reliable Off Road Autonomous Vehicles Operating in Challenging Environments*. In: Ang, M.H., Khatib, O. (eds) *Experimental Robotics IX*. Springer Tracts in Advanced Robotics, vol 21. Springer, Berlin, Heidelberg.
- [23] K. H. Erian and J. M. Conrad, *Controlling ATV Steering Angle on a Forest Path Using Machine Learning*, SoutheastCon 2021, 2021, pp. 01-07, doi: 10.1109/SoutheastCon45413.2021.9401942.

- [24] T. Way, D. Erbach, A. Bailey, E. Burt, & C. Johnson. *Soil displacement beneath an agricultural tractor drive tire*. ScienceDirect, 2004.
- [25] K. Xia. Finite element modeling of tire/terrain interaction: Application to predicting soil compaction and tire mobility. ScienceDirect, 2010.
- [26] S. Naranjo, C. Sandu, Saied Taheri, & Shahyar Taheri. *Experimental testing of an off-road instrumented tire on soft soil*. ScienceDirect, 2014.
- [27] Petterson, T. & Gooch, S.. *ROLLING RESISTANCE OF ATV TYRES IN AGRICULTURE*. Proceedings of the Design Society: DESIGN Conference. 1. 2561-2570. 10.1017/dsd.2020.75. 2020.
- [28] K. Suman and A. T. Mathew, *Speed Control of Permanent Magnet Synchronous Motor Drive System Using PI, PID, SMC and SMC plus PID Controller*, 2018 International Conference on Advances in Computing, Communications and Informatics (ICACCI), 2018, pp. 543-549, doi: 10.1109/ICACCI.2018.8554788.
- [29] US Digital. *E6 Optical Kit Encoder*.  
<https://www.usdigital.com/media/vw2cjdjo/e6-datasheet.pdf>. Last Retrieved on December 1, 2022.
- [30] Intel RealSense. *Intel® RealSense™ Depth Camera D455*.  
<https://www.intelrealsense.com/depth-camera-d455/>. Last Retrieved on December 1, 2022.
- [31] Keisan Casio. *New coordinates by rotation of axes Calculator*.  
<https://keisan.casio.com/exec/system/1223522781>. Last Retrieved on December 1, 2022.

## APPENDIX A: LabVIEW Code

## A.1 Computer Vision

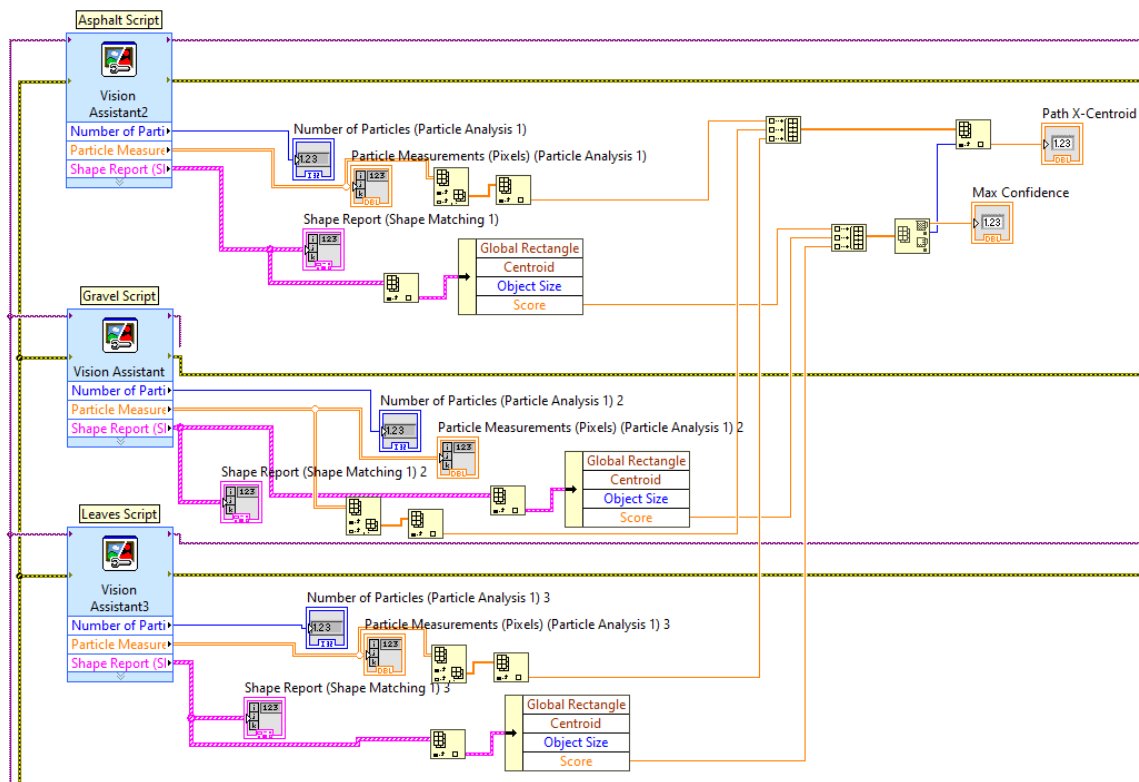


Figure 94: Vision Processing Image Script Prioritization

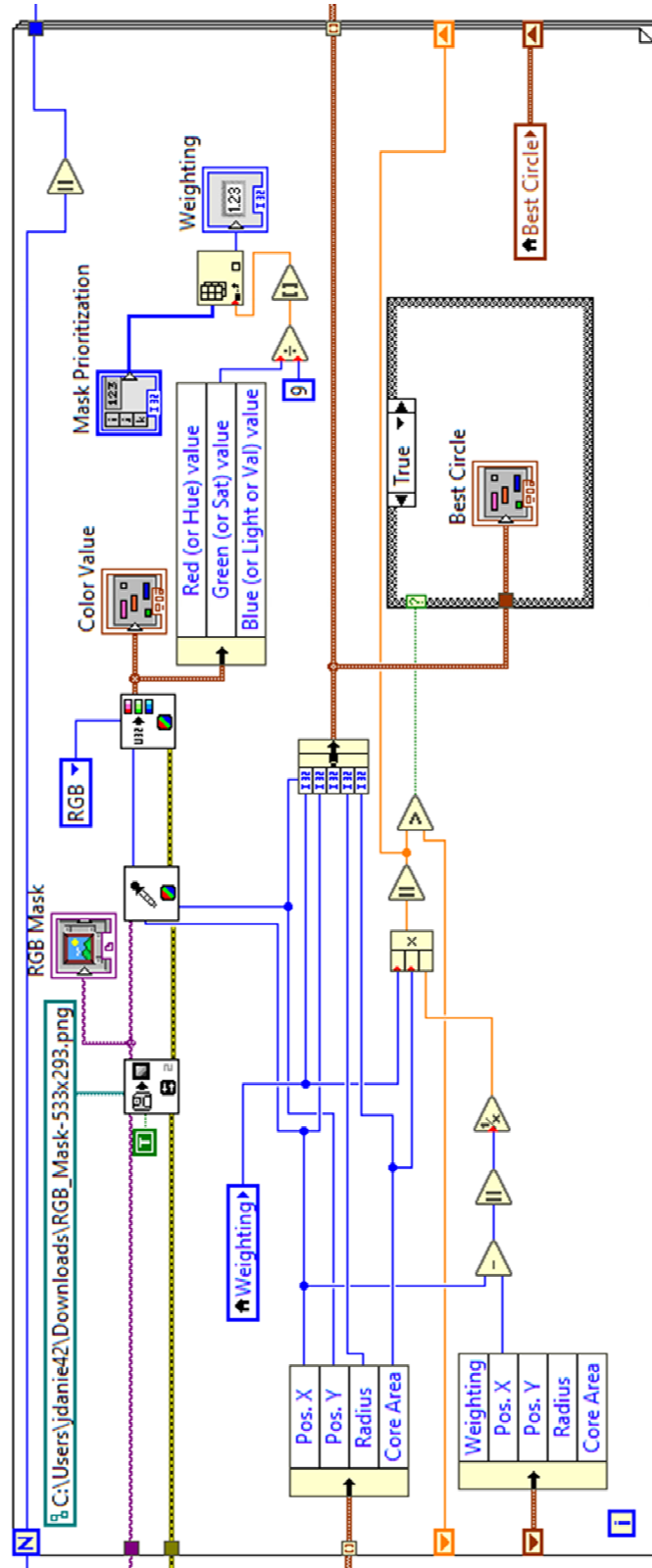


Figure 95: Applying Weighing to Geometry of Interest

## A.2 Localization

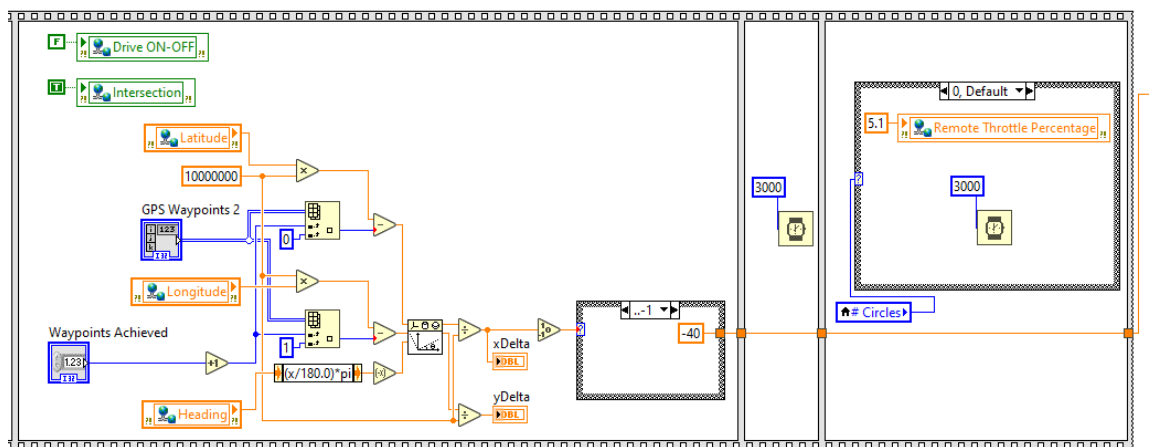


Figure 96: Waypoint Detection at Intersections

## A.3 Navigation

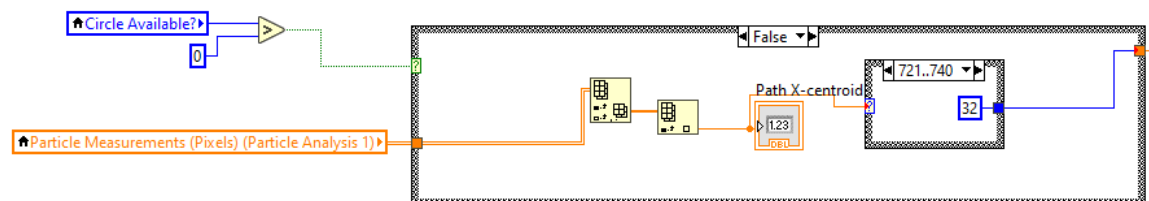


Figure 97: Steering Algorithm for Color-Vision Imaging

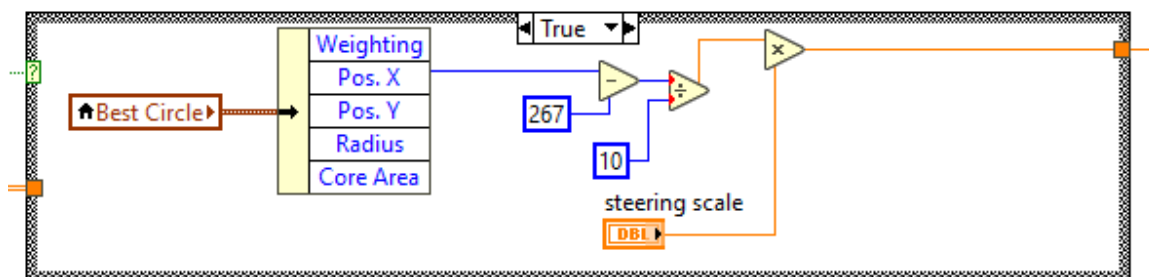


Figure 98: Steering Algorithm for Depth-Vision Imaging

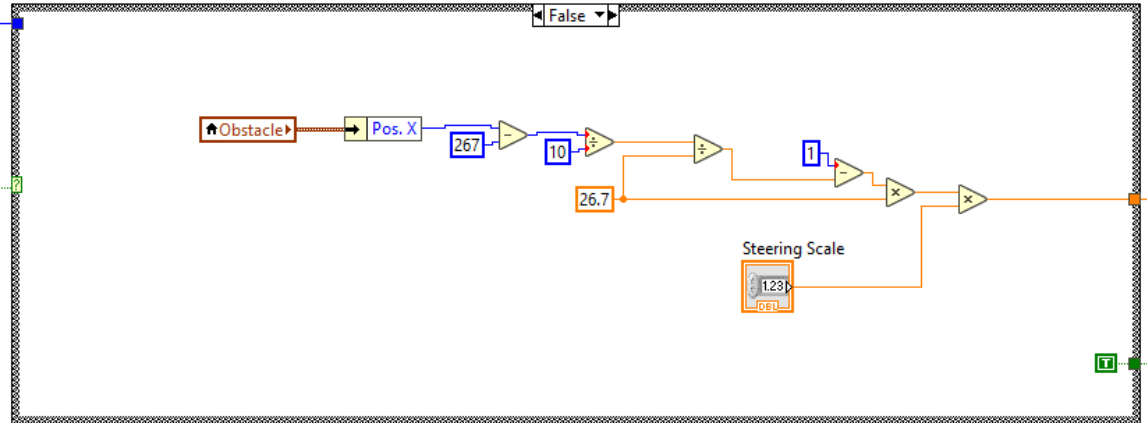


Figure 99: Steering Algorithm for Obstacle Avoidance



## APPENDIX B: Computer Vision Scripts

### B.1 Gravel Detection



Figure 101: Gravel Detection Script

### B.2 Asphalt Detection



Figure 102: Asphalt Detection Script

### B.3 Obstacle Detection



Figure 103: Obstacle Detection Script

### B.4 Depth Analysis



Figure 104: Depth Analysis Script

## B.5 Pedestrian Detection Script

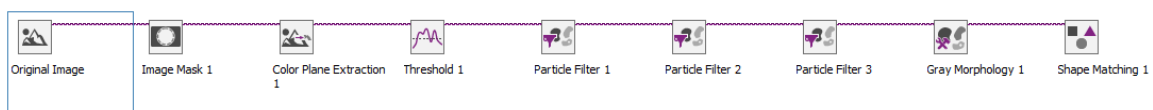


Figure 105: Pedestrian Detection Script

## APPENDIX C: Supplemental Information

## C.1 Mechanical Assemblies

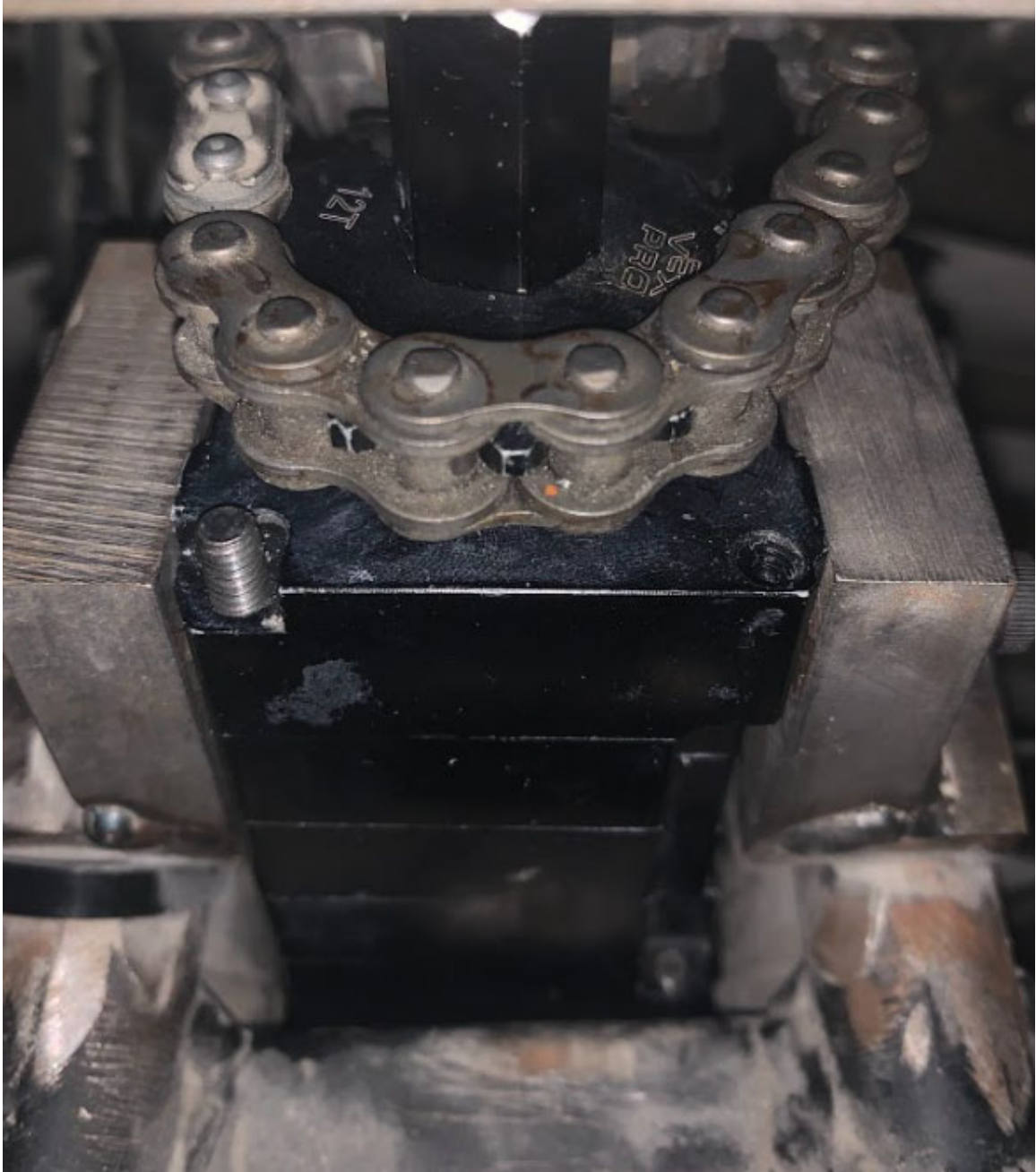


Figure 106: Offset DC Motor Steering Assembly



Figure 107: Installed EV Conversion Kit and Supporting Components

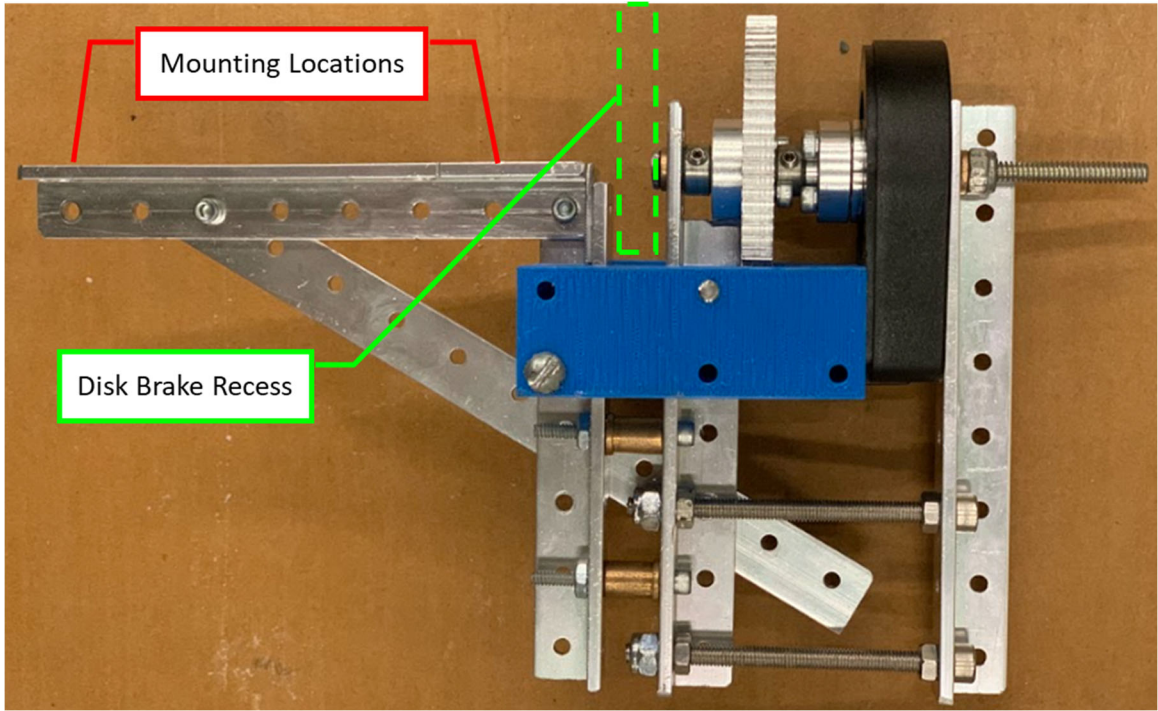


Figure 108: Encoder Structure

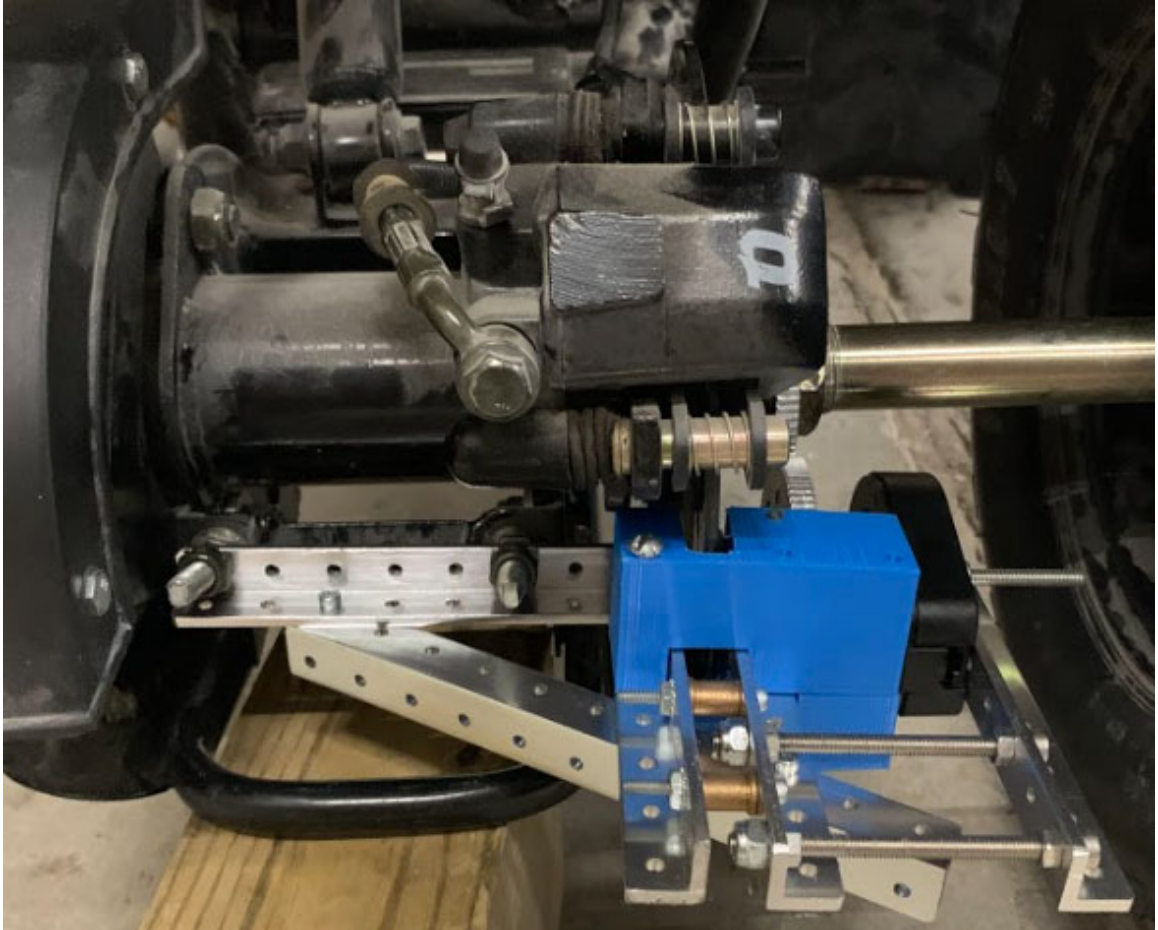


Figure 109: Installed Encoder Structure